Using local, global, and simulated earthquakes to inform earthquake resilience efforts in the Pacific Northwest

Mika Thompson

A dissertation

submitted in partial fulfillment of the

requirements for the degree of

Doctor of Philosophy

University of Washington

2022

Reading Committee:

Erin A. Wirth, Chair

J. Renate Hartog

Kenneth C. Creager

Program Authorized to Offer Degree:

Earth and Space Sciences

University of Washington

Abstract

Using local, global, and simulated earthquakes to inform earthquake resilience efforts in the Pacific Northwest

Mika Thompson

Chair of the Supervisory Committee:

Erin A. Wirth

Earth and Space Sciences

In this dissertation, we investigate how the geometry and rock composition of the Seattle and Tacoma basins influences strong ground motions during local earthquakes by surveying and interpreting strong-motion seismic records and generating 3D ground-motion simulations. We also evaluate the performance of an earthquake early warning system for the West Coast of the United States using historical records of local and global intraslab earthquakes and ground-motion simulations of hypothetical magnitude 9 megathrust earthquake scenarios on the Cascadia subduction zone (CSZ).

Chapter 2 is a characterization of sedimentary basin effects within the Seattle and Tacoma basins using Pacific Northwest Seismic Network and U.S. Geological Survey strong-motion recordings of five local earthquakes (*M* 3.9–6.8), including the 2001 Nisqually earthquake. We observe basin-edge generated surface waves at sites within the Seattle basin for

most ray paths that cross the Seattle fault zone. We also note previously undocumented basin-edge surface waves in the Tacoma basin during one of the local earthquakes. To place quantitative constraints on basin amplification, we determine amplification factors by computing the spectral ratios of inside-basin sites to outside-basin sites at 1, 2, 3, and 5 s periods. Ground shaking is amplified in the Seattle basin for all the earthquakes analyzed and for a subset of events in the Tacoma basin. We find that the largest amplification factors in the Seattle basin are produced by a shallow crustal earthquake located to the southwest of the basin. Our observation suggests that future shallow crustal and megathrust earthquakes rupturing west of the Puget Lowland will produce greater amplification within the Seattle basin than has been seen for intraslab events. We also perform ground-motion simulations using a finite-difference method to validate a 3D Cascadia velocity model (CVM) by comparing properties of observed and synthetic waveforms up to a frequency of 1 Hz. Basin-edge effects are well reproduced in the Seattle basin, but are less well resolved in the Tacoma basin. Continued study of basin effects in the Tacoma basin would improve the CVM.

In Chapter 3, we investigate whether assuming a fixed shallow depth in the ShakeAlert network-based earthquake early warning system is sufficient to produce accurate ground-motion based alerts for intraslab earthquakes. ShakeAlert currently uses a fixed focal depth of 8 km to estimate earthquake location and magnitude. This is an appropriate way to reduce computational costs without compromising alert accuracy in California, where earthquakes typically occur on shallow crustal faults. In the Pacific Northwest (PNW), however, the most common moderate-magnitude events occur within the subducting Juan de Fuca slab at depths between ~35 and 65 km. Using a dataset of seismic recordings from 37 M_w 4.5+ intraslab earthquakes from the PNW and Chile, we replay events through the Earthquake Point-Source Integrated Code and

eqInfo2GM algorithms to estimate source parameters and compute modified Mercalli intensity (MMI) alert threshold contours. Each event is replayed twice—once using a fixed 8 km depth and a second time using the actual catalog earthquake depth. For each depth scenario, we analyze MMI III and IV contours using various performance metrics to determine the number of correctly alerted sites and measure warning times. We determine that shallow depth replays are more likely to produce errors in location estimates of greater than 50 km if the event is located outside of a seismic network. When located within a seismic network, shallow and catalog depth replays have similar epicenter estimates. Results show that applying catalog earthquake depth does not improve the accuracy of magnitude estimates or MMI alert threshold contours, or increase warning times. We conclude that using a fixed shallow earthquake depth for intraslab earthquakes will not significantly impact alert accuracy in the PNW.

Chapter 4 is an evaluation of ShakeAlert performance for *M* 9 megathrust earthquakes in the PNW. Since there are no recordings of large magnitude earthquakes on the CSZ, we use synthetic seismograms from a suite of 30 simulated *M* 9 earthquake scenarios on the Cascadia megathrust with varying hypocenters, down-dip rupture extents, slip distributions, and locations of high-stress drop subevents to test the performance of ShakeAlert algorithms. We implement new features not currently set up in the operational ShakeAlert system (version 2.1.5), such as an upgraded version of the FinDer algorithm capable of utilizing generic and fault specific templates, a set of generic crustal templates that increase the maximum allowed rupture length from 300 km to 1362 km, a new version of the eqInfo2GM algorithm that uses precomputed distance tables to determine the spatial extent of ShakeAlert MMI alert threshold contours, and contour distance tables generated with the Next Generation Attenuation – West 2 ground motion models. We measure the timeliness and accuracy of source estimates and evaluate the

performance of ShakeAlert alert contours using a station-based alert classification scheme. We also a develop a population-based alert classification method by aligning a 30 arc-second resolution population grid with Voronoi diagrams computed from the classified sites for each scenario. Using raster statistics, we estimate the approximate population in the PNW that would receive timely accurate alerts during an offshore *M* 9 earthquake. We also observe the range of expected warning times with respect to the spatial distribution of the population. Our results, disaggregated by MMI alert threshold, show that most of the population could receive alerts with positive warning times for an alert threshold of MMI III, but that the number of late and missed alerts increases as the MMI alert threshold is increased. For MMI V, an average of just under 60% of the population would be alerted prior to the arrival of threshold level shaking. Large regions of late and missed alerts for alert thresholds MMI IV and V are caused by delays in alert updates, inaccurate FinDer source estimates, and undersized alert contours. We also evaluate whether some end-users in the MMI V (moderate shaking) late alert zones could receive an alert prior to experiencing MMI VI (strong) or MMI VII (very strong) level shaking. Correct timely alerts increase by about 10% for MMI V using this warning time definition. Finally, we investigate an alerting strategy where ShakeAlert sends out an alert to the entire PNW region when the system detects at least an *M* 8 earthquake on the coast. This strategy eliminates all missed alerts and all late alerts except at sites close to the epicenter. The mean percentage of timely correct alerts is similar to using an alert threshold of MMI III, but the range of warning times is significantly greater and there is less risk of over-alerting in California.

Table of Contents

I Introduction

The Cascadia subduction zone (CSZ) is formed by the convergence of the Juan de Fuca plate and the North American plate. It extends from Cape Mendocino, California to Vancouver Island, British Columbia. Much of the Pacific Northwest (PNW) region lies just east of the offshore Cascadia fault, creating a complex tectonic environment that is susceptible to three types of seismicity: crustal earthquakes, intraslab earthquakes within the subducting Juan de Fuca slab, and interface earthquakes on the Cascadia megathrust. Several sedimentary basins throughout the Puget Lowlands, Washington and Willamette Valley, Oregon may increase the risk to the regional population. Interactions between seismic energy from local earthquakes and basin structure can amplify seismic waves, increasing the intensity and duration of shaking experienced at sites within the basins.

Paleoseismic evidence (Atwater, 1987) and turbidite records (Goldfinger *et al.*, 2012) reveal a minimum of a 10,000 year history of *M* 8+ earthquakes on the Cascadia megathrust fault. Full margin ruptures along the entire length of the 1100 km subduction zone, producing *M* ~9 earthquakes, are expected to occur approximately every 500 years (Goldfinger *et al.*, 2012). The last known megathrust earthquake on the CSZ produced a trans-Pacific tsunami in Japan. From historical records of this tsunami, Satake *et al.* (1996) concluded that the earthquake occurred on January 26, 1700. Numerical models of the tsunami imply an estimated magnitude between *M* 8.7 and *M* 9.2 for this event (Satake *et al.*, 2003).

Though the CSZ has a history of generating very large magnitude events, the PNW has uncommonly low levels of background seismicity, particularly for moderate-to-large magnitude earthquakes. The Pacific Northwest Seismic Network (PNSN), which monitors earthquake activity in Washington and Oregon, has only recorded 24 *M* 5+ earthquakes since 1980, the

largest being the 2001 *M* 6.8 Nisqually intraslab earthquake. The largest earthquake to be definitively located on the Juan de Fuca plate interface is an *M* 4.9 recorded in 2004 off the coast of Oregon (Tréhu *et al.*, 2008).

A combination of significant seismic hazards and low observed seismicity presents an interesting challenge for researchers seeking to improve seismic hazard mitigation measures in the PNW. In this dissertation, we strive to contribute to the understanding of regional seismic hazards using observations and ground-motion simulations of small-to-moderate magnitude PNW earthquakes. We also endeavor to refine risk mitigation efforts using PNW and global intraslab earthquakes and ground-motion simulations of *M* 9 scenario earthquakes on the CSZ.

In Chapter 2, we characterize sedimentary basin effects in the Seattle and Tacoma basins and validate a 3D seismic velocity model for the PNW using observations from strong-motion recordings from local crustal and intraslab earthquakes (*M* 3.9 – *M* 6.8).

Sedimentary basins can increase seismic hazard during local earthquakes in several ways. When seismic waves interact with sedimentary basins, basin-edges and changes in basin depth can focus incoming *S*-waves, amplifying ground motions; basin-edges can also convert *S*-waves to larger amplitude surface waves; and the impedance contrast between consolidated and unconsolidated rock can amplify incoming *S*-waves and surface waves. There are several sedimentary basins located throughout western Washington and Oregon, including some that underlie major metropolitan areas such as Seattle, Tacoma, and Portland.

Using a spectral ratio method, we calculate basin amplification factors using strong-motion records from sites within and surrounding the Seattle and Tacoma basins. We also survey waveforms from basin sites for evidence of basin-edge generated surface waves that have not been previously documented and to investigate the influence of earthquake depth and source

azimuth on basin amplification. Finally, we attempt to reproduce the basin effects that we observe by computing ground-motion simulations of the earthquakes in our dataset using a finite difference method and a 3D seismic velocity model of the PNW. The simulations serve as a validation exercise for the accuracy of the model. We conclude that shallow crustal and offshore megathrust earthquakes rupturing west of the Puget Lowland will produce greater amplification in the Seattle basin than has been observed for intraslab events. We also advocate for further investigation of the Tacoma basin to improve our understanding of its amplifying effects and refine its characterization in the 3D velocity model since observed basin-edge effects are not well resolved in ground-motion simulations.

In Chapter 3, we assess whether assuming a fixed shallow depth for all earthquake locations predicted by ShakeAlert—the earthquake early warning (EEW) system for the West Coast of the United States—will significantly impact the accuracy of alerts for intraslab events in the PNW by playing a dataset of five local (M 4.7 – M 6.8) and 32 Chilean (M 5.1 – M 6.7) intraslab earthquakes through the ShakeAlert software.

Deep intraslab earthquakes in Cascadia are typically caused by faulting driven by down-dip directed tension in the Juan de Fuca slab. Generally, these events occur beneath the Puget Lowland region of Washington (Bostock *et al.*, 2019) and are the most frequently occurring moderate-magnitude earthquakes in the PNW. Three M 6.5+ intraslab events have struck the Puget Sound region since 1949: the 1949 M 7.1 Olympia earthquake, the 1965 M 6.5 Puget Sound earthquake, and the 2001 M 6.8 Nisqually earthquake (Cascadia Region Earthquake Workgroup [CREW], 2008).

The ShakeAlert EEW system is a network-based earthquake detection system that uses shaking detected at seismic stations to estimate the magnitude and location of an earthquake in

real time, estimate the spatial extent and intensity of ground shaking, and send out the information to delivery mechanisms that will issue alerts to end-users so they can perform mitigating actions prior to the arrival of shaking. It was originally designed for detecting earthquakes in California, where most seismicity occurs on shallow crustal faults. Even though the alerting region has expanded to include Washington and Oregon, the system is still configured to assume that all earthquake types—including intraslab earthquakes in the PNW, which initiate at depths between ~35 to 65 km (Petersen *et al.*, 2014)—occur at a depth of 8 km. By comparing the outcomes from playing our dataset of PNW and Chilean intraslab earthquakes twice through the ShakeAlert system—once using a fixed depth of 8 km for each event and a second time using actual earthquake depth—we measure the magnitude, epicentral location, and ground-motion prediction errors introduced by a shallow depth assumption using various performance metrics and a station-based alert classification scheme. Our results show that ShakeAlert location estimates are similar regardless of depth accuracy as long as the earthquake is located within a seismic network and that accurate depth does not improve magnitude estimates or predictions of the spatial extent of ground shaking, or increase warning times. We conclude that using a fixed shallow earthquake depth for intraslab earthquakes will not significantly impact alert accuracy and timeliness in the PNW.

In Chapter 4, we conduct a population-based performance evaluation of the ShakeAlert EEW system for megathrust earthquakes in the PNW using synthetic seismograms from 3D ground-motion simulations of hypothetical *M* 9 earthquakes on the CSZ.

In this study, we seek to develop realistic expectations of ShakeAlert performance for the population in the PNW during an offshore megathrust earthquake given that the current system is optimally configured to detect, characterize, and alert for onshore shallow crustal earthquakes.

Building off of the station-based alert classification scheme used to measure the quality of EEW alerts in Chapter 3, we develop a population-based alert classification scheme that considers the spatial distribution of the PNW population when measuring alert quality and the range of expected warning times for this type of event. We assess the outcomes of 30 *M* 9 scenarios for modified Mercalli intensity alert thresholds III, IV, and V. We conclude that alerting the whole region that may experience MMI V level shaking for an *M* 9 earthquake as soon as ShakeAlert estimates an *M* 8 offshore event could compensate for the difficulties the system has in characterizing an *M* 9 rupture in near real-time. This could reduce seismic risk by significantly increasing the number of people that may receive alerts for this type of earthquake with enough warning time to perform mitigating actions, such as drop, cover, and hold on.

1 REFERENCES

Atwater, B. F. (1987). Evidence for great Holocene earthquakes along the outer coast of Washington state, *Science* **236**, 942–944.

Bostock, M. G., N. I. Christensen, and S. M. Peacock (2019). Seismicity in Cascadia, *Lithos* **332–333**, 55–66, doi: 10.1016/j.lithos.2019.02.019.

Cascadia Region Earthquake Workgroup (CREW) (2008). Cascadia deep earthquakes, Cascadia Region Earthquake Workgroup, 26 pp., available at https://www.dnr.wa.gov/Publications/ger_ofr2008-1_cascadia_deep_eq.pdf (last accessed March 2022).

Goldfinger, C., C. H. Nelson, A. E. Morey, J. R. Johnson, E. Karabanov, J. Gutierrez-Pastor, A. T. Eriksson, E. Gracia, G. Dunhill, *et al.* (2012). Turbidite event history—Methods and implications for Holocene paleoseismology of the Cascadia subduction zone, *U.S. Geol. Surv. Profess. Pap. 1661-F*, 170 pp.

Petersen, M. D., M. P. Moschetti, P. M. Powers, C. S. Mueller, K. M. Haller, A. D. Frankel, Y. Zeng, S. Rezaeian, S. C. Harmsen, O. S. Boyd, *et al.* (2014). Documentation for the 2014 update of the United States national seismic hazard maps, *U.S. Geol. Surv. Open-File Rept. 2014-1091*, 243 pp., doi: 10.3133/ofr20141091.

Satake, K., K. Shimazaki, Y. Tsuji, and K. Ueda (1996). Time and size of a giant earthquake in Cascadia inferred from Japanese tsunami records of January 1700, *Nature* **379**, no. 6562, 246–249, doi: 10.1038/379246a0.

Satake, K., K. Wang, and B. F. Atwater (2003). Fault slip and seismic moment of the 1700 Cascadia earthquake inferred from Japanese tsunami descriptions, *J. Geophys. Res.* **108**, no. B11, 2535, doi: 10.1029/2003JB002521.

Tréhu, A. M., J. Braunmiller, and J. L. Nabelek (2008). Probable low-angle thrust earthquakes on the Juan de Fuca–North America plate boundary, *Geol.* **36**, no. 2, 127, doi: 10.1130/G24145A.1.

II Basin amplification effects in the Puget Lowland, Washington, from strong-motion recordings and 3D simulations

The content of this chapter is published in:

Thompson, M., E. A. Wirth, A. D. Frankel, J. R. Hartog, and J. E. Vidale (2020). Basin amplification effects in the Puget Lowland, Washington, from strong-motion recordings and 3D simulations, *Bull. Seismol. Soc. of Am.* **110**, no. 2, 534–555, doi: 10.1785/0120190211.

1 INTRODUCTION

The Pacific Northwest is vulnerable to earthquakes generated by crustal faults, deep intraslab normal-faulting, and megathrust events along the Cascadia subduction zone (CSZ). Seismic hazard is increased by the presence of several sedimentary basins located within the Puget Lowland, the most densely populated region of Washington State. The 3D geometry of basins can affect the behavior of seismic waves in multiple ways. Basin-edges and changes in basin depth can focus *S*-waves, thus amplifying ground motions; basin-edges may convert incoming *S*-waves to larger amplitude surface waves; and the impedance contrast between consolidated and unconsolidated rock can amplify incoming *S*-waves and surface waves. These processes can increase shaking intensity and duration at sites within sedimentary basins.

Sedimentary basin effects within the Seattle basin have been studied extensively (e.g., Frankel *et al.*, 2002, 2009; Pratt *et al.*, 2003; Pratt and Brocher, 2006) from recordings of local and teleseismic earthquakes. Frankel *et al.* (2002) used strong motion recordings of the 2001 M_w 6.8 Nisqually earthquake and its M_L 3.4 aftershock to study site response and basin effects in the city of Seattle, Washington. Stiff-soil sites were amplified by a factor of 1.3-2.4 at periods of 1.0-2.0 s relative to a soft rock reference site located just south of the Seattle fault zone (SFZ).

They observed that layers of deep (> 500 m) unconsolidated sediments in the Seattle basin produced larger ground-motion amplitudes than sites outside of the basin with similar V_{S30}. Record sections also showed surface waves generated at the basin edge developing within the basin.

In a similar study, Pratt *et al.* (2003) observed amplification factors ranging from 8-16 for frequencies of 0.2-0.8 Hz in the Seattle basin relative to crystalline bedrock reference sites west of the basin from the 1999 Chi-Chi Taiwan earthquake recorded by the 1999 Seismic Hazard Investigations of Puget Sound (SHIPS) array deployed in an east-west line across the Seattle basin. From recordings of 2 local earthquakes (M_D 2.1 and 2.8) and 5 blasts, they measured amplification up to a factor of 4 relative to crystalline bedrock between 1 and 10 Hz. Amplification decreased with increasing frequency above 1 Hz. Above 7 Hz, amplitudes were lower at Seattle basin sites compared to crystalline bedrock sites.

Pratt and Brocher (2006) used recordings of 3 local earthquakes (M_D 1.6-2.8) from the 1998 SHIPS array, which placed stations throughout the Puget Lowland, to measure 1.5-20 Hz amplification in lowland basins (i.e., the Seattle, Tacoma, and Everett basins). Spectral ratios showed peak amplification factors of 2-6 between frequencies of 3-6 Hz relative to bedrock reference sites outside of the Puget Lowland. They noted decreasing amplification within the basins with increasing frequencies above 6 Hz, similar to the observations from Pratt *et al.* (2003).

3D ground-motion simulations have also been used to investigate ground-motion amplification due to the Seattle basin. Using a 3D velocity model that includes the Puget Lowland basins and includes the impedance contrast imposed by the SFZ on the southern boundary of the Seattle basin, Frankel *et al.* (2009) produced synthetic seismograms of five local

earthquakes, including the 2001 Nisqually earthquake, that match the timing and character of basin-edge surface waves observed in recordings. Synthetic waveforms also showed evidence of *S*-wave focusing along the southern boundary of the basin near an area that experienced localized damage to unreinforced brick chimneys (Booth *et al.*, 2004; Stephenson *et al.*, 2006) during the Nisqually earthquake. They also determined, from plots of observed 1 Hz amplification at Seattle basin sites with respect to the back azimuth to each earthquake, that the highest average amplifications are produced by events south and southwest of the basin. Average 1 Hz amplification from earthquakes approaching the basin from the southwest is about a factor of 2-3 relative to reference sites with thin soil over rock.

Basin-edge generated surface waves in the Seattle basin, which contribute to the overall amplification of ground motions, have been well-documented by Frankel *et al.* (2002, 2009). In general, basin-edge generated surface waves are identified based on the timing of the phase arrival after the *S*-wave, the lower frequency content compared to earlier phases, and either the absence of surface waves outside of the basin or significantly smaller surface wave amplitudes. They demonstrated that basin-edge converted phases develop in the Seattle basin when seismic energy crosses the sharp impedance contrast created by the SFZ. No observations of basin-edge phases have been documented for the Tacoma basin.

Here, we focus on sedimentary basin effects in the Puget Lowland recorded at Pacific Northwest Seismic Network (PNSN) and U.S. Geological Survey (USGS) strong-motion stations on stiff-soil glacial deposits. Since 2010, the number of PNSN strong motion and broadband stations in western Washington has increased dramatically (i.e., ~100 new sites), improving coverage of the Seattle, Tacoma, Everett and Muckleshoot basins. This increased station

coverage—which was absent during previous studies—provides an opportunity to improve our understanding of sedimentary basin effects in this region.

The goals of this project are to (1) quantify 1-5 s period amplification in the Seattle and Tacoma basins using a spectral ratio method, (2) survey local earthquake recordings for evidence of basin-edge converted surface waves that have not been previously documented, and (3) validate a 3D Cascadia velocity model (CVM) developed by Stephenson *et al.* (2017) through numerical simulations of local earthquakes. The CVM was created to support earthquake hazard and ground-motion studies of magnitude 8-9 interface earthquakes on the CSZ (e.g., Frankel *et al.*, 2018; Wirth *et al.*, 2018), large crustal (e.g., SFZ; Frankel *et al.*, 2007) and intraslab earthquakes (Frankel *et al.*, 2009). By comparing the results of numerical simulations to local strong motion recordings, we can determine how well the velocity model reproduces expected sedimentary basin effects and where improvements may be needed.

2 GEOLOGIC SETTING

The Seattle basin, the deepest basin in the Puget Lowland, reaches a maximum depth of about 7 km adjacent to its southern edge. At the northern end, the Seattle basin thins to 2.5 km (Snelson *et al.*, 2007) and is bounded by the Kingston Arch, a structural high that is covered by a 3 km layer of sedimentary rock (Brocher *et al.*, 2001). The Seattle basin is filled with low-density Eocene to Miocene sedimentary rock overlain by approximately 1 km of unconsolidated Quaternary sediment (Barberopoulou *et al.*, 2006; Pratt and Brocher, 2006; Snelson *et al.*, 2007). Several studies have shown that the unconsolidated top layer of the Seattle basin is a major contributor to seismic wave amplification (Barberopoulou *et al.*, 2006; Frankel *et al.*, 2009; Pratt *et al.*, 2003; Pratt and Brocher, 2006).

The SFZ forms the southern boundary of the Seattle basin. It consists of multiple east-west trending fault strands (**Fig. 2.1a**) and contains at least three south-dipping thrust faults (Nelson *et al.,* 2003). Motion on these faults has displaced Eocene volcanic and sedimentary rocks northward (Blakely *et al.*, 2002) where they create a strong impedance contrast with the sediments within the Seattle basin.

The Seattle uplift lies between the Seattle and Tacoma fault zones and marks the northern terminus of the Tacoma basin. Seismic tomography of the upper crustal structure of the Puget Lowland from the 1998 Seismic Hazards Investigation in Puget Sound (SHIPS) experiment portrays the Tacoma basin as asymmetric, deepening to the north (Brocher *et al.*, 2001). The deepest part of the basin, along Tacoma fault zone (TFZ), reaches a depth of 6-7 km. The basin is bounded to the west by the Olympic Mountains and to the southwest by the Olympia structure.

3 EARTHQUAKES

We selected five earthquakes, including the 2001 M_w 6.8 Nisqually event, from some of the largest earthquakes recorded at local strong-motion stations in the Puget Lowland to analyze in this study. The Nisqually earthquake, events 1, 2, and 4 are normal-faulting intraslab events within the Juan de Fuca Plate (**Fig. 2.1a**). Event 3 is a shallow crustal earthquake east of the Olympic Mountains. **Table 2.1** lists the origin time, magnitude, and hypocentral location of the five earthquakes.

Seismic recordings of the five earthquakes analyzed in this study were collected from digital three-component strong-motion stations. The number of available stations varies for each event as sensor coverage has increased over time. For this study, we focus on areas that are expected to exhibit linear site response and have excluded all sites on soft soils (e.g., alluvium and artificial fill), because shallow soils less than 100 m thick are not included in the CVM.

Recordings are converted from counts to m/s^2 by dividing out the instrument sensitivity from individual components. The data are demeaned and integrated to velocity (m/s) seismograms. Time series from PNSN NetQuakes stations are down-sampled from 200 Hz to 100 Hz to match the sample rate of the rest of the seismograms.

4 OBSERVATIONS OF GROUND-MOTION AMPLIFICATION IN THE SEATTLE AND TACOMA BASINS

We measure amplification over the deepest portion of the Seattle basin and within the boundaries of the Tacoma basin by calculating Fourier spectral ratios with the method of Frankel *et al.* (2009). The deepest portion of the Seattle basin is defined as the region where the depth to a shear-wave velocity of 2500 m/s is 6000 m or greater within the CVM (**Fig. 2.1**). We use two references sites, BRI and SEW, located along the SFZ (white squares in **Fig. 2.1b**). BRI is characterized by thin soil over rock and SEW is a soft rock site characterized by a 10 m layer of soil over rock with V_{S30} = 433 m/s (Williams *et al.*, 1999).

A Fourier spectral ratio, $A_i(f)$, is determined from the spectral amplitude, $S_i(f)$, of a basin site and the spectral amplitude, $S_{ref}(f)$, of a reference site with equation

$$A_i(f) = \frac{S_i(f)R_i}{S_{ref}(f)R_{ref}} e^{-\pi f(R_{ref}-R_i)/QV_s}. \quad (1)$$

R_{ref} and R_i are the hypocentral distances of the reference site and basin site, respectively. The average shear-wave velocity of the crust, V_s, is assumed to be 3.5 km/s. The spectral amplitudes are computed from the geometric average of the two horizontal seismogram components using a 40 s window beginning 10 s after the *P*-wave arrival for all earthquakes except the regional event, where we extend the window to 60 s to accommodate for greater earthquake-to-basin distances. Amplitude spectra are corrected for $1/R$ geometric spreading (R is hypocentral distance) and Q using $Q(f) = 380f^{0.39}$ (Atkinson, 1995), and smoothed with a Gaussian

function.

The distance between sites within the deepest portion of the Seattle basin and the reference sites is small compared to the hypocentral distance between these sites and earthquakes analyzed in this study. Therefore, rupture directivity and focal-mechanism effects should not significantly influence spectral ratios at Seattle basin sites (Frankel *et al.*, 2002). There is greater distance between Tacoma basin sites and reference sites, which could alter spectral ratios in the Tacoma basin. However, viewing results from multiple earthquakes mitigates the impact of individual radiation patterns.

We calculate amplification factors, defined in this paper as the geometric average of the horizontal component spectral ratios at a specific period of interest, at 1 (0.67-1.33 Hz), 2 (0.33-0.67 Hz), 3 (0.22-0.43 Hz), and 5 (0.1-0.3 Hz) seconds period. Events 2 and 3 do not have usable data at periods longer than 2 s and event 4 seismograms are not valid above 3 s due to long period noise in waveforms. We use a 4^{th} order high-pass Butterworth filter to remove long period noise and taper the first 10 s from each time series to remove filtering artifacts prior to computing spectral ratios. **Table 2.2** and **Table 2.3** show the average period-dependent amplification factors for each earthquake in the Seattle and Tacoma basins, respectively**.** A complete list of amplification factors for each earthquake is available in the electronic supplement.

4.1 Seattle basin

In the Seattle basin, the Nisqually earthquake produces amplification between 1 and 5 s relative to either of the reference stations. The highest average amplification is a factor of 2.5 relative to SEW at 3 s. Average amplification computed with respect to BRI is similar at 3-5 s. Amplification relative to BRI differs from factors relative to SEW at 1-2 s by a factor of 1.2-1.4.

There is a large amplitude spike in spectral ratios with respect SEW at ~1.2 s (**Fig. 2.2a**) that is not observed at this period with respect to BRI (**Fig. 2.2b**). The Fourier transform of the horizontal components from SEW reveal a spectral hole around this period, which may artificially increase amplification factors.

Event 1 produces similar average amplification to the Nisqually earthquake at 1-5 s in the Seattle basin. The highest average amplification factors occur at 2-3 s for this event (**Fig. 2.2c,d**). Amplification factors relative to BRI are similar to factors relative to SEW except for a factor of ~1.3 difference around 2 s. Event 2, located at a similar hypocentral distance to the Seattle basin as event 1, produces amplification around a factor of 1.8 relative to SEW at 1-2 s. Recordings from BRI were unavailable for this event.

The number of stations in the Seattle basin increases from around 10 to 20 over the deepest part of the basin for events 3 and 4. The average amplification factors for event 3 were around a factor of 2.3 at 1 s relative to BRI or SEW. At 2 s, the average amplification relative to SEW is a factor of 1.6 larger than amplification relative to BRI. There are two peaks visible in spectral ratios relative to SEW around 2 s (**Fig. 2.2e**), which are not observed in the spectral ratios relative to BRI (**Fig. 2.2f**). Though the range of amplification factors is different between the two reference stations at 2 s, by plotting amplification factors in map view (**Fig. 2.3**), we can see a similar spatial pattern of higher amplification near the center of the basin that decreases toward the southern boundary when using either reference station. Event 4 generates some amplification at 1-3 s relative to either reference station, though the average amplification is generally lower than the other earthquakes.

4.2 Tacoma basin

For earthquakes prior to 2010 (Nisqually, event 1, and event 2), there is only a single strong motion station (UPS) within the boundaries of the Tacoma basin. We see no amplification at this site with respect to either reference site for the Nisqually earthquake. For event 1, the amplification relative to SEW is around a factor of 3.0 between 2-5 s, increasing to a factor of 3.8 at 1 s. Amplification at UPS for event 2 with respect to SEW is a factor of 1.7 at 1 s, but exhibits no amplification at 2 s.

Station coverage in the Tacoma basin increased to eight stations prior to events 3 and 4. Event 3 produces average amplification around a factor of 2.3 at 1 s relative to either reference station. We see the same peak in spectral ratios relative to SEW (**Fig. 2.4a**) around 2 s that is not seen in spectral ratios relative to BRI (**Fig. 2.4b**) resulting in the same factor of 1.6 difference in amplification that was observed in the Seattle basin at this period. At 2 s, the average amplification with respect to SEW is a factor of 2.8. Event 4 produces little-to-no amplification relative to either reference station (**Fig. 2.4c,d**).

5 OBSERVED BASIN-EDGE SURFACE WAVES

To identify basin-edge converted phases in horizontal component seismograms, we plot record sections along several azimuths from the epicenter of each earthquake through the Seattle and Tacoma basins and look for a large amplitude pulse following the *S*-wave at inside-basin stations. Basin-edge surface waves observed in the Seattle basin during the Nisqually earthquake have been documented previously in Frankel *et al.* (2002, 2009) and will not be discussed in this paper. However, we do note that no basin-edge surface waves were detected in the Tacoma basin for this event.

Recordings from event 2 near the center of the Seattle basin show surface waves with large amplitudes relative to stations outside of the basin. The record section in **Fig. 2.5a** shows two examples of stations (CTR and LAP) displaying large amplitude surface waves relative to the shear wave amplitudes at station HOLY, just south of the SFZ. **Figure 2.5a** also shows the development of possible basin-edge surface waves at station UPS in the Tacoma basin. This is the only event where we document a possible basin-edge generated phase in the Tacoma basin.

The complexity of waveforms recorded from events 1, 3, and 4 makes detecting basin-edge effects more challenging. We do observe the development of basin-edge surface waves in the Seattle basin during event 1 on the N-S component of station BHD (just north of the SFZ; **Fig. 2.5b**). While there is significant *S*-wave amplification and resonance at station UPS in the Tacoma basin for event 1, we do not detect any basin-edge converted waves. We also identify several likely basin-edge surface waves for event 3 at stations in the Seattle basin at azimuths 87˚-93˚ from the epicenter (**Fig. 2.5c**). Stations at azimuths less than 87˚ within the Seattle basin display more complicated waveforms making basin-edge effects difficult to identify. In the Tacoma basin, we again observe *S*-wave amplification, but do not detect any basin-edge surface waves. There are no clear examples of basin-edge surface waves visible in event 4 seismograms from the Seattle or Tacoma basin stations.

6 VALIDATING THE CVM

6.1 3D seismic velocity model

By computing synthetic seismograms based on observed local earthquakes, we can validate a 3D velocity model that represents the CSZ (Stephenson *et al.*, 2017). The velocity model extends from 40.2°N to 50°N latitude, 122°W to 129°W longitude, and approximately 60 km depth. The primary focus of this paper is the area encompassing western Washington

(approximately 46.8°N to 49.0°N latitude, 122°W to 124°W longitude). The model contains simplified geologic units that include continental sedimentary basins, continental crust, continental mantle, oceanic sediments, oceanic crust, and oceanic mantle. The minimum shear-wave velocity within the continental sedimentary basins is restricted to 600 m/s (Stephenson *et al.*, 2017).

The SFZ is approximated within the velocity model as a distinct velocity contrast imposed across the frontal strand (**Fig. 2.6**), the northern-most thrust fault of the SFZ. The surface trace of the frontal strand, extracted from Blakely *et al.* (2002), is projected to a depth of 20 km with a 45˚ dip to the south (Frankel *et al.*, 2009; Stephenson, 2007). The dip angle is a median value based on the range of dips published in various seismic reflection surveys (e.g., Pratt *et al.*, 1997; Johnson *et al.*, 1999; ten Brink *et al.*, 2002; Brocher *et al.*, 2004).

The velocity model is composed of three layers each with distinct discretization. The top layer has 200 m horizontal grid-spacing and 100 m vertical grid-spacing from the surface to 1200 m. Grid-spacing increases to 300 m horizontal and vertical down to 9900 m depth in the middle layer. The bottom layer increases to 900 m horizontal and vertical grid-spacing down to 60 km depth. Topography is assumed flat.

Frankel *et al.* (2009) used Version 1.3 (Stephenson, 2007) of the CVM to compute 3D ground-motion simulations of the Nisqually earthquake. Here, we use Version 1.6, which has incorporated several changes to the geologic structure and properties within the volume. We briefly summarize these changes, but further details are provided in Stephenson *et al.* (2017). In western Washington, the surficial contact between Quaternary and Tertiary sediments has been redefined at a higher resolution according to the Schuster (2005) geologic map. Tomographic results from Moschetti *et al.* (2007) were used to modify V_S for the continental crust and mantle.

The surface geometry of the Juan de Fuca slab and the base of the subducting oceanic crust were updated with data from McCrory *et al.* (2012) and Blair *et al.* (2013). Note that the velocity structure of the Seattle basin has not been significantly changed between the two versions of the model.

6.2 Ground-motion simulations

We use a finite difference program (Liu and Archuleta, 2002) to compute 3D ground-motion simulations for the five earthquakes listed in **Table 2.1**. This code takes advantage of variable grid spacing to decrease computation time; shallow layers, where lowest seismic velocities are found, are represented with a fine grid-spacing, expanding to coarser grid-spacing deeper in the model box (i.e., higher seismic velocities). The code uses a velocity-stress formalism and is 4^{th} order accurate in space and 2^{nd} order accurate in time. Synthetic seismograms are sampled at 100 Hz.

The Nisqually earthquake simulation is computed with the same source model used in Frankel *et al.* (2009). The model is made up of two spatially coincident point sources separated in time by 1.5 s, with scalar moments of 0.7×10^{19} N · m and 1.1×10^{19} N · m, respectively. Events 1-4 are modeled as single point sources. All point sources are described using a Liu (Liu and Archuleta, 2002) source time function. Origin time, magnitude, hypocentral location, strike, dip, and rake are from the PNSN earthquake catalog. Rise times are chosen based on the best fit to observations. Source parameters are listed for all events in **Table 2.4**.

6.3 Comparison of peak ground velocities and arrival times

We validate the CVM by comparing properties of the synthetic seismograms computed from 3D ground-motion simulations to those of the earthquake recordings. Computational limitations and the resolution of the CVM precludes matching the observational data wiggle-for-

wiggle up to 1 Hz. To assess the accuracy of the velocity model as a tool for predicting earthquake ground motions, we are most interested in the accuracy of the initial *S*-arrival times, peak amplitudes, and the timing and amplitude of basin-edge surface waves. To quantify the fit of the synthetics for each event, we compute the natural log bias and standard deviation of the synthetic and observed peak ground velocities (PGVs) with the method described in Abrahamson *et al.* (1990). Observed and synthetic seismograms are filtered with a 3rd order bandpass Butterworth filter. The lower cutoff frequency is chosen to match the corner frequency selected to remove long period noise from the observed waveforms. The upper cutoff frequency is 1 Hz to match the passband of validity of the synthetic seismograms. Example synthetic and observed seismograms for each earthquake are shown in **Figures 2.7-2.11** and a comparison of predicted and observed PGVs for each event is shown in **Figure 2.12**. PGVs are measured from the geometrically averaged horizontal-component waveforms.

Synthetic seismograms of the Nisqually earthquake (**Fig. 2.7**) capture the general character of actual recordings. Synthetics also show basin-edge surface waves where they are observed in recorded data. All synthetic seismograms show *S*-waves arriving approximately 1.5-2 s early. Synthetic seismograms in **Figure 2.7** have been shifted forward 1.5 seconds to facilitate comparison. The PGV bias is 0.06 natural log units (factor of 1.06) and the standard deviation is 0.36 natural log units (factor of 1.44). The majority of synthetic PGVs match observations within a factor of +/- 2 (**Fig. 2.12a**).

The Puget Lowland region has not changed between V1.3 and V1.6 of the CVM, however modifications to the surface geometry of the Juan de Fuca slab could change synthetic seismograms with deep intraslab sources. Therefore, we compare Nisqually PGVs from simulation results using CVM V1.6 (this study) to synthetic seismograms from Frankel *et al.*

(2009) computed with CVM V1.3 at eight stations (ALO, BHD, BRI, EVA, LAP, THO, SEW, HAL) located in the southern Seattle basin and along the SFZ (**Fig. 2.1b**). For three of the eight stations, we find that simulation results using CVM V1.6 produce PGV amplitudes about a factor of 1.2 larger than synthetics computed with V1.3. The remaining five stations display PGV amplitudes similar to the Frankel *et al.* (2009) synthetics.

Synthetic seismograms of event 1 display shear-wave arrival times that match well with observations (**Fig. 2.8**). Misfit between synthetic and observed PGV is less than a factor of +/- 2 for most stations (**Fig. 2.12b**). We calculate a bias of -0.09 natural log units (factor of 0.91), which indicates that overall the synthetics slightly underpredict observed PGVs between 0.1 – 1 Hz. The standard deviation is 0.4 natural log units (factor of 1.5).

We observe a large late phase (LLP) at some stations in the event 1 synthetics that is not seen in recordings. The phase manifests as a single spike in amplitude around 40 s at five stations (BOW, BRI, MPL, SEW, and SP2) just south of the SFZ and as a large-amplitude resonant phase visible on all three station components beginning around 50 s at four stations (ALO, C43, SEU, and THO) within the Seattle basin. **Figure 2.1b** shows the locations of stations showing the LLP. **Figure 2.8** shows the LLP on all components of SEU and THO and the E-W components of BOW, BRI, and SEW. We will discuss this phenomenon further in the Improvements to the 3D velocity model for Cascadia section of this paper. To prevent the LLP dominating synthetic PGVs, we only compare the first 40 s of observed and synthetic waveforms.

The PGV bias for event 2 is 0.13 natural log units (factor of 1.13) with standard deviation 0.36 natural log units (factor of 1.44). This indicates that synthetics are generally overpredicting PGV for this event between 0.3 – 1 Hz. Misfit between observed and synthetic PGV for event 2 is within a factor of +/- 1.5 for most stations. The basin-edge surface wave that we observe on

the N-S component at UPS is missing from the synthetic waveform (**Fig. 2.9**). We also note synthetic seismograms of event 2 at stations CTR, LAP, and SEA (at similar locations to ALO, C43, SEU, and THO) do not display a LLP around 40 – 50 s (**Fig. 2.9**) though the earthquake location and focal mechanism is similar to event 1 (**Fig. 2.1a**).

Event 3 PGV bias is 0.33 natural log units (factor of 1.39) between 0.3-1 Hz. Standard deviation is 0.35 natural log units (factor of 1.42). Out of 102 stations, 86% of synthetic PGVs fit observations within a factor of +/- 2. Stations with the largest misfits are mostly located along the boundaries of the Puget Lowland and within the Seattle basin. Synthetic seismograms for event 3 show *S*-waves arriving 1-1.5 s late at almost all stations (94/102 stations) and have been shifted forward 1.5 seconds in **Figure 2.10**, relative to observed waveforms, to facilitate comparison.

The PGV bias for event 4 of 0.22 natural log units (factor of 1.25) and standard deviation of 0.43 natural log units (factor of 1.54) indicates an overall overprediction of peak amplitudes for frequencies 0.2-1 Hz. However, when considering only stations within the Tacoma basin, we see a negative bias of -0.08 natural log units (factor of 0.92), indicating a slight underprediction of PGV in the basin. The standard deviation for Tacoma basin sites is 0.17 natural log units (factor of 1.19). 85% of synthetic PGVs match observations within a factor of +/- 2 out of 93 total stations (**Fig. 2.12e**). The majority of stations with a misfit factor of two or greater are located near the northern coast of the Olympic Peninsula and on the Kitsap Peninsula. We observe around a one second delay in synthetic *S*-wave arrivals at several stations. To facilitate comparison with observations in **Figure 2.11**, synthetic seismograms have been shifted forward 1 s.

6.4 Comparison of pseudospectral acceleration response spectra

In addition to comparisons of observed and synthetic PGV, we also quantitatively assess the validity of the CVM by computing the natural log bias of the pseudospectral accelerations for 5% of critical damping computed from the observed and synthetic seismograms for each earthquake with the equation

$$bias(s) = \frac{1}{n}\sum_{i=1}^{n}\left(\frac{\ln RS_{pred_i}}{\ln RS_{obs_i}}\right). \quad (2)$$

RS_{pred_i} and RS_{obs_i} are the geometrically averaged response spectra calculated from synthetic and observed horizontal component seismograms, respectively, for each site. **Figure 2.13** shows the natural-log bias plots for each individual earthquake.

In general, the natural log bias for the Nisqually earthquake is near zero at periods 1-10 s except around 1 s (**Fig. 2.13a**, lighter color). Pseudospectral acceleration may be underpredicted around this period because it approaches the accuracy limits of the 3D simulation, however, we also tested whether the two-point source configuration in our simulations was producing this artifact. We performed a simulation of the Nisqually event with a single point source (M_0 = 1.8×10^{19} N · m, rise time = 4 s, strike = 356˚, dip = 68˚, rake = -90˚). The resulting spectral response bias (**Fig. 2.13a**, darker color) shows that by using a single point source we improve the bias at 1 s but this creates a more significant spectral peak around 3 s. The spectral hole around 1 s is within about -0.5 natural log units (factor of -1.7). Thus, we consider the two-point source configuration more appropriate. Spectral response bias for events 1-4 are all within acceptable tolerance (+/- 0.5) at the periods we are investigating.

7 DISCUSSION

7.1 Amplification in the Seattle and Tacoma basins

There have been several previous site response studies in the Puget Lowland, primarily focused on the Seattle basin (Barberopoulou *et al.*, 2004; Frankel *et al.*, 2002, 2009; Pratt *et al.*, 2003; Pratt and Brocher, 2006). Pratt *et al.* (2003) and Pratt and Brocher (2006) used recordings from the SHIPS experiment, while Frankel *et al.* (2002, 2009) used USGS and UW station recordings of regional earthquakes to look at amplification in the basin. Our study expands upon previous research in the Seattle basin by looking at new earthquakes and additional stations, and documents previously unobserved amplification in the Tacoma basin.

Event 3, the shallowest earthquake used in this study (16 km; **Table 2.1**), produces the highest median amplification factor at 2 s in the Seattle basin compared to the other earthquakes in this study (on average, a factor of 3.2 with respect to SEW; **Table 2.2**). This is likely because the energy from shallow earthquakes is converted more efficiently to surface wave energy (Frankel *et al.*, 2007) and suggests that we can expect higher amplification from shallow crustal earthquakes and megathrust events approaching the Seattle basin from the southwest than from deep intraslab earthquakes. The lowest average amplification is observed for event 4, which is located north of the Seattle basin and thus, seismic energy does not cross the SFZ before entering the basin. It is likely that the absence of basin-edge converted phases contributes to the lower basin amplification values, but we note that we still see moderate amplification up to a factor of 2.5.

We do not observe amplification in the Tacoma basin for every earthquake. The Nisqually earthquake and event 4 produce no amplification relative to either reference station. However, we note that only one seismic station, UPS, was located within the Tacoma basin at

the time of the Nisqually earthquake and thus, may not be representative of ground motions in the entire basin. Frankel *et al.* (2009) notes an area of predicted low peak ground velocities in his simulation of the Nisqually earthquake in a similar location to station UPS, caused by an *S*-wave node in the radiation pattern of the event. Similarly, we suggest that the lack of amplification is due to the *S*-wave node reducing peak velocities at station UPS.

We see amplification in the Tacoma basin during events 1, 2, and 3. Events 1 and 2 occurred when there was only one station in the basin. Event 1 produces the largest amplification factors in the Tacoma basin, at least a factor of 2 greater than event 2, though seismic energy from both events travel across the Olympia structure, and are at similar depths (**Fig. 2.1a, Table 2.1**). Stations in the Tacoma basin record more complicated waveforms during event 1 than event 2 as well. It is possible that path effects, differences in incidence angle as seismic rays enter the basin, or complex basin structure may produce the varying site response at UPS.

7.2 Basin-edge surface waves in the Seattle and Tacoma basins

Basin-edge surface waves are observed in the Seattle basin during four out of our five earthquakes. Event 4, located north of the Puget Lowland, did not produce recognizable basin-edge effects in the Seattle or Tacoma basins; this is likely because seismic waves do not interact with the SFZ before entering the basin. For the other events, stations with identifiable basin surface waves are generally located over the deepest portion of the Seattle basin (where depth to V_S = 2500 m/s is 6000 m) near the southern boundary. For event 3, we are only able to detect basin-edge surface waves in the Seattle basin at stations very close to the SFZ (**Fig. 2.5c**). Raypaths traveling from event 3 to stations in the northern portion of the basin likely avoid any interaction with the SFZ. Our synthetic seismograms generally reproduce basin-edge converted phases in the Seattle basin. Our observations and previous studies (Frankel *et al.*, 2002, 2009)

demonstrate that basin-edge converted phases in the Seattle basin are produced by the sharp velocity contrast created by the SFZ.

In the Tacoma basin, only event 2 reveals a possible basin-edge converted surface wave at UPS (**Fig. 2.5a)**. Event 2 crosses the Olympia structure—a possible fault defined by pronounced gravity and magnetic anomalies (Odum *et al.*, 2016)—before entering the Tacoma basin. It is possible that the impedance contrast along this boundary of the Tacoma basin is capable of generating basin-edge effects. However, we note that seismic energy from event 1 travels a very similar path and does not result in any clearly identifiable basin-edge converted phases. Our ground motion simulations generally reproduce amplification in the Tacoma basin, except for event 2. This suggests that some fine-scale 3D seismic structure around the Olympia structure and western edge of the Tacoma basin may be missing from the CVM.

7.3 Improvements to the 3D velocity model for Cascadia

By comparing properties from synthetic seismograms (e.g., timing of shear-wave arrivals, PGV, and spectral response) produced using real earthquake source parameters and comparing them to station recordings, we are able to show quantitatively that the CVM is doing a reasonable job of reproducing the character of earthquake ground motions. For Nisqually, we see almost a one-to-one match between predicted and observed PGV measurements when averaged across all stations. Bias calculations indicate a slight underprediction of PGV for event 1. Event 2, 3, and 4 generally over-predict PGV by 0.13-0.33 natural log units (factor of 1.13-1.39). This could be mitigated by introducing lateral heterogeneities at the surface of the CVM to scatter earthquake energy, reducing the peak amplitudes of predicted waveforms.

We also see small variations in the timing of *S*-wave arrivals during three events. Synthetic waveforms for the Nisqually earthquake show *S*-waves arriving 1.5-2 s early and many

Event 3 and 4 synthetics display a 1-1.5 s delay in *S*-wave arrivals. Stations with delayed *S*-arrivals are spread throughout the Puget Lowland with no particular spatial pattern for either event. The PNSN locates earthquakes with a simple 1D velocity model, which can lead to errors in event location up to a few kilometers. For example, if we assume an average shear-wave velocity in western Washington of 3.5 km/s, an earthquake located 5 km too shallow or too deep could shift *S*-wave arrivals in synthetic seismograms by up to 1.5 s ($5\ km / 3.5\ km\ s^{-1} = 1.5\ s$). Relocation of the Nisqually, events 3 and 4 hypocenters could improve the timing of synthetic *S*-wave arrivals. Frankel *et al.* (2009) also noted the early arrival of *S*-waves for the Nisqually earthquake and concluded it was because the hypocenter was most likely deeper than 55 km based on inversion results by Ichinose *et al.* (2004).

7.3.1 Large late phase (LLP)

Comparison of recorded and synthetic waveforms reveal some concerning behavior. The event 1 simulation produces a LLP after the *S*-wave arrival, which is not observed in the recorded data (**Fig. 2.8**). The LLP is most prominent between frequencies 0.5 and 0.8 Hz, which is close to the high-frequency accuracy limit of the finite-difference simulations, given the grid spacing and minimum V_S. **Fig. 2.1b** shows the locations of event 1 stations with a LLP in synthetic waveforms.

To identify the origin of the LLP, we examined an animation of wave propagation following event 1. We observe shear-wave energy propagating through the Tacoma basin developing an amplified phase as it crosses the TFZ that continues northeastward along the Seattle uplift. The amplified phase appears collocated with stations BOW, BRI, MPL, SEW, and SP2 around 40 s into the simulation, which matches the timing of the large amplitude spike in

synthetics. The phase arrives ~10 s later at stations ALO, C43, SEU, and THO in the Seattle basin.

It is difficult to tell whether the LLP is caused by overamplification of shear waves within the CVM Tacoma basin or by some other feature along the path of the earthquake since much of what we observe in the animation occurs where actual station coverage is sparse; unfortunately, it is impossible to further constrain the geologic structures in this area without better station coverage. Increasing strong motion or broadband station coverage along the boundaries and over the deepest parts of the Tacoma basin would improve our understanding of its amplifying effects. We note that event 2 and 3D simulations of *M* 9 Cascadia earthquakes (Frankel *et al.*, 2018) do not show these late-arriving phases.

Although the animation appears to suggest that the LLP is generated by structure within the CVM, we performed several tests to rule out other causes. We added random heterogeneities to V_S in the top 1.3 km of the Quaternary sediments within the Puget Lowland, in an attempt to diminish the LLP in the event 1 simulated waveforms. This technique was used by Frankel *et al.* (2011) to account for realistic small-scale variations in V_S not present in the CVM and was shown to cause scattering that reduced the amplitude of basin-edge surface waves in the Seattle basin in 3D simulations. However, in our simulations, this addition did not significantly reduce the LLP in event 1 synthetics. We also performed a simulation with the strike rotated 90 degrees to test for sensitivity to the focal mechanism, which did not diminish the large late phase. A simulation with higher resolution grid-spacing in the CVM also did not noticeably reduce LLP amplitudes.

8 CONCLUSIONS

Our study shows that synthetic seismograms produced with the Cascadia 3D velocity model generally match observed peak ground velocities and basin amplification. Basin-edge effects are well reproduced within the Seattle basin, but are less well resolved in the Tacoma basin. Both the absence of basin-edge surface waves in the Tacoma basin for simulated event 2, and the presence of a LLP in synthetic seismograms for event 1, could be related to inaccuracies in the velocity model near the southwestern boundary of the Puget Lowland. We suggest placing additional seismic stations within and surrounding the Tacoma basin to further investigate the effects we observe in this article.

Perhaps the most significant finding from this study is the observation that shallow local earthquakes that rupture southwest of the Seattle basin (i.e., event 3) tend to generate higher average basin amplification than intraslab events in the Seattle basin (**Table 2.2**). Higher amplification from shallow events could indicate that seismic waves from shallow crustal earthquakes that cross the southwestern boundary of the Seattle basin or a Cascadia megathrust event may be more greatly amplified in the Seattle basin than would be expected from an intraslab event like the Nisqually earthquake. In addition, we also document amplification and possible basin-edge effects in the Tacoma basin. This advocates for increased study of ground motion amplification in other Puget Lowland basins, besides the Seattle basin. Further study of the Tacoma basin and the other Puget Lowland basins is an important step toward accurately predicting ground motions in western Washington for moderate and large magnitude earthquakes.

9 TABLES

Table 2.1: Earthquake information

Earthquake	Date (yyyy/mm/dd)	Time (UTC)	Latitude (degrees)	Longitude (degrees)	Depth (km)	Magnitude
Nisqually	2001/02/28	18:54	47.15	-122.72	52.40	6.8*
Event 1	2001/06/10	13:19	47.17	-123.50	40.24	5.0†
Event 2	2009/10/01	03:10	47.18	-123.23	43.56	3.9‡
Event 3	2014/09/17	10:06	47.56	-123.01	16.20	4.0‡
Event 4	2015/12/30	07:39	48.59	-123.30	52.52	4.8‡

* moment magnitude, † coda magnitude, ‡ local magnitude
All earthquake information is from the Pacific Northwest Seismic Network (PNSN).

Table 2.2: Seattle basin average amplification factors

		1 s		2 s		3 s		5 s	
Earthquake	**Number of Stations**	**BRI**	**SEW**	**BRI**	**SEW**	**BRI**	**SEW**	**BRI**	**SEW**
Nisqually	10	1.7	2.1	2.1	1.5	2.3	2.5	2.1	2.3
Event 1	13	2.0	2.1	2.1	2.7	2.5	2.3	2.1	1.9
Event 2	8	--	1.9	--	1.8	--	--	--	--
Event 3	21	2.4	2.3	2.1	3.3	--	--	--	--
Event 4	14	1.6	1.5	1.9	1.6	1.6	1.6	--	--

Table 2.3: Tacoma basin average amplification factors

		1 s		2 s		3 s		5 s	
Earthquake	**Number of Stations**	**BRI**	**SEW**	**BRI**	**SEW**	**BRI**	**SEW**	**BRI**	**SEW**
Nisqually	1*	0.2	0.3	0.5	0.4	0.5	0.5	0.4	0.5
Event 1	1*	3.6	3.8	2.4	3.1	2.4	3.1	3.3	2.9
Event 2	1*	--	1.7	--	1.0	--	--	--	--
Event 3	8	2.4	2.2	1.8	2.8	--	--	--	--
Event 4	7	0.7	0.7	1.0	0.9	1.1	1.1	--	--

* Amplification factors from station UPS.

Table 2.4: Earthquake source parameters used in 3D simulations

Earthquake	Moment ($N \cdot m$)	Strike (degrees)	Dip (degrees)	Rake (degrees)	Rise Time (s)
Nisqually*	0.7×10^{19}, 1.1×10^{19}	356, 356	68, 68	-90, -100	4.0
Event 1	2.8×10^{16}	130	40	-100	1.5
Event 2	8.9×10^{14}	175	25	-60	0.5
Event 3	6.3×10^{14}	140	60	160	0.5
Event 4	1.5×10^{16}	181	39	-66	1.5

* The Nisqually earthquake source is composed of two spatially coincident point sources separated 1.5 s in time.

10 FIGURES

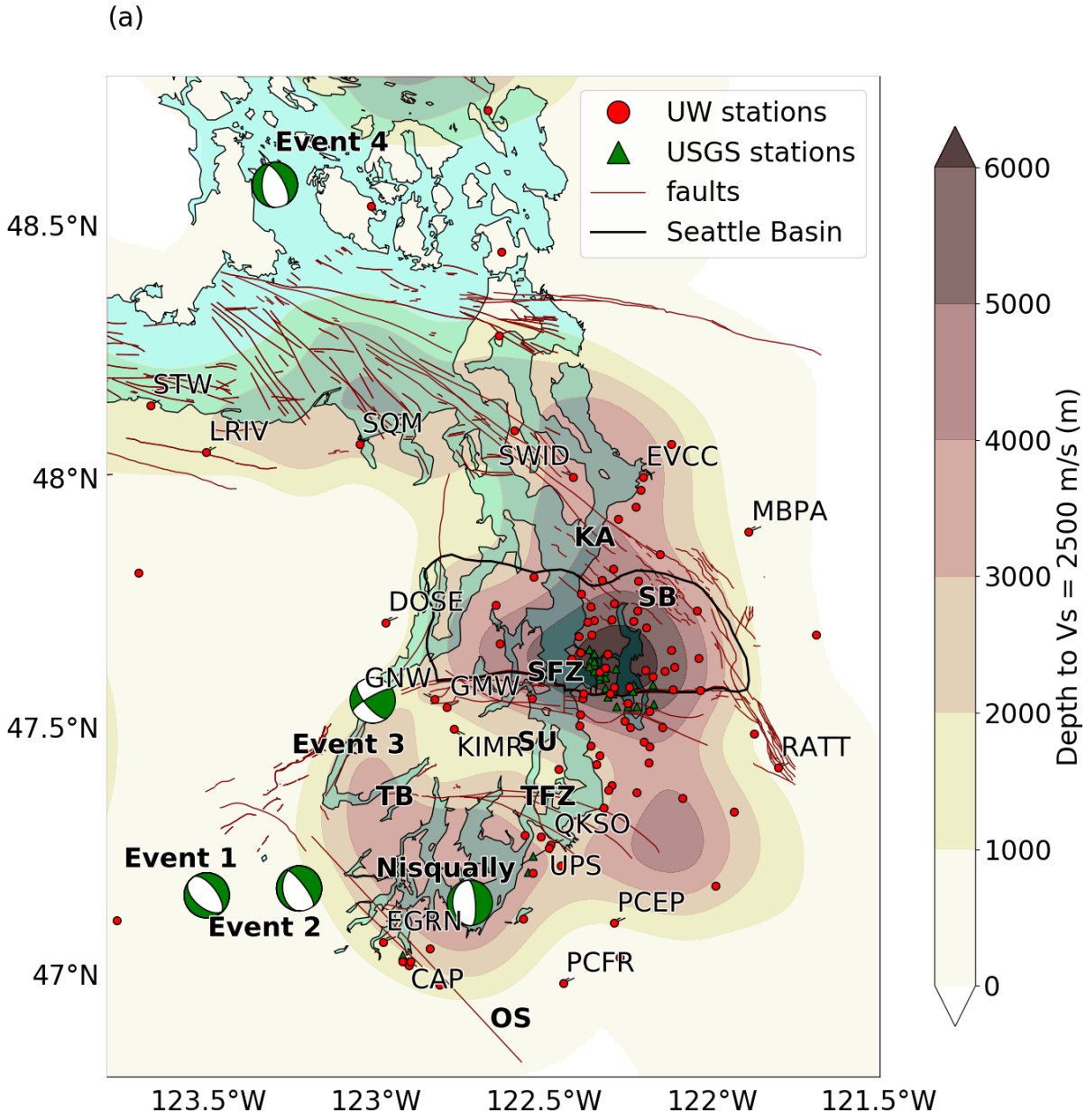
(a)
UW stations
USGS stations
faults
Seattle Basin
Event 4
Event 3
Event 1
Event 2
Nisqually
STW
LRIV
SQM
SWID
EVCC
MBPA
KA
SB
DOSE
GNW
GMW
SFZ
KIMR
SU
RATT
TB
TFZ
OKSO
UPS
PCEP
EGRN
PCFR
CAP
OS
48.5°N
48°N
47.5°N
47°N
123.5°W
123°W
122.5°W
122°W
121.5°W
Depth to Vs = 2500 m/s (m)
6000
5000
4000
3000
2000
1000
0

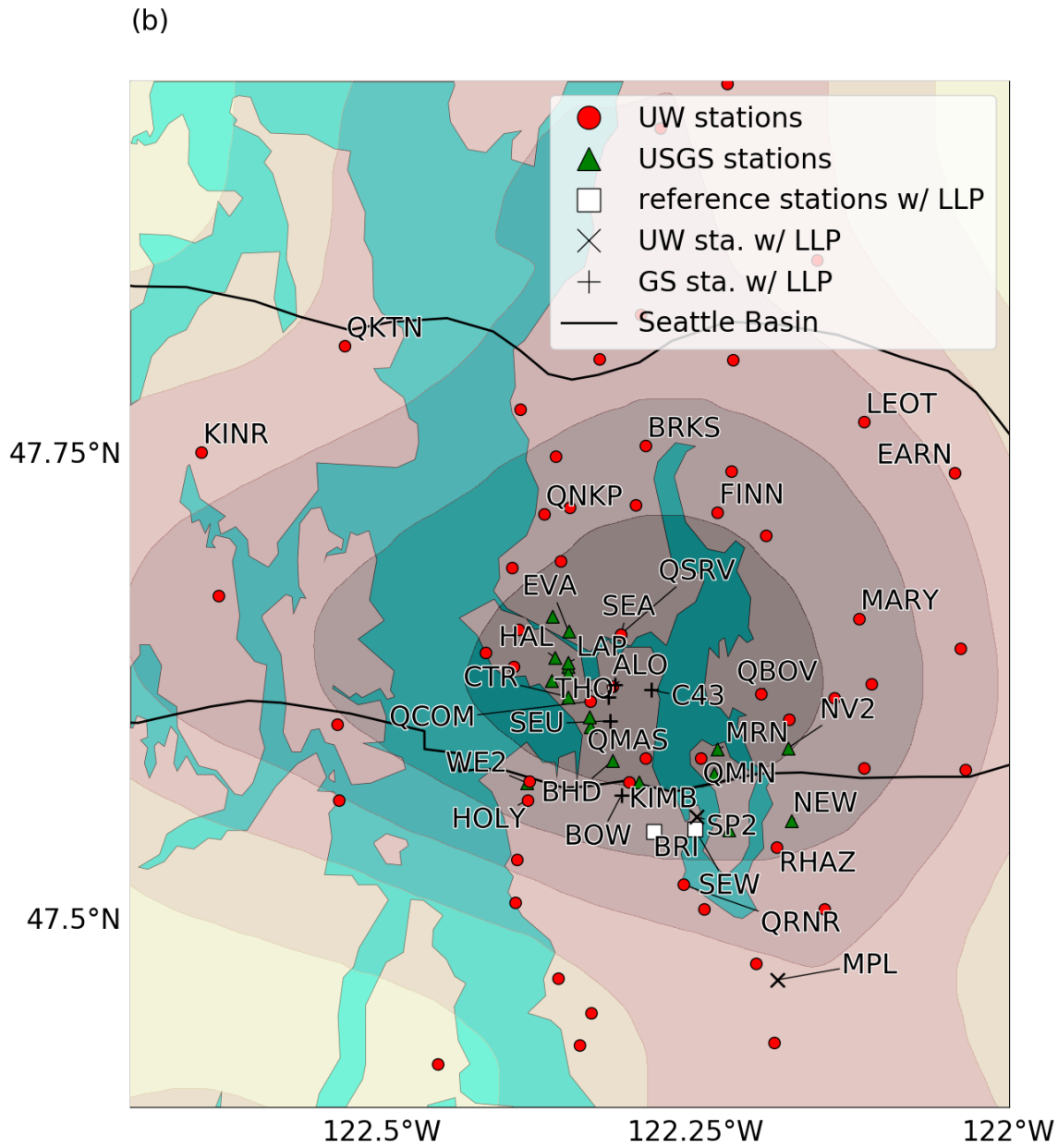

Figure 2.1: (a) Map of western Washington showing the locations and focal mechanisms for the earthquakes used in this study. Sedimentary basins and major geologic features are labeled as follows: KA, Kingston Arch; OS, Olympia structure; SB, Seattle basin; SFZ, Seattle fault zone; SU, Seattle uplift; TB, Tacoma basin; TFZ, Tacoma fault zone. The approximate shape and depth of the Puget Lowland basins are shown with 1000 m contours that represent the depth to V_S = 2500 m/s (depth to bedrock) in the Cascadia velocity model (CVM). The Seattle basin outline is from Richard Blakely. Fault locations are from the U.S. Geological Survey (USGS) Quaternary fault and fold database for the United States (U.S. Geological Survey, 2018). Labeled sites are stations discussed in this article. **(b)** The same map as (a) zoomed-in on the Seattle basin. Stations that display a large late phase (LLP) in the event 1 simulation are labeled "w/ LLP" in the legend.

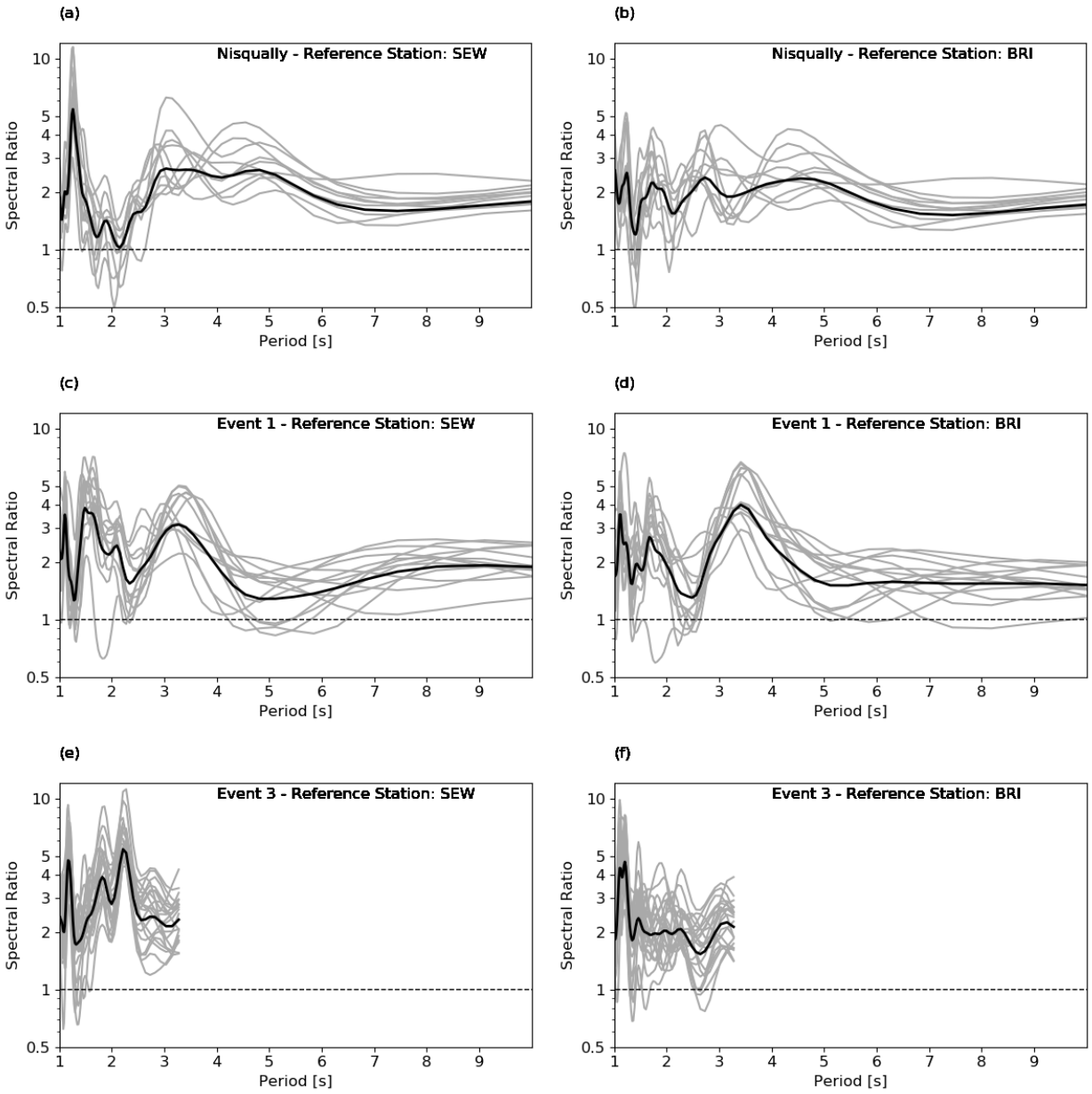

Figure 2.2: Spectral ratios computed from observed waveforms within the Seattle basin relative to reference station SEW (left-hand column) and BRI (right-hand column) for **(a,b)** the Nisqually earthquake, **(c,d)** event 1, and **(e,f)** event 3. Dark lines are the geometric average of all spectral ratios. Lighter-shade lines are spectral ratios from individual stations.

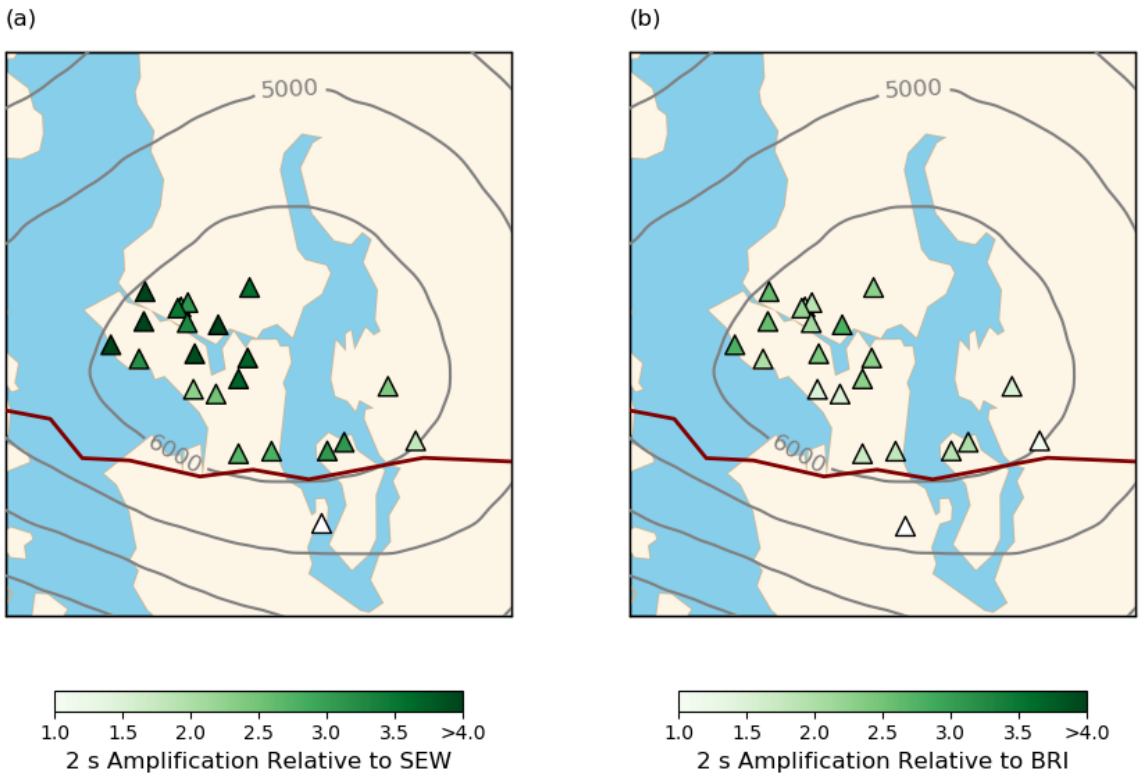

Figure 2.3: Maps showing observed 2 s amplification factors relative to **(a)** SEW and **(b)** BRI for event 3. Stations are represented by triangles. Thin contour lines represent the depth to V_S = 2500 m/s (depth to bedrock in meters) retrieved from the CVM to show the approximate depth of the Seattle basin beneath the sites. The thick line is the location of the SFZ, courtesy of Richard Blakely. White triangles south of the SFZ are reference stations.

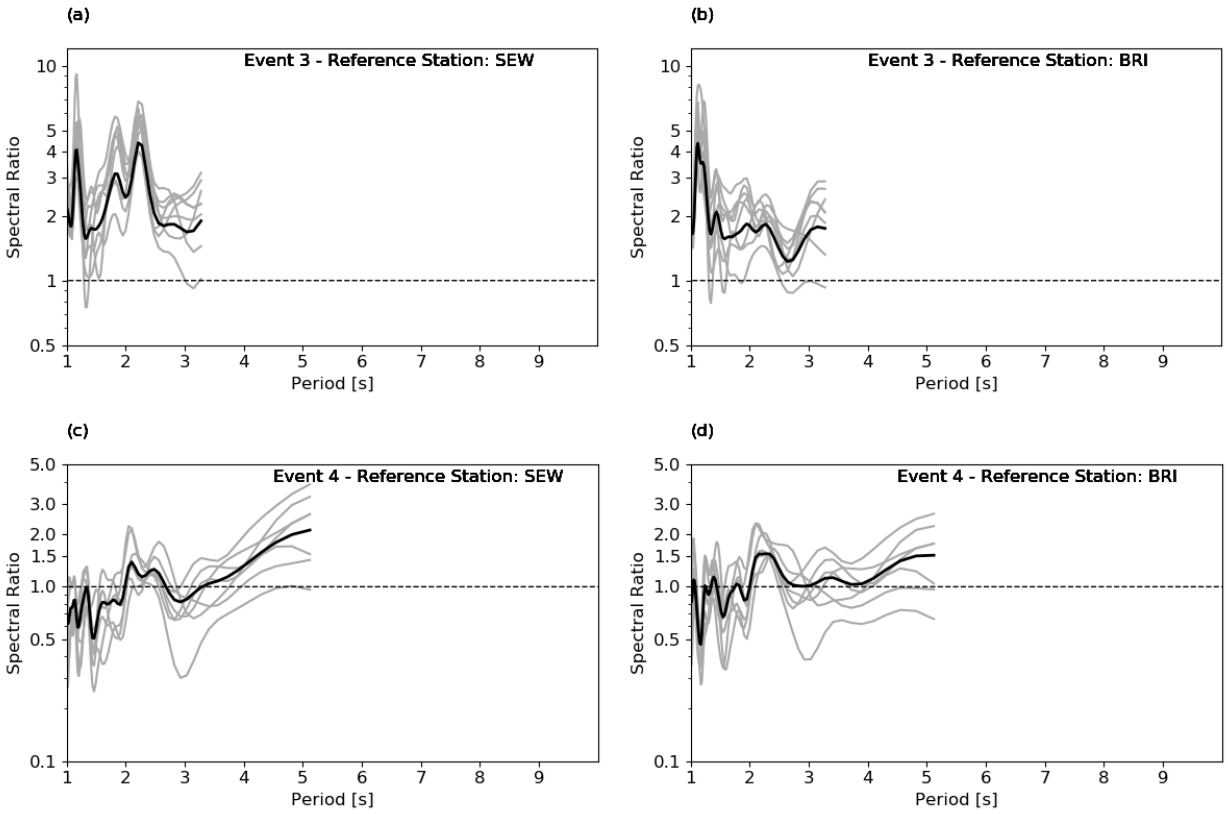

Figure 2.4: Spectral ratios computed from observed waveforms within the Tacoma basin relative to reference station SEW and BRI for **(a,b)** event 3 and **(c,d)** event 4. Dark lines are the geometric average of all spectral ratios. Lighter-shade lines are spectral ratios from individual stations.

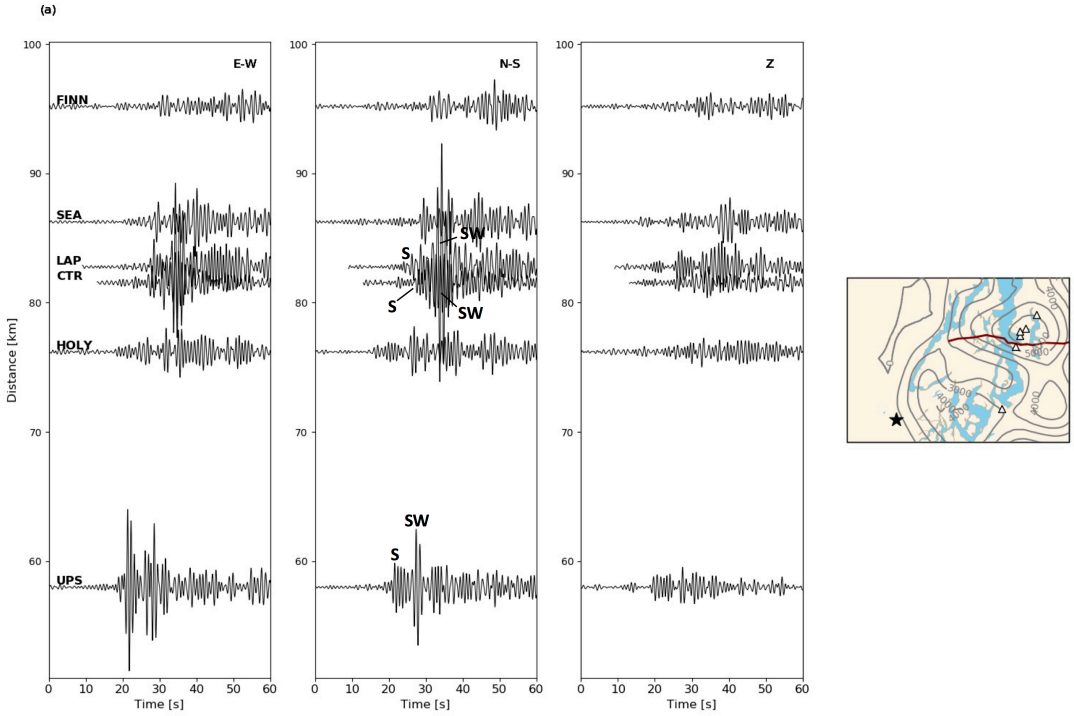
(a)
E-W
N-S
Z
FINN
SEA
LAP
CTR
HOLY
UPS
S
SW
Distance [km]
Time [s]

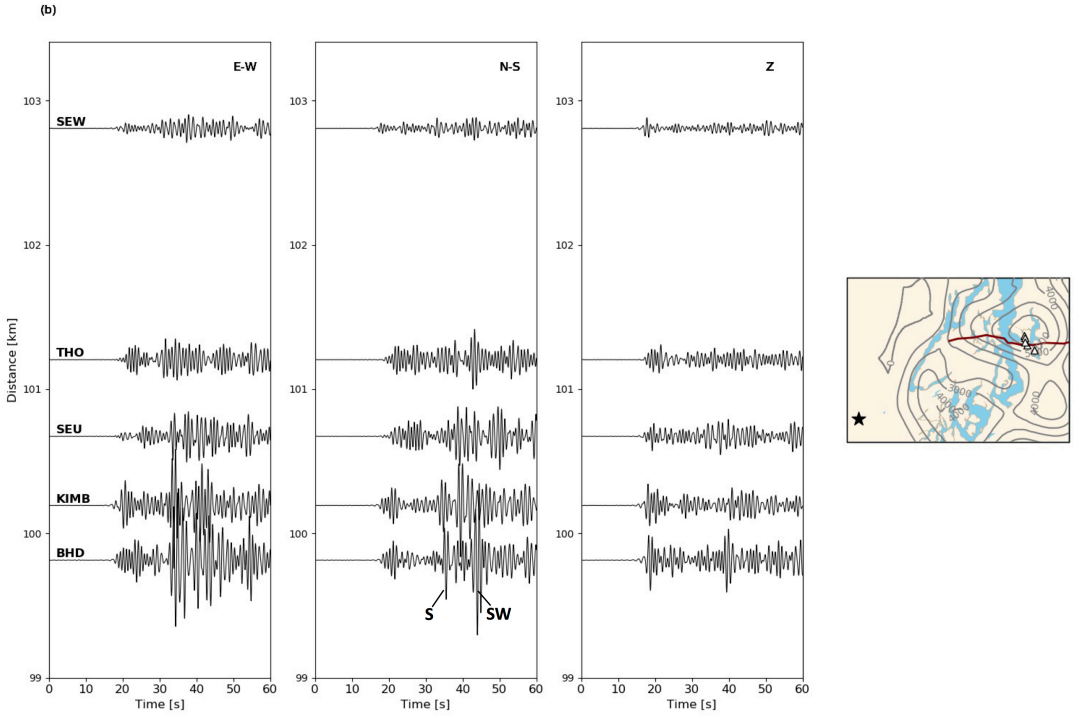
(b)
E-W
N-S
Z
SEW
THO
SEU
KIMB
BHD
S
SW
Distance [km]
Time [s]

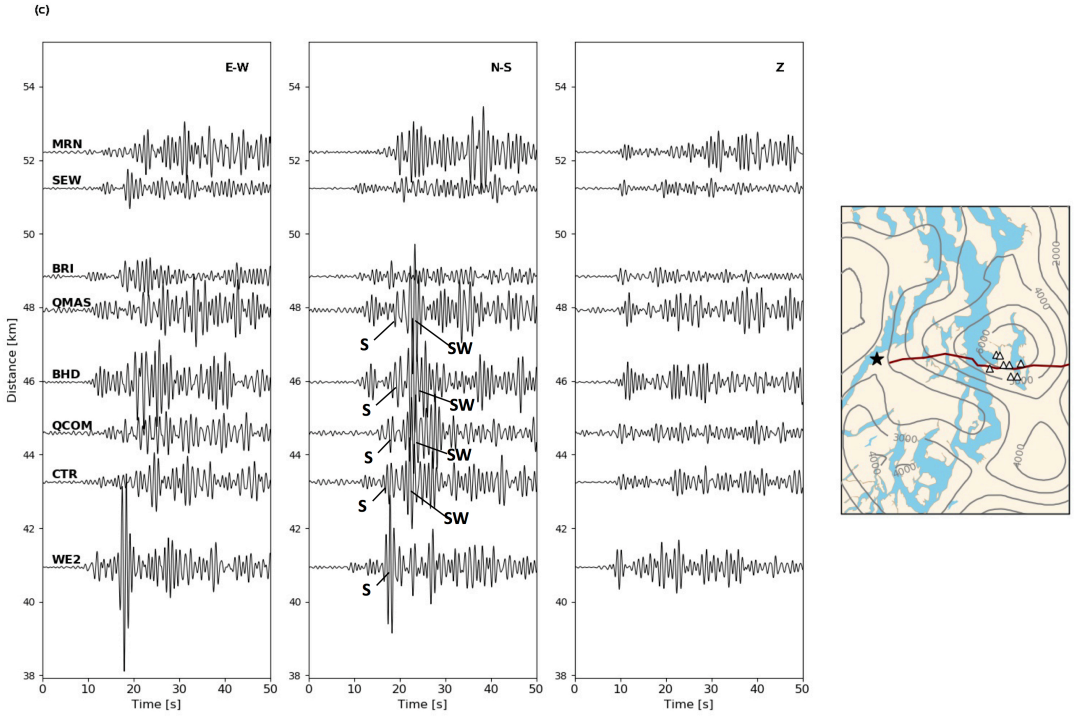

Figure 2.5: Record sections of observations from **(a)** event 2, **(b)** event 1, and **(c)** event 3**.** Velocity (m/s) seismograms are bandpass filtered 0.67-1.33 Hz. *S*-waves and basin-edge surface waves are labeled on the N-S component waveforms as "S" and "SW", respectively. Maps show the locations of the earthquake epicenters (star) and stations (triangles) plotted in record sections. Thin contour lines represent the depth to $V_S = 2500$ m/s (depth to bedrock in meters) retrieved from the CVM to show the approximate depth of the Seattle and Tacoma basins beneath the sites. The thick line is the location of the SFZ, courtesy of Richard Blakely.

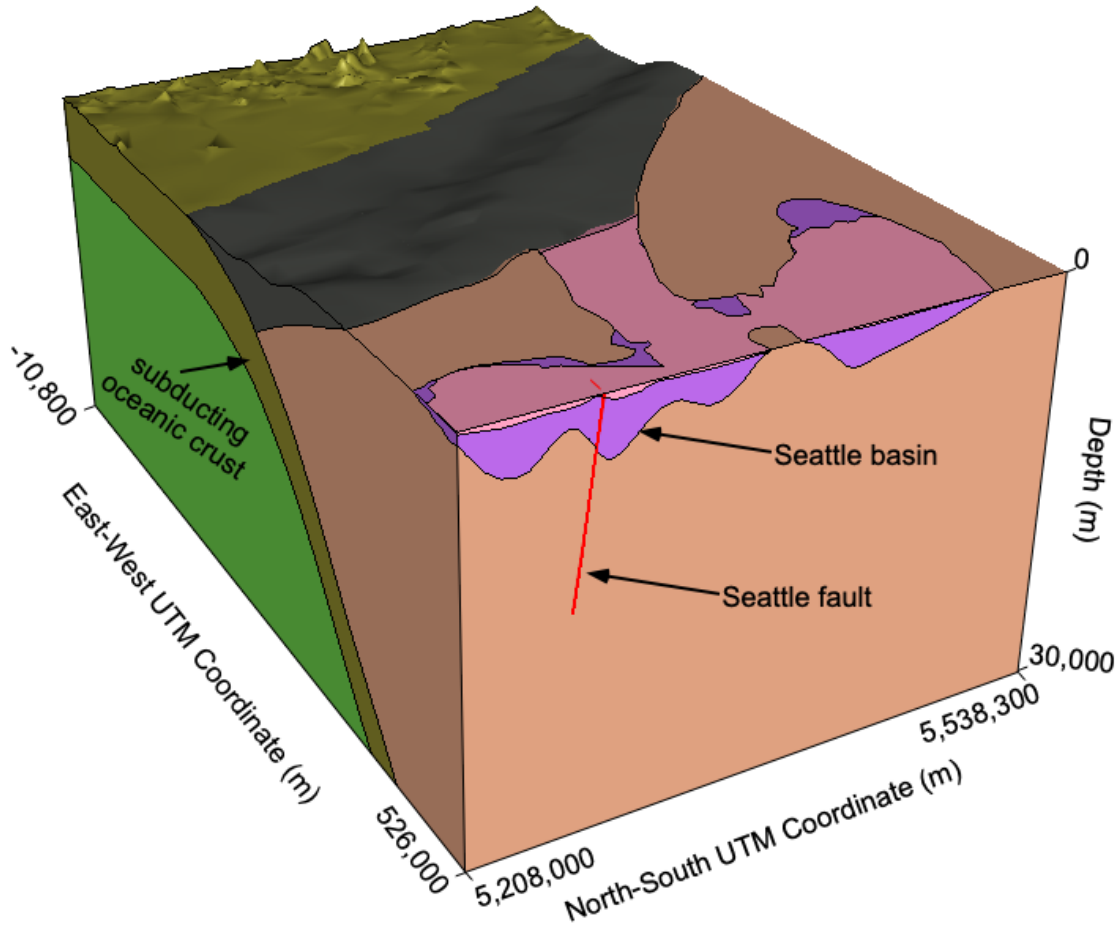

Figure 2.6: Cross-section of the CVM zoomed-in on the Puget Lowland. Vertical exaggeration is approximately 6×. The Quaternary unit within the model is shown in pink. Tertiary sediments are purple, continental crust is tan, oceanic sediments are gray, oceanic crust is olive, and oceanic mantle is green. Axes are annotated in Universal Transverse Mercator (UTM) zone 10 north coordinates. Reprinted with permission from Stephenson *et al.* (2017).

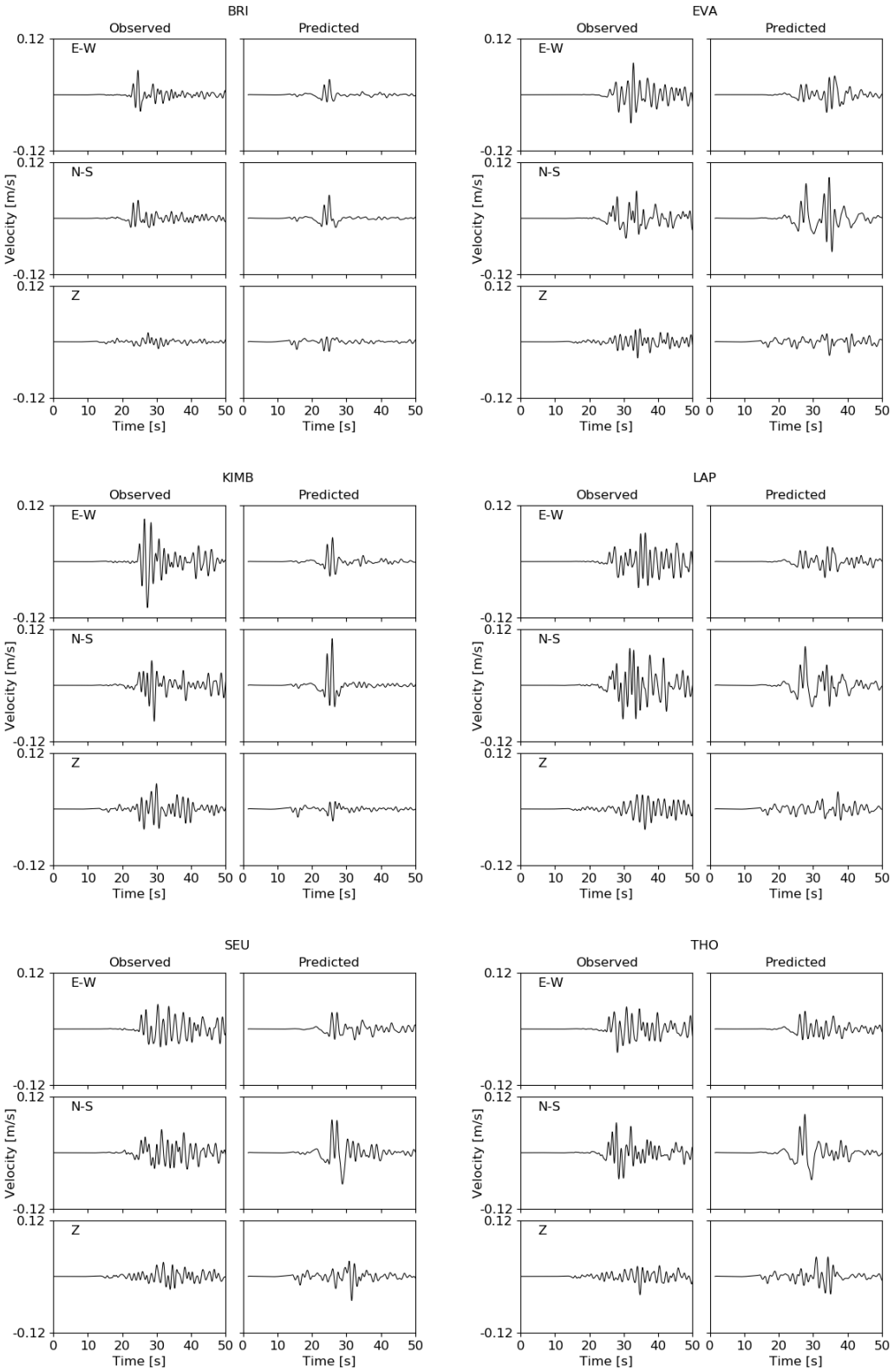

Figure 2.7: Example observed and predicted waveforms from the Nisqually earthquake filtered between 0.1 and 1 Hz.

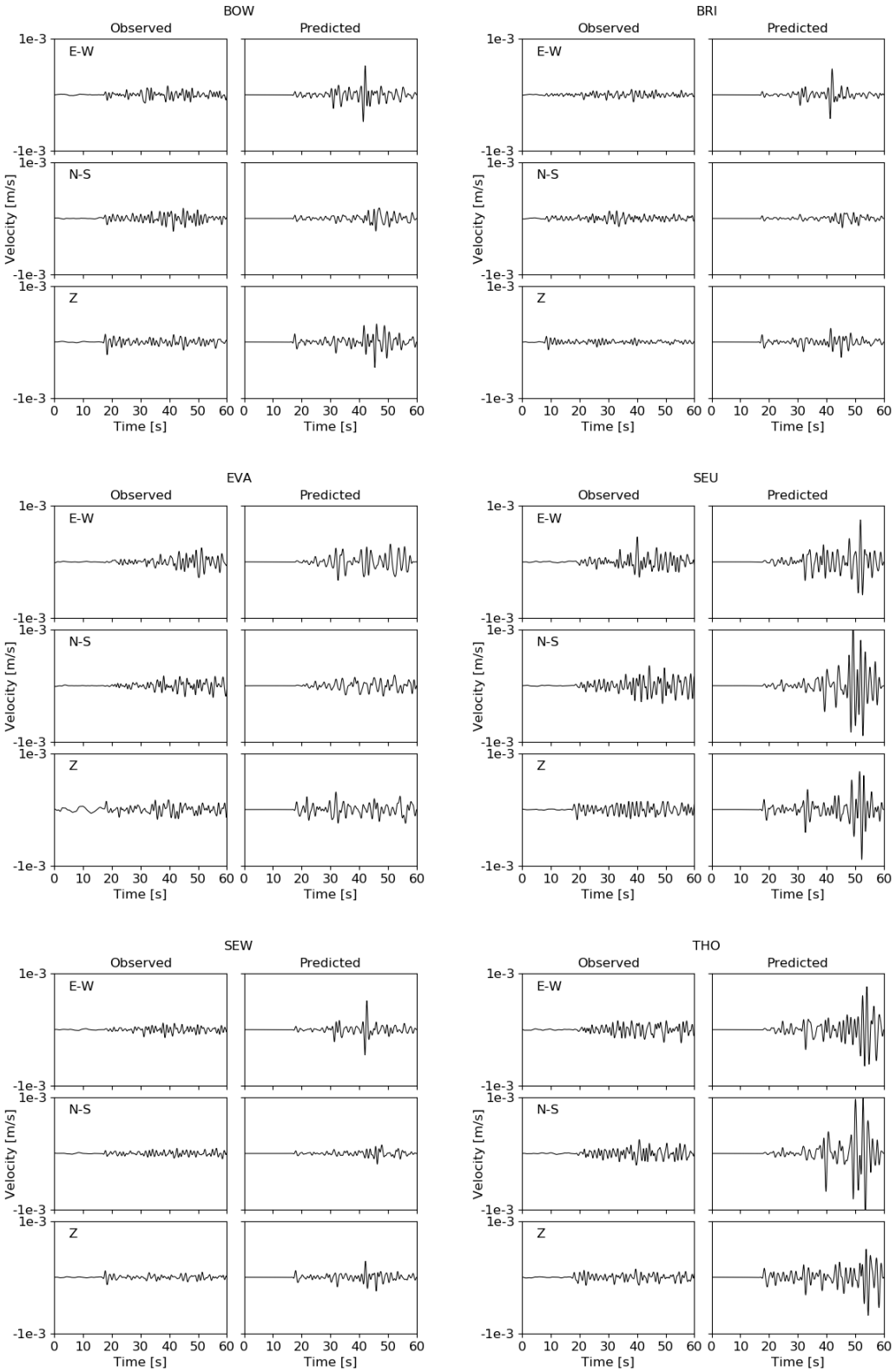

Figure 2.8: Example observed and predicted waveforms from event 1 filtered between 0.1 and 1 Hz.

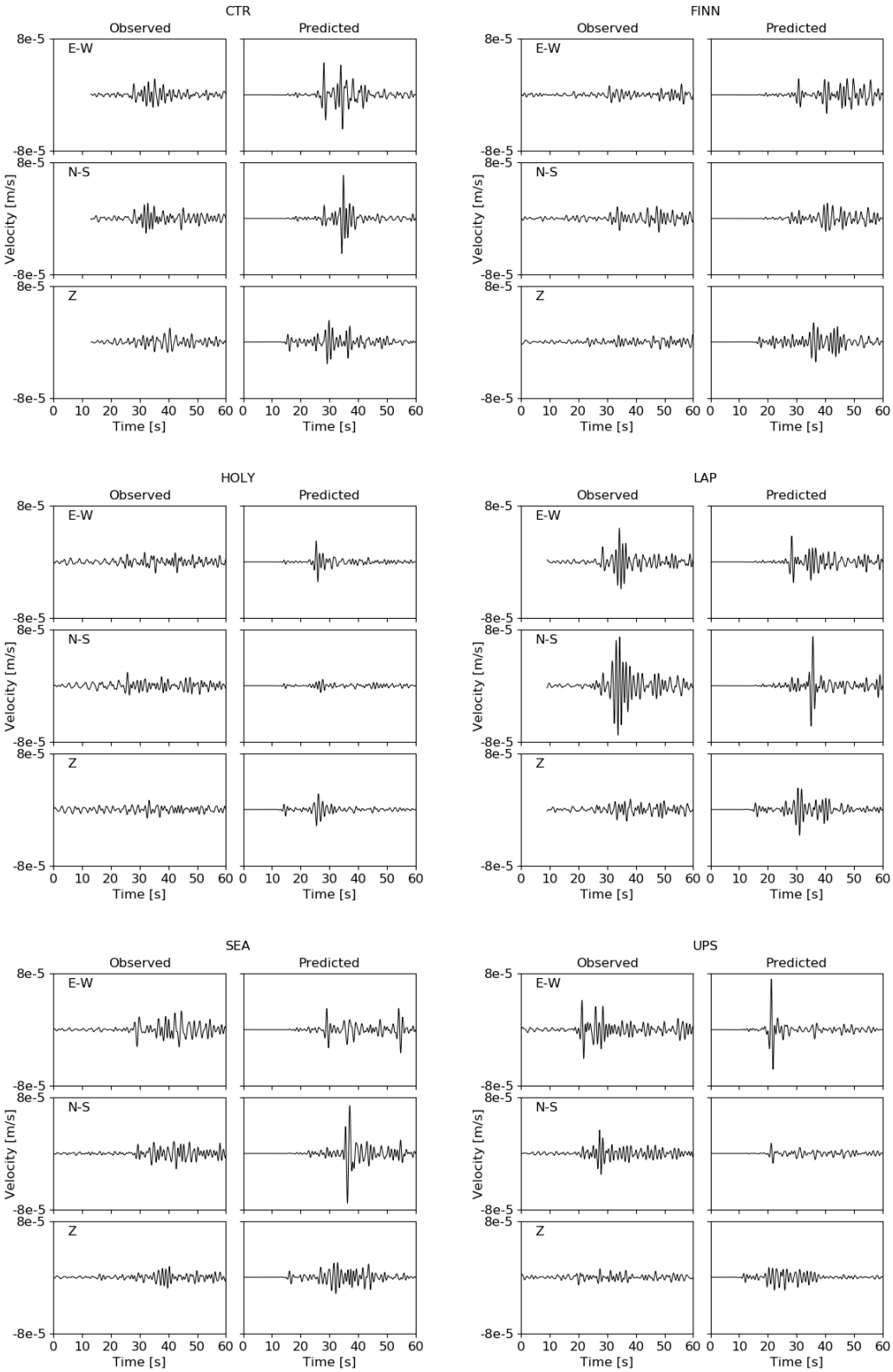

Figure 2.9: Example observed and predicted waveforms from event 2 filtered between 0.3 and 1 Hz.

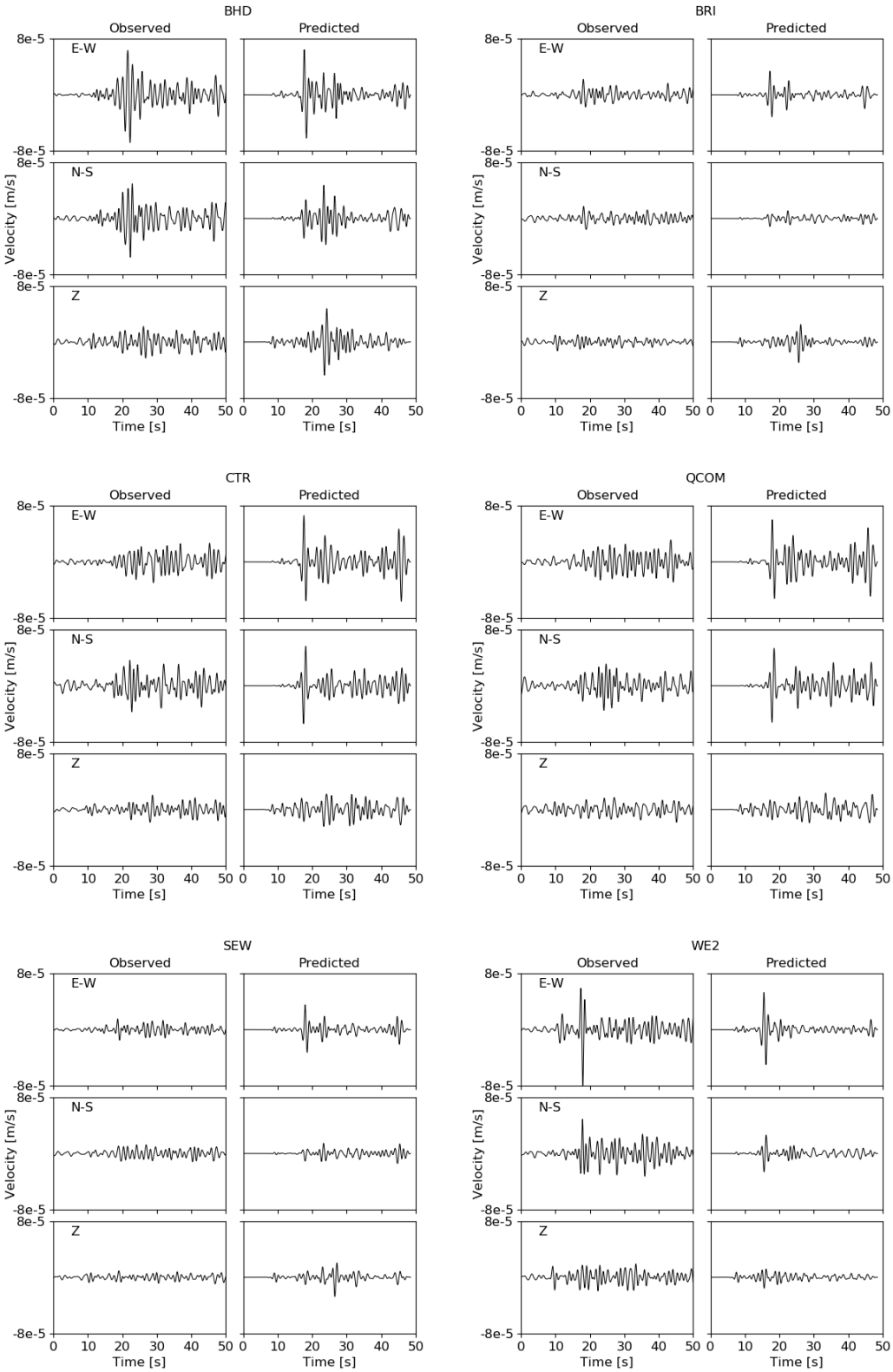

Figure 2.10: Example observed and predicted waveforms from event 3 filtered between 0.3 and 1 Hz.

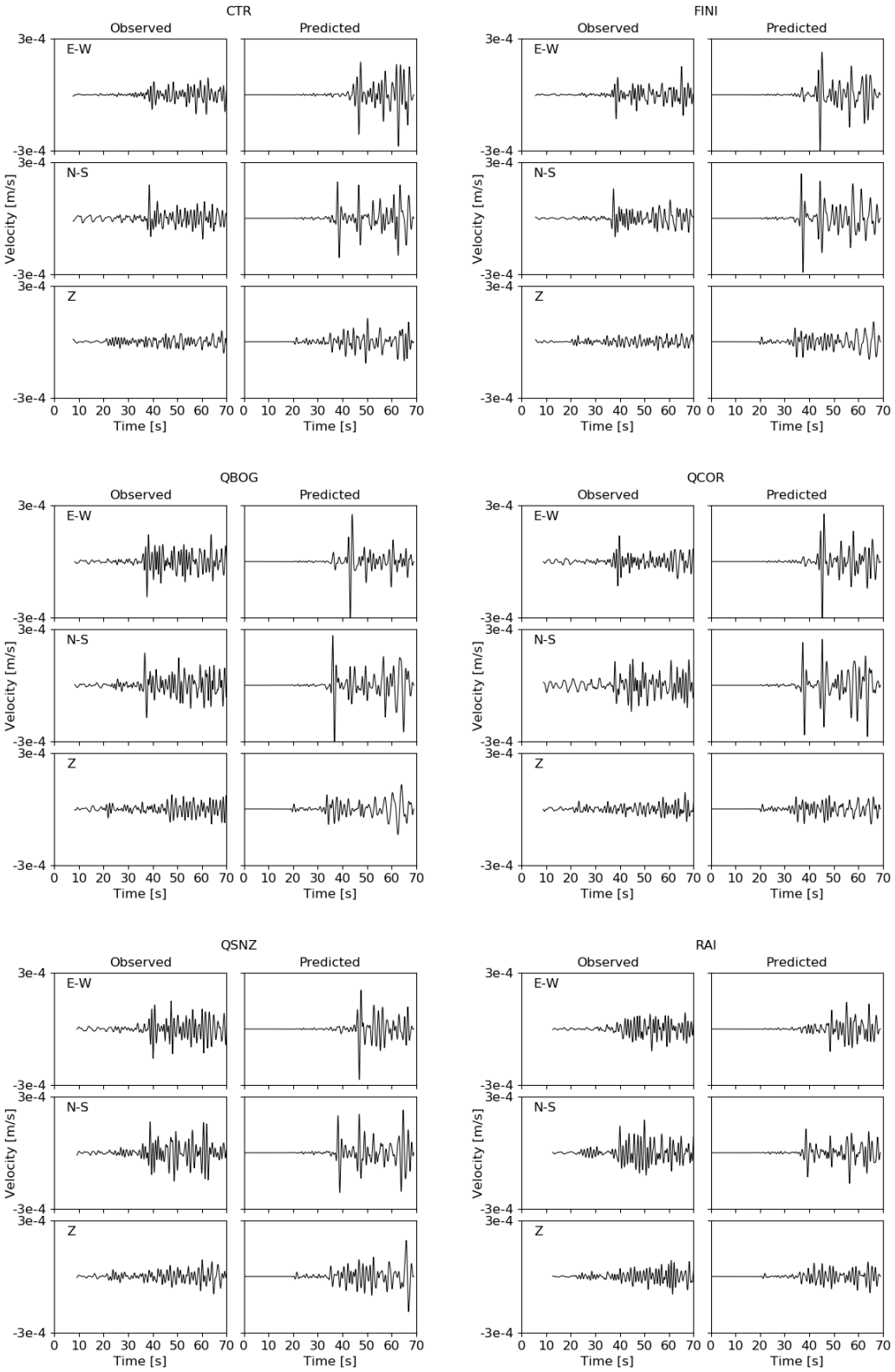

Figure 2.11: Example observed and predicted waveforms from event 4 filtered between 0.2 and 1 Hz.

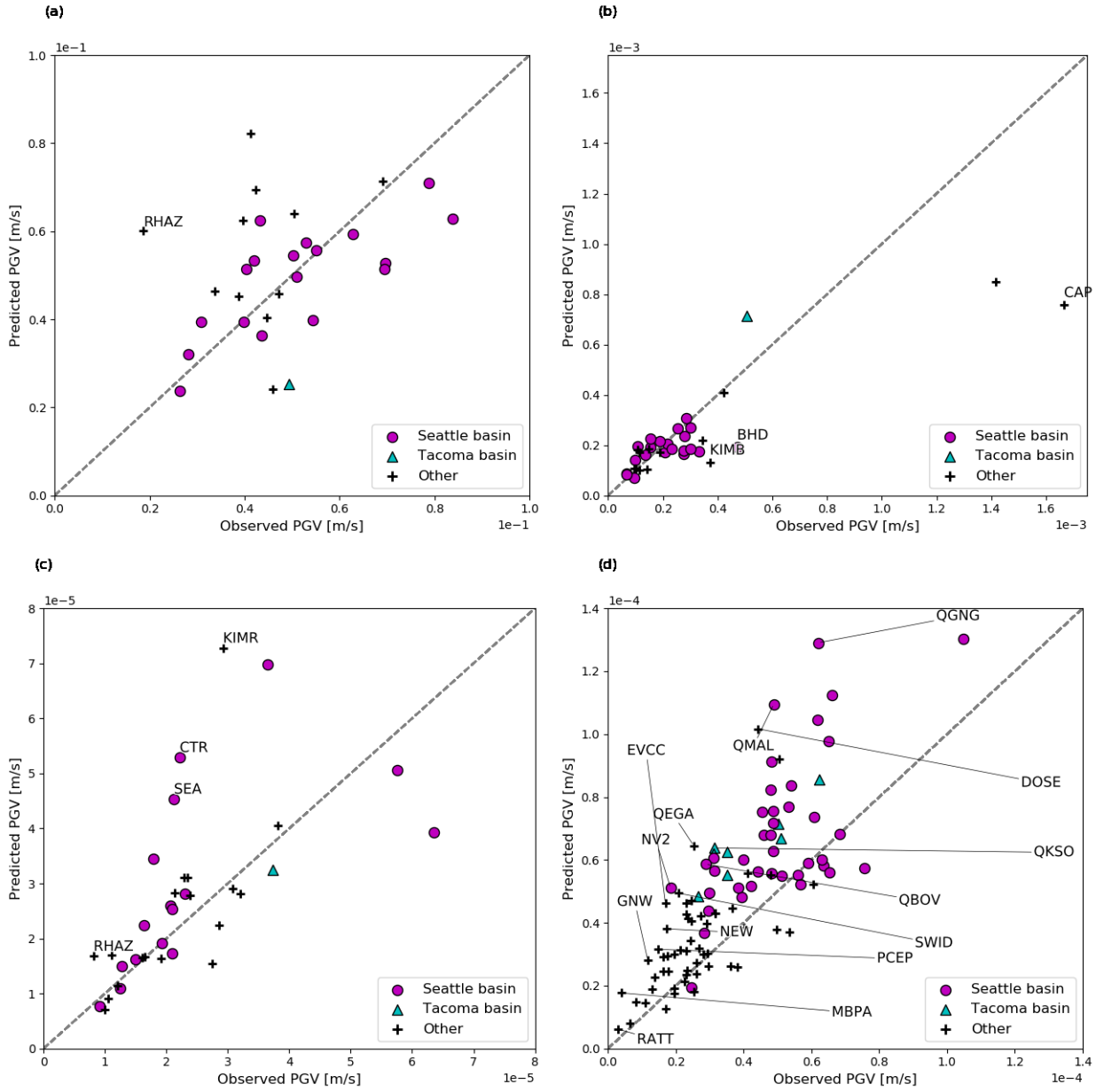
(a)
1e−1
Predicted PGV [m/s]
Observed PGV [m/s]
1e−1
RHAZ
Seattle basin
Tacoma basin
Other
(b)
1e−3
Predicted PGV [m/s]
Observed PGV [m/s]
1e−3
CAP
BHD
KIMB
Seattle basin
Tacoma basin
Other
(c)
1e−5
Predicted PGV [m/s]
Observed PGV [m/s]
1e−5
KIMR
CTR
SEA
RHAZ
Seattle basin
Tacoma basin
Other
(d)
1e−4
Predicted PGV [m/s]
Observed PGV [m/s]
1e−4
QGNG
EVCC
QMAL
DOSE
QEGA
NV2
QKSO
QBOV
GNW
NEW
SWID
PCEP
MBPA
RATT
Seattle basin
Tacoma basin
Other

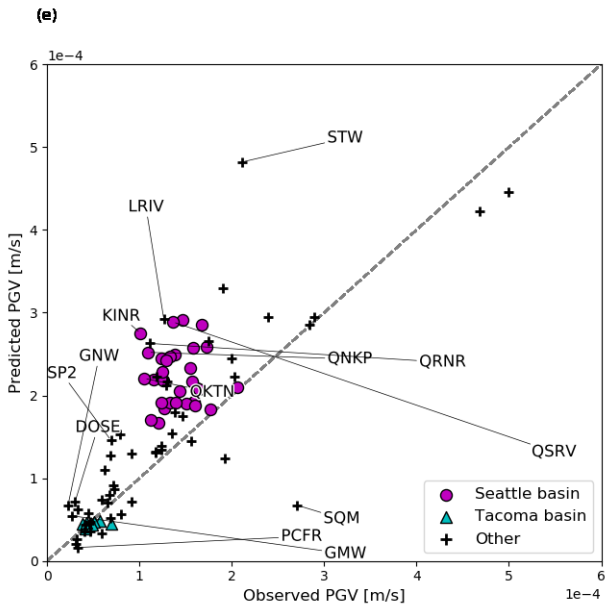

Figure 2.12: Predicted versus observed geometrically averaged horizontal component peak ground velocities (PGVs) for **(a)** Nisqually, **(b)** event 1, **(c)** event 2, **(d)** event 3, and **(e)** event 4. Synthetic PGVs with a misfit larger than a factor of +/- 2 are labeled with station names.

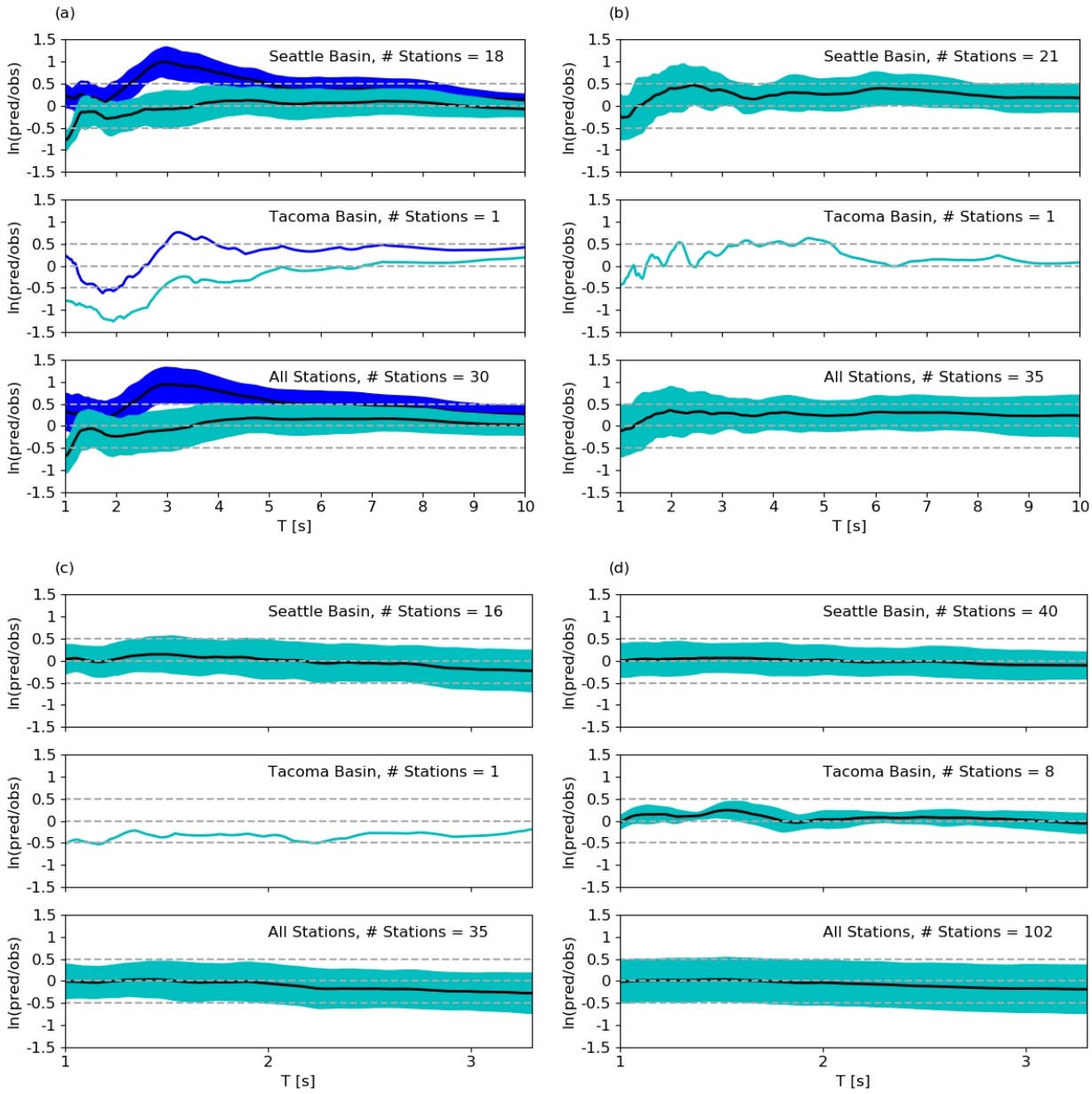
(a)
Seattle Basin, # Stations = 18
Tacoma Basin, # Stations = 1
All Stations, # Stations = 30
(b)
Seattle Basin, # Stations = 21
Tacoma Basin, # Stations = 1
All Stations, # Stations = 35
(c)
Seattle Basin, # Stations = 16
Tacoma Basin, # Stations = 1
All Stations, # Stations = 35
(d)
Seattle Basin, # Stations = 40
Tacoma Basin, # Stations = 8
All Stations, # Stations = 102
ln(pred/obs)
T [s]

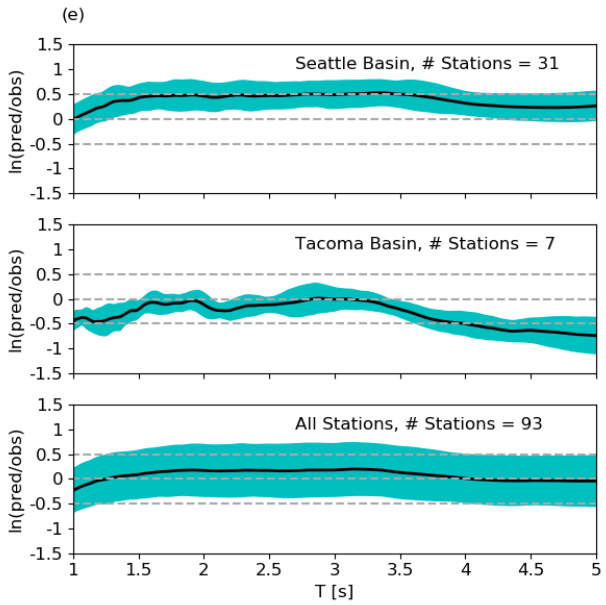

Figure 2.13: Natural log bias plots comparing observed and synthetic response spectra for the **(a)** Nisqually earthquake, **(b)** event 1, **(c)** event 2, **(d)** event 3, and **(e)** event 4. The black solid lines are the natural log bias for Seattle Basin sites (top plots), Tacoma Basin sites (middle plots), and all Puget Lowland sites including basins (bottom plots). Shaded regions represent standard deviation. The lighter-shade solid lines in the subplots representing Tacoma Basin sites in panels (a-c) show the bias between the observed and synthetic response spectra at station UPS. Panel (a) is a comparison of response spectra from two Nisqually simulations with different sources. The lighter shade represents standard deviation between predicted response spectra using the two-point source and observed response spectra. The darker shade represents the standard deviation between predicted response from Nisqually synthetics produced with a single point source and observed response spectra. Dashed lines represent -0.5, 0, and +0.5 natural log bias.

11 SUPPLEMENTARY MATERIALS

Table S2.1: Nisqually earthquake amplification factors								
Seattle basin								
	1 s		**2 s**		**3 s**		**5 s**	
Station	**BRI**	**SEW**	**BRI**	**SEW**	**BRI**	**SEW**	**BRI**	**SEW**
ALO	1.7	2.1	2.1	1.5	2.6	2.8	2.5	2.8
BHD	2.0	2.5	2.8	2.0	2.3	2.4	1.6	1.8
EVA	1.3	1.6	2.1	1.5	1.9	2.0	1.9	2.1
HAL	2.1	2.6	1.9	1.4	2.4	2.5	2.1	2.4
HIG	1.6	2.0	1.6	1.1	1.7	1.8	2.0	2.2
LAP	2.3	2.9	2.3	1.7	3.2	3.4	2.6	2.9
LAWT	1.9	2.3	2.4	1.7	2.1	2.2	1.9	2.1
SEU	1.3	1.6	2.6	1.8	2.7	2.9	2.0	2.3
THO	1.5	1.8	1.5	1.1	2.1	2.3	2.2	2.5
WISC	1.4	1.7	2.1	1.5	2.2	2.4	2.0	2.2
Average	1.7	2.1	2.1	1.5	2.3	2.5	2.1	2.3
Median	1.7	2.1	2.1	1.5	2.3	2.4	2.0	2.3
Tacoma basin								
	1 s		**2 s**		**3 s**		**5 s**	
Station	**BRI**	**SEW**	**BRI**	**SEW**	**BRI**	**SEW**	**BRI**	**SEW**
UPS	0.2	0.3	0.5	0.4	0.5	0.5	0.4	0.5

Table S2.2: Event 1 amplification factors								
Seattle basin								
	1 s		**2 s**		**3 s**		**5 s**	
Station	**BRI**	**SEW**	**BRI**	**SEW**	**BRI**	**SEW**	**BRI**	**SEW**
ALO	1.8	1.9	2.2	2.9	2.8	2.6	2.7	2.4
BHD	3.6	3.7	2.7	3.5	2.3	2.2	1.7	1.5
C43	2.1	2.2	2.1	2.7	3.4	3.2	2.8	2.5
CRO	2.2	2.3	1.9	2.5	2.5	2.4	2.3	2.1
CTR	1.5	1.5	2.0	2.5	2.4	2.2	1.8	1.6
EVA	1.2	1.2	0.9	1.2	1.6	1.5	1.5	1.3
GAR	2.5	2.6	2.1	2.8	2.8	2.6	2.4	2.2
HAL	1.8	1.9	2.1	2.7	2.5	2.4	1.8	1.6
HIG	1.8	1.9	1.7	2.2	2.3	2.1	2.0	1.8
LAP	2.3	2.4	2.7	3.5	2.8	2.7	2.1	1.8
LAWT	1.9	2.0	2.0	2.5	1.9	1.8	1.8	1.6
SEU	2.1	2.2	2.7	3.5	2.6	2.4	2.2	1.9
THO	1.8	1.9	1.8	2.3	2.5	2.4	2.4	2.2
Average	2.0	2.1	2.1	2.7	2.5	2.3	2.1	1.9
Median	1.9	2.0	2.1	2.7	2.5	2.4	2.1	1.8
Tacoma basin								
	1 s		**2 s**		**3 s**		**5 s**	
Station	**BRI**	**SEW**	**BRI**	**SEW**	**BRI**	**SEW**	**BRI**	**SEW**
UPS	3.6	3.8	2.4	3.1	2.4	3.1	3.3	2.9

Table S2.3: Event 2 amplification factors								
Seattle basin								
	1 s		**2 s**		**3 s**		**5 s**	
Station	**BRI**	**SEW**	**BRI**	**SEW**	**BRI**	**SEW**	**BRI**	**SEW**
BHD		2.6		2.7				
CTR		1.6		1.6				
LAP		3.0		1.7				
MER		1.6		1.7				
MRN		1.8		1.9				
NV2		1.4		1.3				
RAI		1.6		1.7				
SEA		1.6		2.1				
Average		1.9		1.8				
Median		1.6		1.7				
Tacoma basin								
	1 s		**2 s**		**3 s**		**5 s**	
Station	**BRI**	**SEW**	**BRI**	**SEW**	**BRI**	**SEW**	**BRI**	**SEW**
UPS		1.7		1.0				

Table S2.4: Event 3 amplification factors

Seattle basin								
	1 s		2 s		3 s		5 s	
Station	**BRI**	**SEW**	**BRI**	**SEW**	**BRI**	**SEW**	**BRI**	**SEW**
BHD	2.6	2.5	1.7	2.7				
CIN	2.1	2.0	1.8	2.9				
CTR	1.8	1.7	1.5	2.3				
FINI	2.2	2.1	1.9	3.1				
LAU	2.5	2.4	2.2	3.5				
LAWT	3.2	3.1	2.6	4.1				
MRN	2.4	2.3	2.0	3.1				
NOB	2.7	2.6	2.4	3.9				
NV2	1.5	1.4	1.1	1.8				
QADA	3.0	2.9	2.6	4.2				
QBOV	1.4	1.4	1.5	2.4				
QCOM	1.7	1.6	1.5	2.5				
QCOR	2.4	2.3	2.8	4.5				
QEMI	3.7	3.5	2.3	3.7				
QMAL	2.1	2.0	2.3	3.6				
QMAS	2.7	2.5	1.8	2.8				
QMIN	2.3	2.2	1.9	3.1				
QNWT	2.9	2.8	2.0	3.2				
QPAL	2.2	2.1	2.1	3.3				
QPRK	3.1	2.9	2.8	4.4				
QSNZ	2.8	2.7	2.3	3.7				
Average	2.4	2.3	2.1	3.3				
Median	2.4	2.3	2.0	3.2				
Tacoma basin								
	1 s		2 s		3 s		5 s	
Station	**BRI**	**SEW**	**BRI**	**SEW**	**BRI**	**SEW**	**BRI**	**SEW**
MAC	2.9	2.7	2.1	3.3				
QCMM	2.4	2.3	2.3	3.6				
QKSO	2.0	1.9	1.5	2.4				
QSKT	2.3	2.2	2.0	3.1				
QTKM	1.9	1.8	1.5	2.4				
QTNB	2.8	2.6	1.9	3.0				
UPL	2.3	2.2	1.9	3.0				
UPS	2.3	2.2	1.1	1.8				
Average	2.4	2.2	1.8	2.8				
Median	2.3	2.2	1.9	3.0				

Table S2.5: Event 4 amplification factors

Seattle basin								
	1 s		2 s		3 s		5 s	
Station	**BRI**	**SEW**	**BRI**	**SEW**	**BRI**	**SEW**	**BRI**	**SEW**
CIN	1.2	1.1	1.7	1.5	1.6	1.6		
CTR	1.3	1.2	1.4	1.2	1.4	1.4		
FINI	1.0	1.0	1.3	1.2	1.5	1.5		
LAU	1.5	1.3	1.7	1.5	1.7	1.6		
MRN	2.0	1.9	2.4	2.1	2.0	1.9		
NV2	1.3	1.2	2.3	2.1	2.1	2.1		
QCOR	1.4	1.3	1.6	1.4	2.1	2.1		
QEMI	2.0	1.8	1.6	1.4	1.4	1.4		
QMAL	1.7	1.5	2.2	2.0	1.4	1.4		
QMIN	1.9	1.8	2.1	1.8	1.9	1.9		
QNWT	1.8	1.6	1.9	1.7	1.4	1.4		
QPRK	1.8	1.7	1.9	1.7	1.6	1.6		
QSNZ	1.8	1.6	2.1	1.9	1.4	1.4		
RAI	1.7	1.6	1.7	1.5	1.5	1.5		
Average	1.6	1.5	1.9	1.6	1.6	1.6		
Median	1.7	1.6	1.8	1.6	1.6	1.6		
Tacoma basin								
	1 s		2 s		3 s		5 s	
Station	**BRI**	**SEW**	**BRI**	**SEW**	**BRI**	**SEW**	**BRI**	**SEW**
MAC	1.0	0.9	1.2	1.1	1.1	1.0		
QCMM	0.8	0.8	1.3	1.1	1.2	1.2		
QKSO	0.6	0.5	0.9	0.8	1.1	1.1		
QSKT	0.6	0.6	1.0	0.9	1.4	1.4		
QTKM	0.7	0.6	0.8	0.7	1.1	1.1		
UPL	0.9	0.8	1.2	1.0	1.0	1.0		
UPS	0.6	0.6	0.7	0.6	0.6	0.6		
Average	0.7	0.7	1.0	0.9	1.1	1.1		
Median	0.7	0.6	1.0	0.9	1.1	1.1		

12 DATA AND RESOURCES

All data from the PNSN and the USGS Seattle Urban Seismic Array are available from the IRIS Data Management Center (www.iris.edu, last accessed August 2018). Earthquake source information is available from the PNSN at www.pnsn.org (last accessed August 2018). All observed and synthetic waveform files analyzed in this article are available at https://doi-org.offcampus.lib.washington.edu/10.1785/0120190211.

13 ACKNOWLEDGEMENTS

This work was supported by National Science Foundation Grant Number EAR-1331412. The authors thank Nasser Marafi for providing scripts to compute response spectra. We also thank Benjamin Baker, Paul Bodin, Robert Graves, Sheri Molnar, Thomas Pratt, and an anonymous reviewer for helpful comments that improved this manuscript.

14 REFERENCES

Abrahamson, N. A., P. G. Somerville, and C. A. Cornell (1990). Uncertainty in numerical strong motion predictions, *Proc. of the Fourth U. S. Nat. Conf. Earthq. Eng.* Vol. 1, 407–416.

Atkinson, G. M. (1995). Attenuation and source parameters of earthquakes in the Cascadia region, *Bull. Seism. Soc. Am.* **85**, 1327–1342.

Barberopoulou, A., A. Qamar, T. L. Pratt, K. C. Creager, and W. P. Steele (2004). Local amplification of seismic waves from the Denali Earthquake and damaging seiches in Lake Union, Seattle, Washington, *Geophys. Res. Lett.* **31**, doi: 10.1029/2003GL018569.

Barberopoulou, A., A. Qamar, T. L. Pratt, and W. P. Steele (2006). Long-period effects of the Denali earthquake on water bodies in the Puget Lowland: Observations and modeling, *Bull. Seism. Soc. Am.* **96**, 519–535, doi: 10.1785/0120050090.

Blair, J. L., P. A. McCrory, D. H. Oppenheimer, and F. Waldhauser (2013). A Geo-referenced 3D model of the Juan de Fuca Slab and associated seismicity, *U.S. Geol. Surv. Data Series 633,* Version 1.2, available at http://pubs.er.usgs.gov/publication/ds633 (last accessed May 2019).

Blakely, R. J., R. E. Wells, C. S. Weaver, and S. Y. Johnson (2002). Location, structure, and seismicity of the Seattle fault zone, Washington: Evidence from aeromagnetic anomalies, geologic mapping, and seismic-reflection data, *Geol. Soc. Am. Bull.* **114**, 169–177.

Booth, D. B., R. E. Wells, and R. W. Givler (2004). Chimney damage in the greater Seattle area from the Nisqually earthquake 28 February 2001, *Bull. Seism. Soc. Am.* **94**, 1143–1158.

Brocher, T. M., R. J. Blakely, and R. E. Wells (2004). Interpretation of the Seattle uplift, Washington, as a passive-roof duplex, *Bull. Seismol. Soc. Am*. **94**, 1379–1401, doi: 10.1785/012003190.

Brocher, T. M., T. Parsons, R. J. Blakely, N. I. Christensen, M. A. Fisher, and R. E. Wells (2001). Upper crustal structure in Puget Lowland, Washington: Results from the 1998 Seismic Hazards Investigation in Puget Sound, *J. Geophys. Res.: Solid Earth* **106**, 13541–13564.

Frankel, A., W. Stephenson, and D. Carver (2009). Sedimentary basin effects in Seattle, Washington: Ground-motion observations and 3D simulations, *Bull. Seism. Soc. Am.* **99**, 1579–1611.

Frankel, A., W. Stephenson, D. Carver, J. Odum, R. Williams, and S. Rhea (2011). Probabilistic seismic hazard maps for Seattle: 3D sedimentary basin effects, nonlinear site response, and uncertainties from random velocity variations, IASPEI/IAEE International

symposium, Effects of Surface Geology on Seismic Motion, University of California, Santa Barbara, California, 12 pp.

Frankel, A., E. Wirth, N. Marafi, J. Vidale, and W. Stephenson (2018). Broadband synthetic seismograms for magnitude 9 earthquakes on the Cascadia megathrust based on 3D simulations and stochastic synthetics, Part 1: Methodology and overall results, *Bull. Seism. Soc. Am.* **108**, 2347–2369.

Frankel, A. D., D. L. Carver, and R. A. Williams (2002). Nonlinear and linear site response and basin effects in Seattle for the M 6.8 Nisqually, Washington, earthquake, *Bull. Seism. Soc. Am.* **92**, 2090–2109.

Frankel, A. D., W. J. Stephenson, D. L. Carver, R. A. Williams, J. K. Odum, and S. Rhea (2007). Seismic hazard maps for Seattle, Washington, incorporating 3D sedimentary basin effects, nonlinear site response, and rupture directivity, *U. S. Geol. Surv. Open-File Rept. 2007-1175,* 77 pp.

Ichinose, G. A., H. K. Thio, and P. G. Somerville (2004). Rupture process and near-source shaking of the 1965 Seattle-Tacoma and 2001 Nisqually, intraslab earthquakes, *Geophys. Res. Lett.* **31**, doi: 10.1029/2004GL019668.

Johnson, S. Y., and S. V. Dadisman, J. R. Childs, and W. D. Stanley (1999). Active tectonics of the Seattle fault and central Puget Sound, Washington— Implications for earthquake hazards, *Geol. Soc. Am. Bull.* **111**, 1042-1053.

Liu, P.-C., and R. J. Archuleta (2002). The effect of a low-velocity surface layer on simulated ground motion, *Seism. Res. Lett.* **73**, 267.

McCrory, P. A., J. L. Blair, F. Waldhauser, and D. H. Oppenheimer (2012). Juan de Fuca slab geometry and its relation to Wadati-Benioff zone seismicity, *J. Geophys. Res.: Solid Earth* **117**, no. B09306, doi: 10.1029/2012JB009407.

Moschetti, M. P., M. H. Ritzwoller and N. M. Shapiro (2007). Surface wave tomography of the western United States from ambient seismic noise: Rayleigh wave group velocity maps, *Geochem., Geophys., Geosys.* **8**, doi: 10.1029/2007GC001655.

Nelson, A. R., S. Y. Johnson, H. M. Kelsey, R. E. Wells, B. L. Sherrod, S. K. Pezzopane, L.-A. Bradley, R. D. Koehler, and R. C. Bucknam (2003). Late Holocene earthquakes on the Toe Jam Hill fault, Seattle fault zone, Bainbridge Island, Washington, *Geo. Soc. Am. Bull.* **115**, 1388, doi: 10.1130/B25262.1.

Odum, J. K., W. J. Stephenson, T. L. Pratt, and R. J. Blakely (2016). Shallow geophysical imaging of the Olympia anomaly: An enigmatic structure in the southern Puget Lowland, Washington State, *Geosphere* **12**, 1617–1632, doi: 10.1130/GES01248.1.

Pratt, T. L., and T. M. Brocher (2006). Site response and attenuation in the Puget Lowland, Washington State, *Bull. Seism. Soc. Am.* **96**, 536–552, doi: 10.1785/0120040200.

Pratt, T. L., T. M. Brocher, C. S. Weaver, K. C. Creager, C. M. Snelson, R. S. Crosson, K. C. Miller, and A. M. Tréhu (2003). Amplification of seismic waves by the Seattle basin, Washington State, *Bull. Seism. Soc. Am.* **93**, 533–545, doi: 10.1785/0120010292.

Pratt, T. L., S. Johnson, C. Potter, W. Stephenson, and C. Finn (1997). Seismic reflection images beneath Puget Sound, western Washington State: The Puget Lowland thrust sheet hypothesis, *J. Geophys. Res.* **102**, 27469–27489.

Schuster, J. E. (2005). Geologic map of Washington State, *WA State Dep. of Nat. Res.*, scale 1:500,000.

Snelson, C. M., T. M. Brocher, K. C. Miller, T. L. Pratt, and A. M.Tréhu (2007). Seismic amplification within the Seattle basin, Washington State: Insights from SHIPS seismic tomography experiments, *Bull. Seism. Soc. Am.* **97**, 1432–1448, doi: 10.1785/0120050204.

Stephenson, W. J. (2007). Velocity and density models incorporating the Cascadia subduction zone for 3D earthquake ground motion simulations, *U. S. Geol. Surv. Open-File Rept. 2007-1348,* 24pp.

Stephenson, W. J., A. D. Frankel, J. K. Odum, R. A. Williams, and T. L. Pratt (2006). Toward resolving an earthquake ground motion mystery in west Seattle, Washington State: Shallow seismic focusing may cause anomalous chimney damage, *Geophys. Res. Lett.* **33**, doi: 10.1029/2005GL025037.

Stephenson, W. J., N. G. Reitman, and S. J. Angster (2017). P- and S-wave velocity models incorporating the Cascadia subduction zone for 3D earthquake ground motion simulations, Update for OFR 2007-1348, *U. S. Geol. Surv. Open-File Rept. 2017-1152*, 17 pp., doi: 10.3133/ofr20171152.

ten Brink, U. S., P. C. Molzer, M. A. Fisher, R. J. Blakely, R. C. Bucknam, T. Parsons, R. S. Crosson, and K. C. Creager (2002). Subsurface geometry and evolution of the Seattle fault zone and the Seattle basin, Washington, *Bull. Seismol. Soc. Am.* **92**, 1737–1753, doi: 10.1785/0120010229.

U.S. Geological Survey (2018). Quaternary fault and fold database for the United States, from USGS website available at http://earthquake.usgs.gov/hazards/qfaults/ (last accessed February 2018).

Williams, R. A., W. J. Stephenson, A. D. Frankel, and J. K. Odum (1999). Surface seismic measurements of near-surface P- and S-wave seismic velocities at earthquake recording stations, Seattle, Washington, *Earthq. Spectra* **15**, 565–584, doi: 10.1193/1.1586059.

Wirth, E. A., A. D. Frankel, N. Marafi, J. E. Vidale, and W. J. Stephenson (2018). Broadband synthetic seismograms for magnitude 9 earthquakes on the Cascadia megathrust based on 3D simulations and stochastic synthetics, Part 2: Rupture parameters and variability, *Bull. Seism. Soc. Am.* **108**, 2370–2388, doi: 10.1785/0120180029.

III Effect of fixing earthquake depth in ShakeAlert algorithms on performance for intraslab earthquakes

The content of this chapter is published in:

Thompson, M., J. R. Hartog, and E. A. Wirth (2022). Effect of fixing earthquake depth in ShakeAlert algorithms on performance for intraslab earthquakes, *Seism. Res. Lett.* **93**, no. 1, 277–287, doi: 10.1785/0220210056.

1 INTRODUCTION

Earthquake early warning (EEW) systems are designed to quickly detect ongoing earthquakes and send alerts to people and automated systems in the path of imminent ground shaking. ShakeAlert is an EEW system for the West Coast of the United States that provides alerts to the general public in California, Oregon, and Washington. It is currently a network-based *P*-wave detection system, which uses the first few seconds of *P*-wave information recorded at stations to estimate the magnitude and location of an ongoing earthquake and predict the intensity of ground shaking at sites where the earthquake is likely to be felt.

A major goal in developing ShakeAlert is to minimize computational cost and processing time between when an earthquake is detected and when an alert is sent out, without compromising accuracy. One way of doing this is to reduce the number of variables that system algorithms are required to calculate. ShakeAlert uses two seismic algorithms to characterize the source parameters of an event: the Earthquake Point-Source Integrated Code (EPIC), based on ElarmS-3 (Chung *et al.*, 2019), and the finite-fault algorithm named Finite-Fault Rupture Detector (FinDer) (Böse *et al.*, 2018). Both algorithms are currently configured to assume that all earthquake types occur at a fixed shallow depth, reducing the search for the source location from

a 3D to a 2D problem. This is a reasonable assumption in most of California where earthquakes typically occur on shallow crustal faults at depths of 5–15 km (Brown *et al.*, 2011).

The Pacific Northwest (PNW) region north of Cape Mendocino, California, however, is a more complex tectonic environment. It is located along the Cascadia subduction zone, formed by the Juan de Fuca plate subducting beneath the North American plate, which extends beneath northern California, Oregon, and Washington in the United States, and southwestern British Columbia, Canada (**Fig. 3.1a**). Along with crustal earthquakes, deep intraslab and large megathrust events pose a significant hazard to the region. The most frequently recurring type of moderate-magnitude earthquakes are intraslab events in northwestern Washington, such as the 2001 M_w 6.8 Nisqually earthquake, which generally occur at depths between 35–65 km (Petersen *et al.*, 2014).

To date, there are no studies that examine how the simplifying assumption of a fixed shallow depth affects the accuracy and timeliness of EEW algorithms in the PNW. The most thorough study of algorithms' potential to provide accurate and timely warnings in subduction zone settings is described in Meier *et al.* (2020), which replayed 219 Japanese crustal and subduction zone earthquakes through the EPIC, FinDer, and the Propagation of Local Undamped Motion (PLUM) algorithms (Kodera *et al.*, 2018). Meier *et al.* (2020) modified EPIC to search over a range of possible earthquake depths (2, 8, 20, 26, 30, 36, and 42 km), while FinDer used either generic symmetrical templates calculated assuming an earthquake depth of 10 km or, for offshore events, asymmetrical templates calculated assuming an earthquake depth of 20 km. PLUM is a ground-motion based algorithm that does not characterize an earthquake source. The authors assessed the performance of each algorithm by classifying individual seismic stations used in the study based on whether, for a particular alert threshold, an alert was correctly issued

(or not issued) to a site and how much warning time alerted sites received. Sites were then analyzed to determine how often and under what circumstances each algorithm provided accurate alerts with useful warning times. The effect of depth estimate accuracy on alert performance was not considered. Their analysis demonstrated that all three algorithms had the potential to provide more timely accurate alerts in a subduction zone setting than a shallow crustal earthquake environment, particularly for severe to extreme ground motions, due to the greater hypocentral distance of noncrustal events (i.e., subduction zone interface, outer rise, and intraslab events) compared to onshore crustal earthquakes. For example, 25% of sites with observed peak shaking intensities between Japanese Meteorological Agency (JMA) Intensity 6–7 (equivalent to modified Mercalli intensity 8.9–10.5) could expect warning times of 40 seconds from the EPIC algorithm during a noncrustal earthquake, but the longest warning time one could expect for a shallow crustal event was ~15 seconds. Their warning times did not take into consideration delays from data telemetry or alert delivery.

We attempt to quantify the impact of (incorrectly) assuming intraslab earthquakes in the PNW occur at a fixed shallow depth of 8 km. Using an empirical approach, we measure improvements in earthquake source estimates (i.e., location, magnitude), ground-motion predictions, and warning times when the true depth is known, to determine whether it is advisable to try to constrain the depth of an earthquake using early warning algorithms. We note that constraining earthquake depths can be a challenge even when using conventional seismic location methods with a lot of data (e.g., Gomberg *et al.*, 1990; Lomax *et al.*, 2009). Thus, trying to constrain the depth with only a few observations may have unexpected negative consequences due to trade-offs among origin time, depth, and horizontal location.

Our analysis measures the errors introduced by a shallow depth assumption by comparing the outcomes of two depth scenarios. For the first scenario, we replay the events in our dataset through the ShakeAlert program assuming all earthquakes occur at a fixed depth of 8 km, the depth currently used by the EPIC algorithm in the operational ShakeAlert system. For the second, we fix individual earthquakes at their catalog depth for each ShakeAlert replay. In reality, the depth of an earthquake would never be known prior to locating an event and, therefore, this information could not be used to improve the accuracy of location estimates. However, by setting fixed earthquake depths in this study, we can examine the errors introduced in location, magnitude, and ground-motion predictions when a shallow depth is assumed, without introducing additional errors from performing a depth search. The goals of this work are to determine if applying catalog depth to ShakeAlert algorithms for intraslab earthquakes (1) results in a more rapid estimation of accurate earthquake location and magnitude, (2) reduces the number of missed and false alerts by improving the accuracy of MMI alert threshold contours, and (3) improves warning times.

2 DATA

2.1 PNW earthquakes

Our PNW dataset is composed of five intraslab earthquakes (**Fig. 3.1a**) that were recorded between 1999 and 2015. Earthquake depths range from 40 to 62 km with local or moment magnitudes of 4.7–6.8. We identify PNW intraslab earthquakes based on their location relative to the Juan de Fuca plate, depth relative to the locked interface and base of the North American crust, and faulting style. We select non-thrust faulting style earthquakes at depths greater than the average maximum crustal depth (42–47 km depth; Miller *et al.*, 1997). We exclude thrust faulting events since it is unlikely that intraslab earthquakes would exhibit this

faulting style. Hypocenters must be located within the Juan de Fuca slab based on the Slab2 model (Hayes *et al.*, 2018) and below estimated depth limits of the locked zone. We estimate the maximum depth of the seismogenic interface based on the up-dip limit of nonvolcanic tremor (dashed line in **Fig. 3.1a**), which ranges between depths of about 25 km and 35 km (Frankel *et al.*, 2015). We use a depth tolerance of +/- 20 km to account for poorly located events. Faulting styles are determined from triangle diagrams (Frohlich, 1992) computed with focal mechanism information from the Global Centroid Moment Tensor (Global CMT) project, as well as the Pacific Northwest Seismic Network (PNSN) and U.S. Geological Survey (USGS) National Earthquake Information Center (NEIC) earthquake catalogs (see Data and Resources). Information about individual earthquake locations, magnitudes, number of recordings, and faulting mechanisms are available in **Table S3.1** of the supplementary material.

2.2 Chilean earthquakes

A major challenge to testing the performance of ShakeAlert algorithms in the PNW is the low level of background seismicity. Therefore, we supplement the PNW dataset with 32 intraslab earthquakes from Chile with depths of 44–124 km and moment magnitudes ranging from 5.1 to 6.7. Chile is located along a subduction zone formed by the Nazca plate subducting beneath the South American plate (**Fig. 3.1b**). Chilean intraslab earthquakes are identified based on their location relative to the South American slab and the down-dip limit of the seismogenic plate interface (dashed line in **Fig. 3.1b**) as defined in Hayes *et al.* (2018). Selected events are at depths below the average maximum crustal depth for Chile (~44 km; Chulick *et al.*, 2013). All events with thrust faulting focal mechanisms are excluded from the dataset, except one at a depth of 110 km. Focal mechanism information is from the Global CMT Project. Some Chile earthquakes do not have focal mechanisms—but for this project, it is sufficient to assume they

are intraslab earthquakes based on their depths (> 80 km) and their locations relative to the South American slab, since our earthquake sources are modeled as simple point sources and do not require detailed faulting information. **Table S3.2** in the supplementary material contains information about individual earthquake locations, magnitudes, number of recordings, and faulting mechanisms.

2.3 Data format

All earthquake recordings must be in integer miniSEED format for historic replay through the ShakeAlert program. PNW accelerometer and broadband data are downloaded as miniSEED files from the Incorporated Research Institutions for Seismology (IRIS) Data Management Center in units of counts. Chile accelerometer data, downloaded from the Centro Sismológico Nacional (CSN) website, are available in units of m/s^2 and requires a conversion from float to integer format. Each value is multiplied by a scale factor of 1.0×10^8 to prevent rounding of significant digits prior to converting data files to miniSEED format. Chile broadband data are downloaded as miniSEED files from the Federation of Digital Seismograph Networks (FDSN) in units of counts. See Data and Resources to access data from the IRIS, CSN, and FDSN databases.

2.4 Peak ground shaking and intensity measurements

For our performance analysis, we measure peak ground motions at each accelerometer. We use accelerometers and broadband stations to detect and characterize events during ShakeAlert replays. However, recordings from broadband stations are often clipped, which leads to inaccurate peak ground measurements, and therefore we exclude them from the subsequent performance analysis.

PNW data are converted from counts to m/s^2, demeaned, tapered, high-pass filtered at 0.075 Hz, and integrated to velocity. Chilean data are processed similarly, but do not require a unit conversion. At each time sample, the peak ground acceleration (PGA) and peak ground velocity (PGV) up to that time are computed from the vector sum of the two horizontal waveform components, resulting in a PGA and PGV time series. A modified Mercalli intensity (MMI) time series is then computed from the PGA and PGV time series using equation 3 from Worden *et al.* (2012)—a peak ground motion to MMI relation. The MMI time series is used to measure the time (relative to earthquake origin time) when particular MMI alert thresholds are first exceeded at each site. Using the vector sum of the horizontal waveform components maximizes peak ground measurements. Therefore, MMI alert thresholds may be exceeded earlier in the timeseries than if an alternate method (e.g., geometric mean) were used to combine horizontal components. These measurements are used to compute warning times, which are defined in the results section.

3 METHODS

To perform ShakeAlert replays of our earthquake dataset, we use the same procedure for replaying events as described in Cochran *et al.* (2018) except that we use one instance per run instead of four. When an event is detected, ShakeAlert is typically set up to simultaneously compute earthquake source parameters with the EPIC and FinDer algorithms and use a combination of both solutions to predict ground motions (Kohler *et al.*, 2020). For this project, we use only EPIC to characterize the earthquake source as there are no FinDer templates currently available for PNW or Chilean intraslab earthquakes.

The EPIC algorithm uses *P*-wave information recorded at a minimum of four stations to estimate origin time, epicentral location, and magnitude of an earthquake. All replays use

accelerometers and broadband stations to detect and characterize the earthquake, except for one Chilean event where no broadband data are available. For catalog depth scenario replays, PNW and Chilean earthquakes are fixed at the USGS NEIC catalog depth (**Table S3.1** and **S3.2**). Travel time tables for each earthquake, at either the true catalog depth or a fixed depth of 8 km, are calculated using the AK135 velocity model (Kennett *et al.*, 1995). The EPIC algorithm uses trilateration and a grid search to estimate event location and origin time and estimates earthquake magnitude using an empirical scaling relationship between magnitude and *P*-wave displacement amplitude (Kuyuk and Allen, 2013).

Some modifications to EPIC are required to complete our study. The filter-bank teleseismic filter (Chung *et al.*, 2019), used to differentiate between local and teleseismic earthquakes, has been turned off because it requires earthquake recordings with 30 seconds of data prior to an earthquake trigger. Most of the PNW and Chilean earthquake recordings are triggered data and do not contain enough pre-event data for this feature to work properly. To account for the sparse distribution of stations in Chile compared to the West Coast of the United States, the maximum station-to-event distance used to estimate earthquake location and magnitude is increased from 200 to 300 km.

Earthquake source information from EPIC is used by the eqInfo2GM ground-motion module (Thakoor *et al.*, 2019) to predict ground-shaking intensity. Alert messages output intensity information as contours around regions predicted to exceed particular MMI thresholds. Contours are eight-sided polygons centered on an earthquake's estimated epicenter. For a given MMI alert threshold, equation 4 from Worden *et. al.* (2012) is used to convert MMI to PGA and PGV. Using the EPIC magnitude estimate, earthquake depth, and information about the depth-averaged shear-wave velocity within the top 30 m of the Earth's crust (V_{S30}), a ground-motion

model (GMM) is used to compute the epicentral distance at which the PGA and PGV occur. The average of the PGA and PGV distances is used as the contour radius for the MMI alert threshold of interest. ShakeAlert is configured to use a single fixed V_{S30} for computing contours. For the PNW dataset, we use the same value as the operational ShakeAlert system, which is 500 m/s. We use a V_{S30} value of 560 m/s for Chilean earthquakes to reflect the average V_{S30} in Chile from the USGS global V_{S30} map (Worden *et al.*, 2015). For both the PNW and Chile, we use the Zhao *et al.* (2006; referred to as Zea06 for the remainder of this article) GMM to calculate PGA and 1.0 s pseudospectral acceleration (PSA). PGV is then derived from PSA at 1.0 s using the relation of Newmark and Hall (1982), because the Zea06 relationship does not predict PGV. We treat shallow depth scenarios as crustal earthquakes and apply Zea06's crustal earthquake coefficients and a focal depth of 8 km when computing peak ground motions. For catalog depth scenarios, we apply the GMM's intraslab earthquake coefficients and use each earthquake's true depth as the focal depth parameter. Hypocentral distance is used for the distance parameter.

EqInfo2GM also outputs ground shaking intensity information in map format. At each point on a 0.2° resolution grid, a GMM is used to compute ground motions from the predicted magnitude, predicted source-to-grid-point distance, and site-specific V_{S30}. Contours are used to generate alerts for the general public. Ground motion maps, which take longer to compute, are more appropriate for alerting technical users who can use the higher resolution information to find ground-motion predictions closest to their specific facilities.

4 RESULTS

4.1 Comparison of catalog and shallow depth EPIC predicted earthquake source parameters

For each alert update of a historic earthquake replay, we measure the epicentral location error (distance between the catalog epicenter and the predicted epicenter in kilometers). Comparison of the results of the two depth scenarios reveal that, in general, shallow depth replays are more likely to generate larger location errors (> 50 km) than catalog depth replays (**Fig. 3.2**). 40% of shallow depth replays have at least one update where the estimated earthquake location is greater than 50 km from the catalog epicenter. Only 8% of catalog depth replays have at least one update with a location error of 50 km or greater. **Figure 3.2b** shows that location estimates do not necessarily improve by the final update. For the first and final alerts, catalog depth location errors are less than shallow depth location errors for 84% of the replays.

We also measure the magnitude error for each alert update (catalog magnitude - predicted magnitude). A comparison of catalog and shallow depth magnitude error (**Fig. 3.3**) does not show the same pattern of larger errors for shallow depth replays that we see with epicentral location estimates. For the first alert and final alerts, the absolute value of the catalog depth magnitude error (not considering whether magnitude is under or overpredicted) is less than the absolute value of the shallow depth magnitude error for 51% of replays. The first alert mean magnitude error is 0.09 and 0.18 magnitude units for shallow depth replays and catalog depth replays, respectively, indicating that both scenarios tend to underpredict initial magnitude estimates. For the final alert update, magnitude estimates tend to be overpredicted by both depth scenarios (shallow depth mean, -0.23 magnitude units; catalog depth mean, -0.12 magnitude

units). In general, magnitude estimates for both depth scenarios improve by the final alert update (**Fig 3.3b**).

4.2 Comparison of catalog and shallow depth MMI alert threshold contours

We assess the accuracy and timeliness of eqInfo2GM MMI alert threshold contours by classifying accelerometer sites using a modified version of the performance metrics described in Meier *et al.* (2020). If a site falls within the boundaries of an MMI threshold contour prior to observed ground motion exceeding the MMI threshold of interest at that location, then it is classified as true positive (TP). If ground motion does not exceed the alert threshold, but the site falls within the bounds of the contour it is considered a false positive (FP). If a site is located outside of the contour, but exceeds the alert threshold, it is considered a false negative (FN). Sites that are alerted after the threshold is exceeded, or with less than one second of warning time, are also considered false negatives. A site that does not receive an alert and does not exceed the alert threshold is classified as a true negative (TN). For our performance evaluation, we are interested in alert thresholds of MMI III (MMI 2.5 - MMI 3.4) and MMI IV (MMI 3.5 - MMI 4.4). We focus on these alert thresholds in particular because the delivery mechanisms currently available for issuing alerts (McGuire *et al.*, 2021) define their alerting criteria for MMI III–MMI V. We omit MMI V from our analysis because several of the events in our dataset do not exceed this intensity.

When classifying stations, we consider all alert updates. Several alert messages may be generated by the ShakeAlert system for a single earthquake. Over time, as more data is collected from stations, the algorithms will refine the estimated source parameters and predicted ground motions. This feature is especially important for very large earthquakes, where the first alert

messages may be sent out while the rupture is still growing. All ShakeAlert replays performed in this study have at least two alert updates.

When the first alert occurs, we classify accelerometers based on the criteria described above. With an alert update, a change in the magnitude or location of the estimated earthquake source can result in a change in the diameter or position of the MMI threshold contour. Thus, all stations not classified as TP with the previous alert are reevaluated. With each consecutive update, any site that is within the previous or current boundaries of the threshold contour, will exceed the alert threshold, and has a warning time greater than one second is considered a TP site. Warning time is defined as the difference between the time when the MMI threshold of interest is exceeded at a site and the time of the alert message when that site falls within the boundaries of the threshold contour for the first time. We measure the time when MMI 2.5 is exceeded for an alert threshold of MMI III and when MMI 3.5 is exceeded for MMI IV. Warning times do not take into consideration system latencies from data telemetry or alert delivery. Examples of this process are illustrated in **Fig. 3.4**, which shows the catalog depth and shallow depth scenario MMI III alert contours for replays of a M_w 5.6 Chilean earthquake at 119 km depth. In **Fig. 3.4a**, the northernmost accelerometer, labeled with a warning time of 40 s, is classified as a false negative until 27 seconds after the predicted origin time when the third alert update (green contour) predicts a magnitude of 5.7 and the boundaries of the MMI III contour expand to include the site. MMI III level shaking reaches the site 67 seconds after the onset of the earthquake. Short warning times at accelerometers inside the first alert contour in **Fig. 3.4** are due to MMI III being exceeded by the *P*-wave.

Using the suite of TP, FP, and FN classified sites, we compute the normalized TP rate (TP/(TP + FN)) and normalized FP rate (FP/(TP + FN)), as defined in Meier (2017) and Cochran

et al. (2018), for the catalog depth and shallow depth replay of each earthquake. These values are used to measure the overall alert quality (OAQ = $((1 - \text{TP rate})^2 + (\text{FP rate})^2)^{1/2}$) of individual replays by finding the distance between the ideal case (TP rate = 1, FP rate = 0) and the actual alert performance. An OAQ value of zero indicates perfect performance.

We compare catalog depth and shallow depth scenario TP rate, FP rate, and OAQ for all earthquakes for an alert threshold of MMI III (**Fig. 3.5a–c**) and MMI IV (**Fig. 3.5d–f**). For MMI III, catalog depth improves TP rates for 16% of events, but worsens them for 25% of events. For 59% of earthquakes, the catalog and shallow depth TP rates are identical. 92% of catalog and shallow depth replays have identical or zero FP rates and no catalog replays have higher FP rates than shallow depth replays. Catalog depth replays perform better (have smaller OAQs) for 14% of events, perform worse for 29% of events, and have identical OAQs for 57% of events. For MMI IV, using catalog depth improves TP rates for 39% of events, but makes them worse for 17% of events. 44% of catalog and shallow depth replays have identical TP rates. 6% of catalog depth replays have FP rates smaller than the shallow depth replays of the same event and 92% of events have identical or zero FP rates. We see improved performance (smaller OAQs) from catalog depth over shallow depth replays for 39% of events, worse performance for 19% of events, and identical performance for 42% of events. One PNW earthquake has been excluded from the analysis at MMI IV because the catalog depth replay does not predict that shaking intensity will exceed this alert threshold. For the shallow depth replay, no stations fall within the boundaries of the alert contour, therefore we cannot determine whether the MMI IV prediction is correct.

Although we do not have enough higher magnitude events in the dataset to perform our analysis for MMI V, the 2001 M_w 6.8 Nisqually earthquake can provide at least one example of

how ShakeAlert performs at this alert level. For this event, source estimates are very similar between catalog and shallow depth replays, so differences in the contour radii are controlled by the Zea06 GMM. The replays show that the MMI V contour radii predicted by the Zea06 crustal GMM for a depth of 8 km are smaller than those predicted by the Zea06 intraslab GMM for a depth of 52 km. Underpredicted shallow depth contour radii result in missed alerts at two sites that are classified as TP for the catalog depth replay.

4.3 Comparison of catalog and shallow depth warning times

We compare catalog depth and shallow depth warning times for MMI III (**Fig. 3.6a**) and MMI IV (**Fig. 3.6b**). For all earthquakes, warning times are compared between stations that are classified as TP for both depth scenarios. Our results show that the difference between catalog depth and shallow depth warning times is less than +/- 1 second for 72% of stations for MMI III and 70% of stations for MMI IV. Only 11% of catalog depth warning times are at least one second longer than shallow depth warning times for either alert threshold.

5 DISCUSSION

In this study, we examine how the simplifying assumption of a fixed shallow depth of 8 km affects the accuracy and timeliness of EEW alerts for intraslab earthquakes in the PNW. To isolate the errors introduced in ShakeAlert source estimates and ground-motion predictions from using an incorrect source depth, we replay a suite of 37 PNW and Chilean deep intraslab earthquakes and compare the outcomes of a catalog depth and a shallow depth scenario. Our analysis is used to determine whether it is advisable to constrain earthquake depth within earthquake early warning algorithms.

Our results show that, in general, shallow depth replays are more likely than catalog depth replays to have at least one alert update where the location error is greater than 50 km, but

that this is largely due to the configuration of network stations (**Fig. 3.1**). Chilean earthquakes that produce large location errors during a shallow depth replay have catalog epicenters located outside of the Chilean National Seismic Network (e.g., **Fig. 3.4**). For this project, we chose only to use stations inside Chile. However, intraslab earthquakes within the subducting South American slab extend beyond the country's borders (**Fig. 3.1b**). Location estimates of inland deep events might be improved by including station recordings from Bolivia or Argentina. Improvement of location estimates for coastal intraslab earthquakes may require offshore instrumentation. A poor epicentral location estimate can reduce alert quality, such as for the earthquake shown in **Figure 3.4b**; for this shallow depth replay, the third update (green contour) predicts an earthquake location ~250 kilometers away from catalog epicenter, shifting the alert region eastward. The shift in the contour location results in missed alerts at sites that are classified as TP in the catalog depth replay. See **Figure S3.1b** in the supplementary material for MMI IV contour results for this event. This earthquake is marked as a black filled circle in **Figure 3.5** to show how a large location error affects alert performance for this particular event. Only one PNW earthquake, an M_w 5.8 at 40 km depth, produces similarly large location errors (diamonds in **Fig. 3.2**). This earthquake occurred in 1999, when most accelerometers and broadband stations in Washington State were located in the Puget Sound region (**Fig. 3.1a**) northeast of the earthquake epicenter. When considering all events, first and final alert catalog depth location error tends to be smaller than shallow depth location error. However, since we cannot know the depth of an earthquake prior to locating the event, a more useful observation is that for events that locate within a seismic network, most catalog depth and shallow depth replays have similar epicenter estimates, regardless of the depth accuracy.

Unlike the location estimates, there appears to be no relationship between the accuracy of magnitude estimates and depth accuracy (**Fig. 3.3**). This is unsurprising since the Kuyuk and Allen (2013) P_d-to-magnitude relation contains an epicentral distance factor but does not take into account earthquake depth. On average, first alerts underestimate magnitude and final alerts overestimate magnitude for both depth scenarios. Magnitude errors are typically larger for Chilean earthquakes than PNW events (**Fig. 3.3**). We note that Kuyuk and Allen (2013) was developed from Japanese and Californian earthquakes; it has been tested in the PNW (Hartog *et al.*, 2016), but may not be suitable for magnitude predictions in Chile. Magnitude estimates might be improved by using a region-specific magnitude scaling relation (e.g., Lancieri *et al.*, 2011). For the first alert, we note that larger magnitude errors do not generally coincide with larger location errors (**Fig. 3.7a**). Since only a small amount of *P*-wave information (4 seconds) is used to initially characterize an event, it is difficult to discern if there is a relationship between inaccurate early location and magnitude estimates. However, we do observe a correspondence between larger magnitude errors and larger location errors with the final update (**Fig. 3.7b**). For events with distance errors greater than 50 km, the absolute value of the magnitude error is at least 0.4 magnitude units. Only the 1999 PNW earthquake in particular, mentioned in the previous paragraph (diamond shape in **Fig. 3.2**, **3.3**, and **3.7**), shows an increase in magnitude and location error with each consecutive alert update of the shallow depth replay.

Our comparison of catalog depth and shallow depth scenario warning times show that applying catalog depth (i.e., increasing hypocentral distance) to intraslab earthquakes improves warning times by at least one second for only 11% of stations for MMI alert thresholds III and IV. This result is similar to the observations from Meier *et al.* (2020) for JMA Intensity 2.0–3.0 (equivalent to MMI 3.3–4.1), where they found the range of warning times to be similar

regardless of earthquake type. For example, Meier et al. found that for either shallow crustal or nonshallow crustal earthquakes, 25% of sites were expected to receive ~40 s warning time. In our study, for MMI III and IV, around 70% of our shallow depth replays had warning times within +/- one second of catalog depth warning times. This indicates that catalog depth and shallow depth replay alert times are very similar, and that processing time is not decreased by using catalog depth.

Determining the relationship between overall alert quality and depth accuracy is challenging because of the trade-offs between the parameters discussed above. For example, the first alert from a shallow depth replay may generate a poor location estimate. Depending on the estimated magnitude, the contour region may be larger than would be predicted using the actual earthquake depth. The poor location would shift the alert region away from sites, but the larger than expected contour region would include all sites that require warning. If there are no FP sites within the alert region, as is the case with all 32 Chilean events for an alert threshold of MMI III (**Fig. 3.5b**), the calculated overall alert quality would indicate perfect performance.

Though we cannot attribute good performance with good alert accuracy, the fact that catalog depth scenarios only outperform (have lower OAQs) shallow depth scenarios for 14% of events for an alert threshold of MMI III and 39% of events for MMI IV, suggests that overall alert quality is not strongly impacted by errors in contour size and placement caused by applying a fixed shallow depth when locating events or computing the size of alert contours.

6 CONCLUSIONS

We aimed to determine if applying catalog depth to ShakeAlert algorithms for intraslab earthquakes results in a more rapid estimation of accurate earthquake location and magnitude, reduces the number of missed and false alerts by improving the accuracy of MMI alert threshold

contours, and improves warning times. Our results demonstrate magnitude estimates are generally insensitive to depth accuracy and that when located within a seismic network, catalog depth and shallow depth scenario epicenter estimates yield similar alerting accuracy in terms of MMI contour areas and timeliness. We also find that warning times and overall alert quality are not improved by applying catalog depth.

In the PNW the EEW station distribution is sufficiently dense and uniform around the region where deep earthquakes are expected to occur (Bostock et al., 2019; note location of earthquake epicenters relative to stations in **Fig. 3.1a**). Therefore, our analysis indicates that using a fixed shallow depth for moderate-magnitude intraslab earthquakes in the PNW will not have a significant impact on alert accuracy and timing for alert thresholds of MMI III and IV. This conclusion, however, does not apply to all subduction zones, particularly in regions where intraslab earthquakes have a greater potential to locate outside of seismic networks.

7 FIGURES

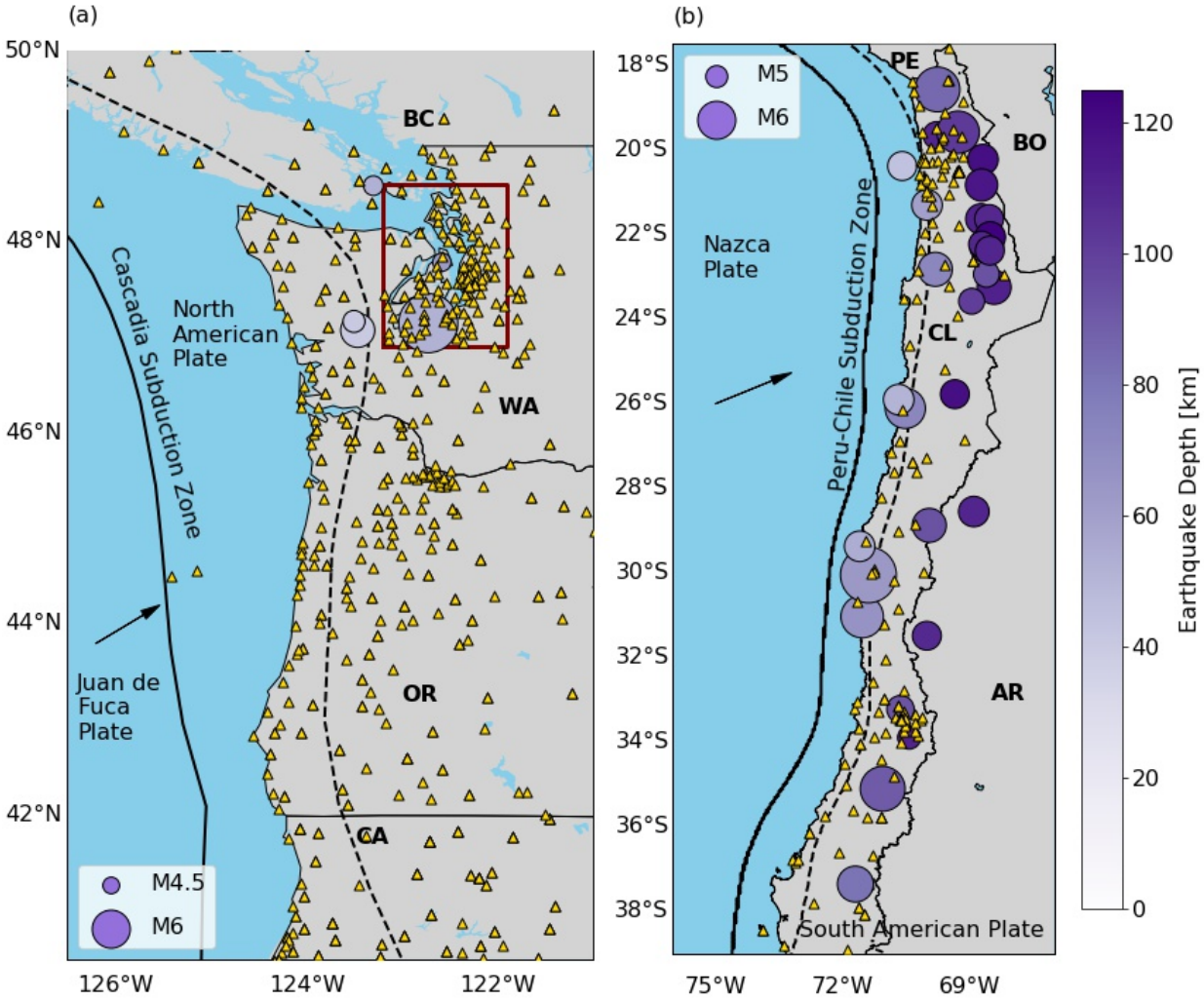

Figure 3.1: (a) Map of Pacific Northwest (PNW) intraslab earthquakes used in this study. Filled circles indicate earthquake locations. Triangles show the configuration of seismic stations used by the operational ShakeAlert system as of May 2021. Boxed area is the approximate location of the Puget Sound region. Solid line denotes the plate boundary. Dashed line is the approximate up-dip limit of non-volcanic tremor, which we use to approximate the maximum down-dip limit of the seismogenic plate interface (Frankel *et al.*, 2015). Arrow indicates the convergence direction of the subducting Juan de Fuca plate. BC, British Columbia, Canada; CA, California; OR, Oregon; WA, Washington. **(b)** Map of Chilean intraslab earthquakes. Filled circles and solid line are the same as in (a). Triangles show the distribution of seismic stations in Chile as of May 2021. Dashed line is the 45 km depth contour of the South American slab interface in the Slab2 model, approximating the down-dip limit of the seismogenic zone as defined in Hayes *et al.*, (2018). Arrow indicates the convergence direction of the subducting Nazca plate. AR, Argentina; BO, Bolivia; CL, Chile; PE, Peru. Note that the current distribution of stations shown in (a) and (b) were not all operational during the time when most of the earthquakes in our dataset were recorded. Tables S3.1 and S3.2 in the supplementary material list the number of station recordings for each PNW and Chilean earthquake, respectively.

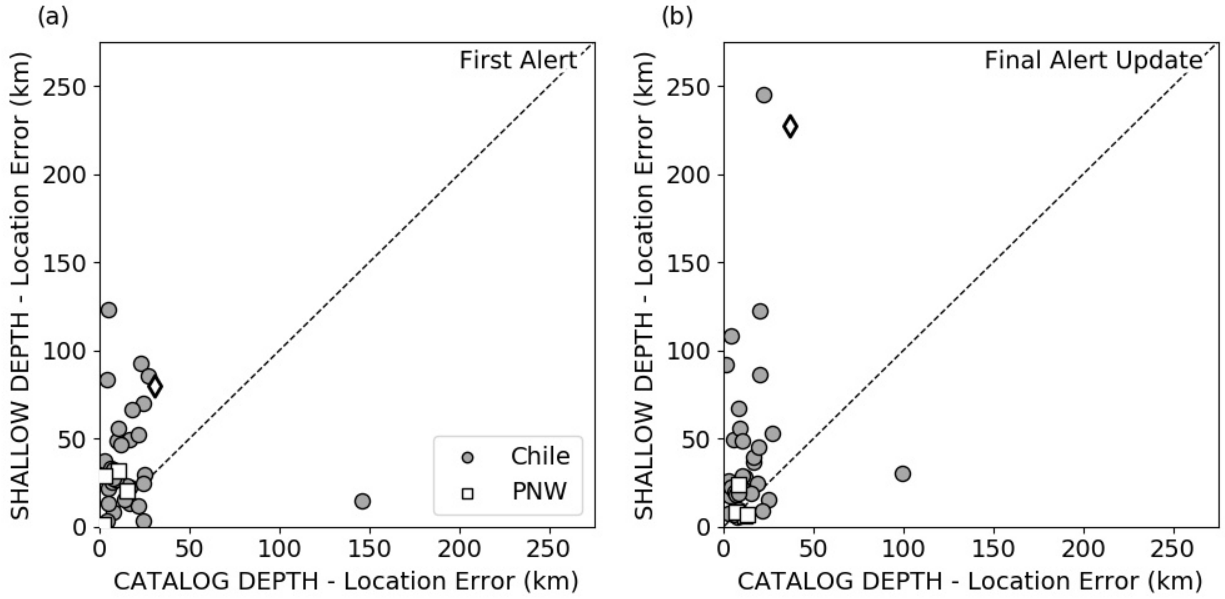

Figure 3.2: For all earthquakes in this study, a comparison of shallow depth scenario and catalog depth scenario epicentral location error (distance between catalog epicenter and predicted epicenter in kilometers) for the **(a)** first alert and **(b)** final alert update. Diamond is an M_w 5.8 PNW earthquake at 40 km depth, recorded in 1999 when most accelerometers and broadband stations in Washington State were located in the Puget Sound region (Fig. 3.1a), northeast of the earthquake epicenter.

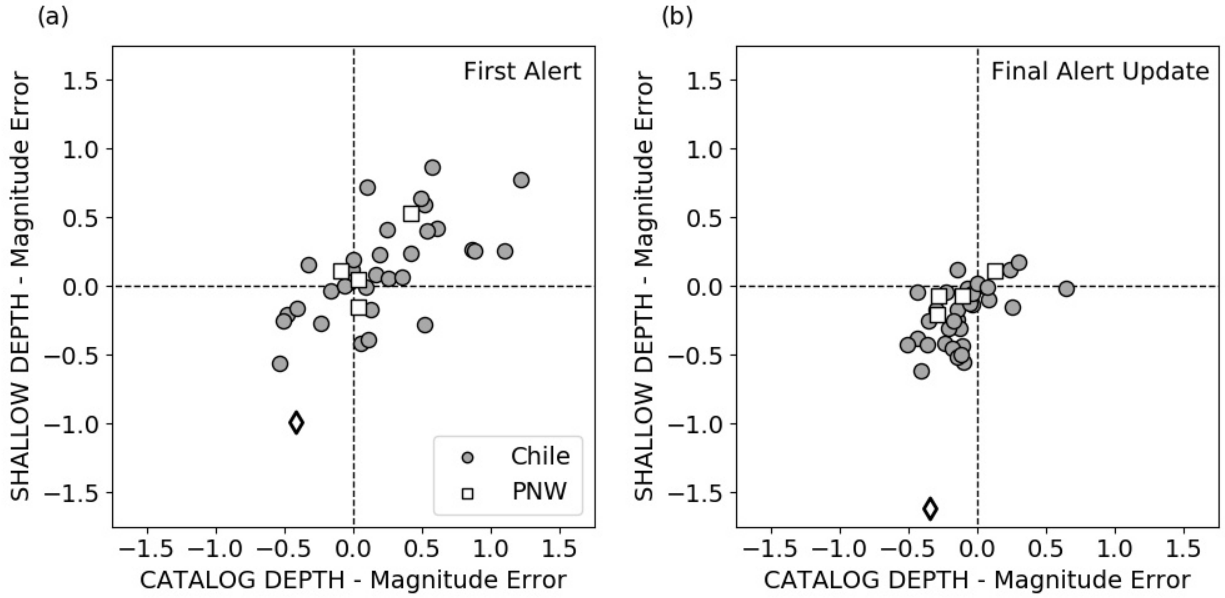

Figure 3.3: Comparison of shallow depth and catalog depth scenario magnitude error (catalog magnitude - predicted magnitude) from the **(a)** first alert and **(b)** final alert updates. Diamond is the M_w 5.8 PNW earthquake at 40 km depth described in the caption for Figure 3.2.

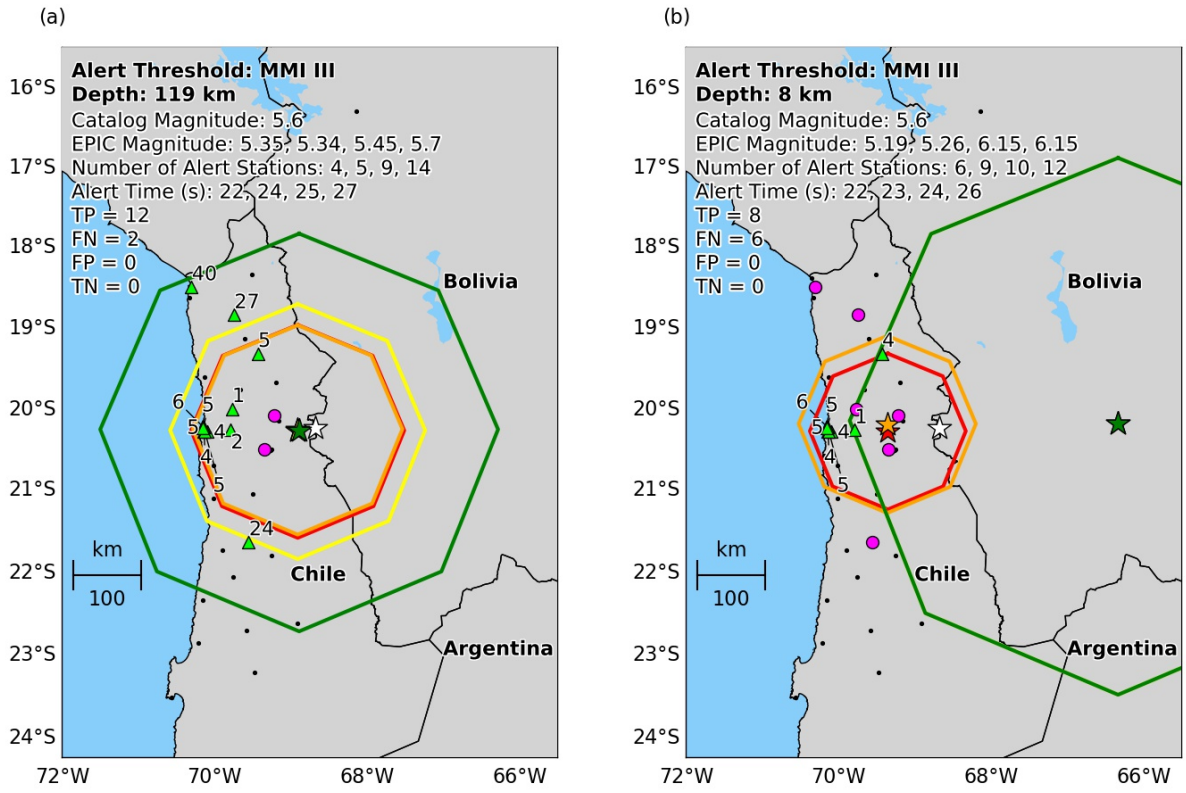

Figure 3.4: Maps of Chile showing stations used in the ShakeAlert replays of a M_w 5.6 earthquake at **(a)** a catalog depth of 119 km and **(b)** a depth of 8 km. Contours are consecutive updates of the region where modified Mercalli intensity (MMI) III+ shaking is expected to occur. All true positive sites (triangles) are labeled with warning times in seconds. Circles are false negative sites. Dots are broadband stations. The white star is the catalog epicenter. Colored stars are estimated epicenters. Colored stars and contours associated with a particular alert update have matching colors. EPIC, Earthquake Point-Source Integrated Code; FN, false negative; FP, false positive; MMI, modified Mercalli intensity; TN, true negative; TP, true positive.

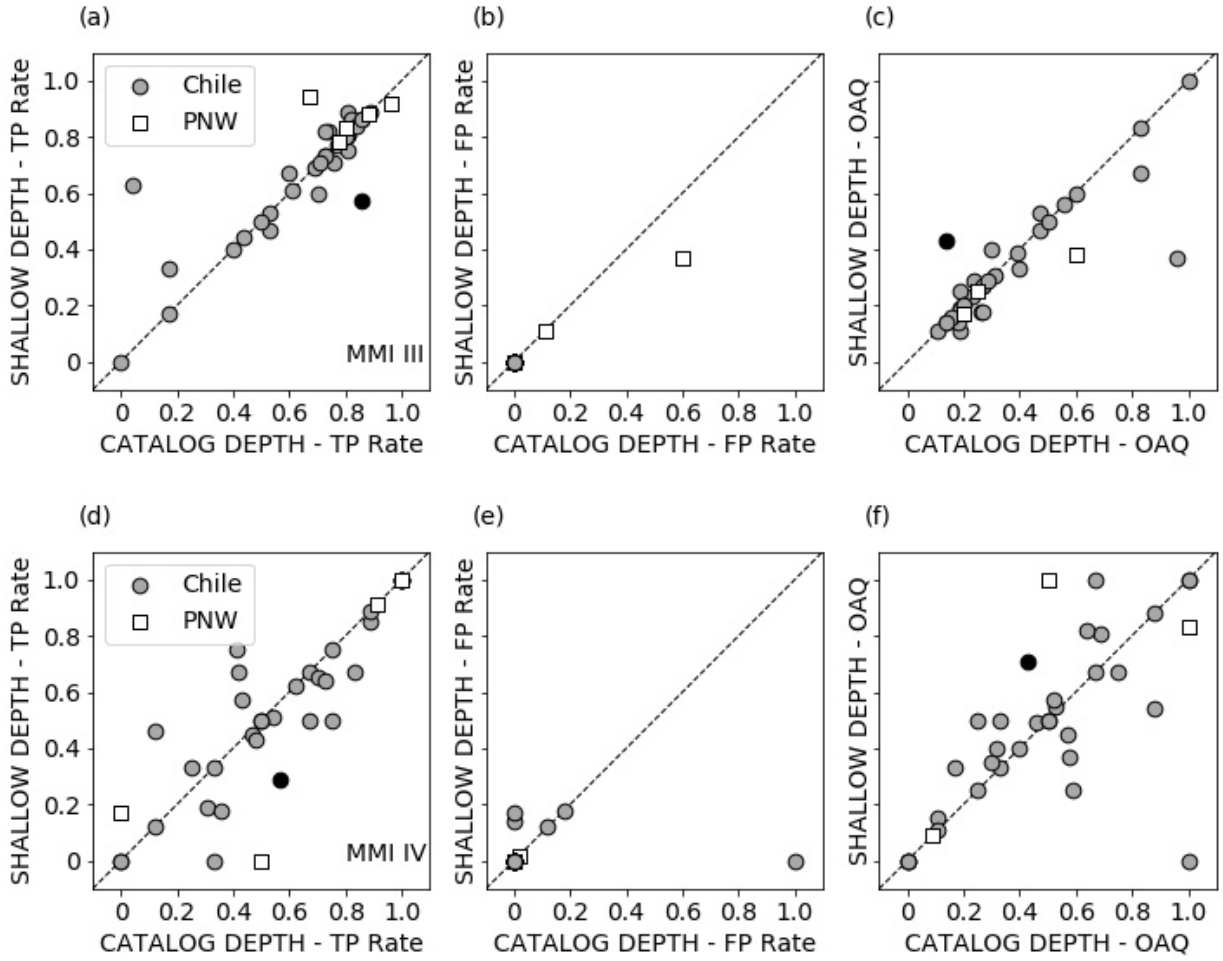

Figure 3.5: Comparison of shallow depth and catalog depth scenario **(a)** true positive (TP) rate, **(b)** false positive (FP) rate, and **(c)** overall alert quality (OAQ) for an alert threshold of MMI III. **(d)–(f)** are the same as (a)–(c) for MMI IV. Black circle is the M_w 5.6 Chilean earthquake at 119 km depth shown in Figure 3.4.

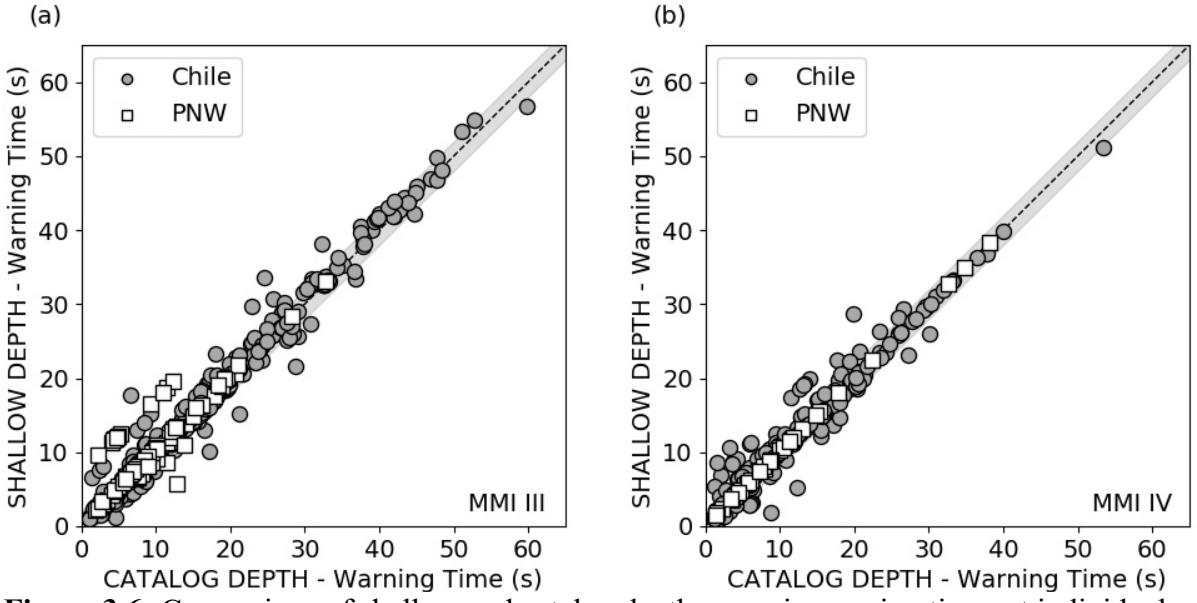

Figure 3.6: Comparison of shallow and catalog depth scenario warning times at individual stations for **(a)** MMI III and **(b)** MMI IV alert thresholds. Warning times are only shown for stations classified as TP for both shallow and catalog depth replays. The shaded area around the dashed line represents +/- 2 seconds warning time.

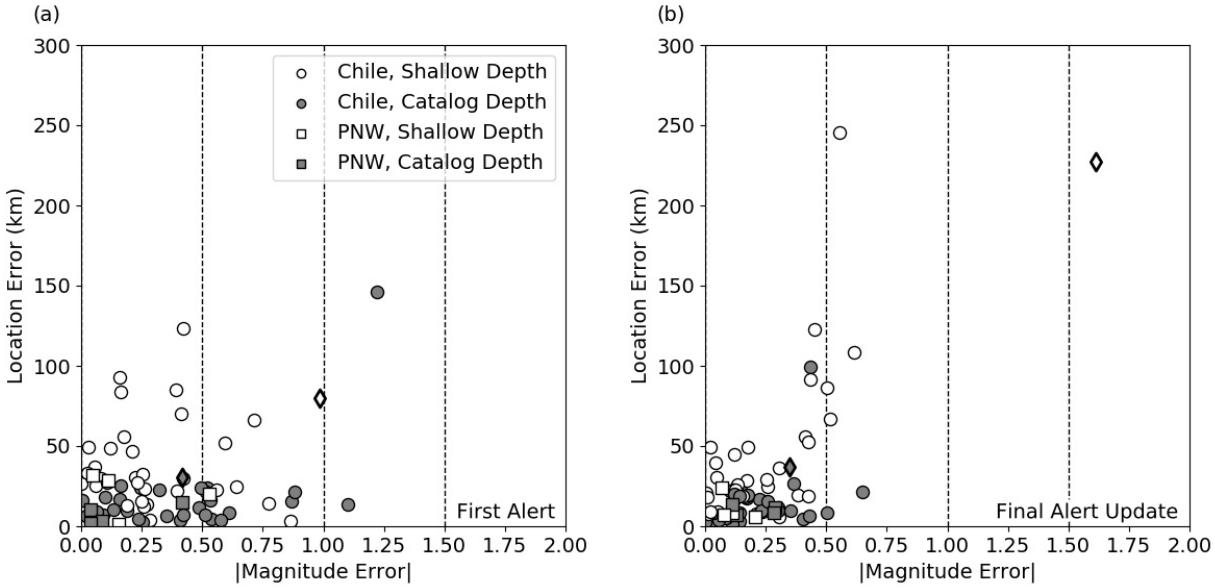

Figure 3.7: Plots showing location error versus the absolute value of the magnitude error for **(a)** the first alert and **(b)** final alert updates. Light and dark diamonds are the shallow and catalog depth location and magnitude errors, respectively, for the M_w 5.8 PNW earthquake at 40 km depth described in the caption for Figure 3.2.

8 SUPPLEMENTARY MATERIALS

Table S3.1: List of Pacific Northwest earthquakes and their source parameters used in this study

Origin time (UTC)	**Latitude** (degrees)	**Longitude** (degrees)	**Depth** (km)	**M**	**Number of acc.**	**Number of broad.**	**Mechanism**
1999-07-03T01:43:54.37	47.074	-123.4637	40.014	5.8*	10	8	Normal
2001-02-28T18:54:32.83	47.149	-122.7267	51.798	6.8*	50	16	Normal
2001-06-10T13:19:11.29	47.1675	-123.5025	40.245	5.0*	49	20	Normal
2009-01-30T13:25:03.76	47.7865	-122.5847	62.24	4.7†	117	120	Strike-slip
2015-12-30T07:39:29.31	48.5865	-123.3003	52.42	4.8†	252	102	Normal

Earthquake information is from the U. S. Geological Survey National Earthquake Information Center earthquake catalog.
M, magnitude
acc., accelerometers
broad., broadband sites
*Moment magnitude
†Local magnitude

Table S3.2: List of Chilean earthquakes and their source parameters used in this study

Origin time (UTC)	**Latitude** (degrees)	**Longitude** (degrees)	**Depth** (km)	**M_w**	**Number of acc.**	**Number of broad.**	**Mechanism**
2013-08-23T08:34:06.92	-22.2741	-68.5927	111.0	5.8	4	35	Normal
2014-03-31T12:53:06.00	-19.511	-69.174	114.5	5.6	6	31	Normal
2014-05-30T15:32:27.00	-21.302	-69.999	59.6	5.6	15	42	Strike-slip
2014-07-23T21:39:08.47	-20.2267	-68.6776	118.73	5.6	14	36	Normal
2014-10-07T05:09:10.00	-19.653	-69.769	109.2	5.4	18	35	Normal
2014-11-10T11:38:59.00	-21.631	-68.725	111.3	5.6	9	38	Normal
2015-01-10T17:55:02.63	-21.6328	-68.5339	108.78	5.5	7	42	Normal
2015-03-28T16:36:53.85	-22.2167	-68.6175	112.0	5.6	10	36	Normal
2015-05-26T10:32:03.35	-22.057	-68.5076	124.0	5.6	7	38	Normal
2015-11-01T15:16:17.48	-23.2468	-68.4169	111.0	5.8	15	37	Normal
2015-11-09T04:46:27.86	-23.5755	-68.9458	101.0	5.3	10	41	Normal
2015-11-10T17:48:23.09	-22.2254	-68.7099	109.34	5.3	6	38	Normal
2016-04-14T09:38:44.10	-33.8833	-70.4192	110.52	5.1	17	37	Thrust*
2016-06-24T21:29:19.02	-25.7705	-69.3417	118.96	5.5	15	59	Strike-slip
2016-07-25T17:26:50.21	-26.1067	-70.5111	72.0	6.1	31	57	Normal
2016-11-04T16:20:44.44	-35.0945	-71.0457	90.0	6.3	22	48	Normal
2017-01-11T21:58:18.41	-22.821	-69.8033	72.0	5.8	19	85	Normal
2017-05-14T19:44:25.16	-20.8287	-68.711	116.0	5.7	13	71	Strike-slip
2017-05-29T14:57:53.86	-37.3446	-71.6896	81.14	5.9	15	89	Normal
2017-06-06T17:35:07.98	-22.9376	-68.5964	93.13	5.3	9	86	Strike-slip
2017-08-01T06:13:56.43	-28.545	-68.8943	110.0	5.6	12	106	Normal
2017-08-02T07:15:13.70	-33.2117	-70.6255	92.0	5.4	27	87	Normal
2017-10-05T08:11:36.97	-22.3793	-68.5172	110.18	5.5	16	78	Normal
2017-10-10T06:32:21.17	-18.5715	-69.7526	85.0	6.3	47	38	N/A†
2018-04-05T11:12:10.60	-20.381	-70.5855	44.0	5.5	26	70	Strike-slip
2018-04-10T10:19:34.37	-31.0258	-71.5292	66.0	6.2	57	61	Normal

2018-09-07T02:39:17.95	-28.8696	-69.9459	93.13	5.8	36	96	Normal
2018-11-01T22:19:51.69	-19.5827	-69.2656	102.0	6.2	28	0	N/A[†]
2019-01-20T01:32:52.48	-30.0404	-71.3815	63.0	6.7	38	56	Normal
2019-01-30T07:44:45.25	-25.8985	-70.6676	51.0	5.6	17	96	Normal
2019-04-18T04:06:34.94	-29.3648	-71.5891	54.0	5.6	11	120	Normal
2019-05-20T11:18:33.13	-31.4782	-70.0028	108.0	5.5	5	109	Strike-slip

Earthquake information is from the U. S. Geological Survey National Earthquake Information Center earthquake catalog.
M_w, moment magnitude
acc., accelerometers
broad., broadband sites
[*]Unlikely to be an interface earthquake. Hypocenter is much deeper (>> 45 km depth) than the seismogenic interface.
[†]No fault plane information available.

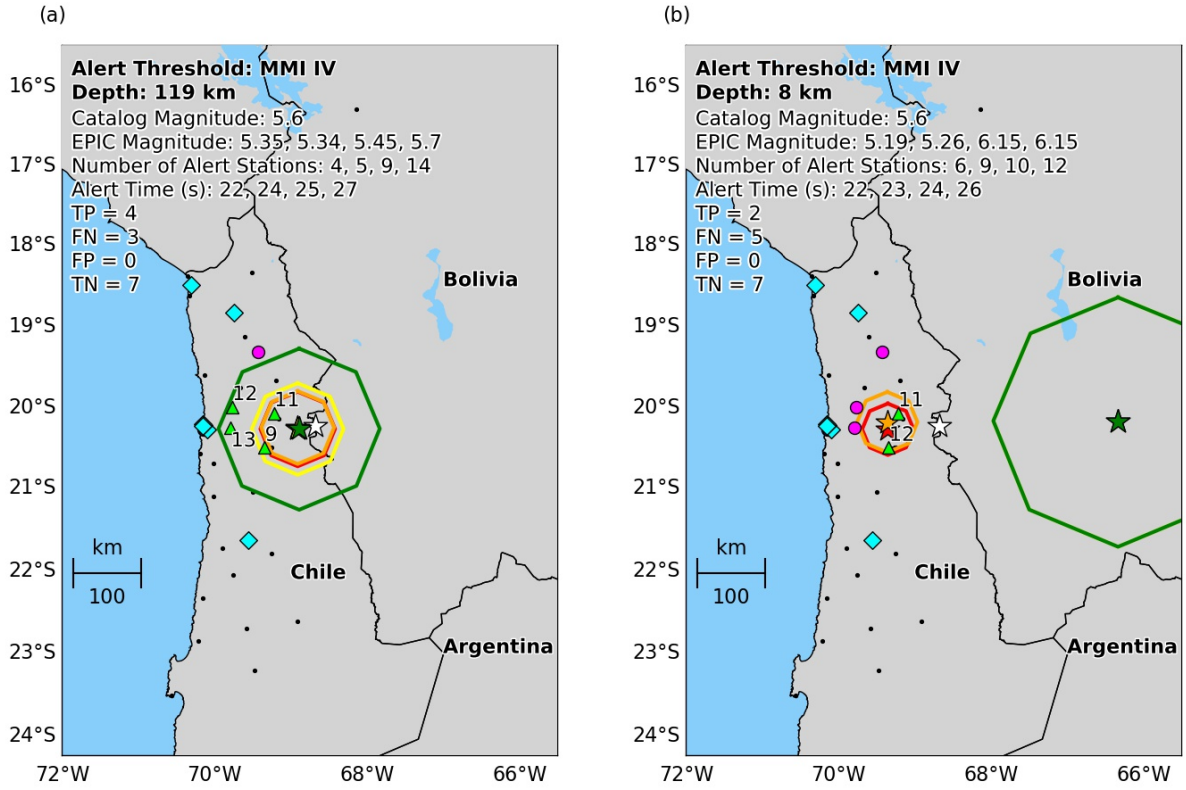

Figure S3.1: Maps of Chile showing stations used in the ShakeAlert replays of an M_w 5.6 earthquake at **(a)** a catalog depth of 119 km and **(b)** a depth of 8 km. Contours are consecutive updates of the region where MMI IV+ shaking is expected to occur. All true positive sites (triangles) are labeled with warning times in seconds. Circles are false negatives and diamonds are true negatives. Dots are broadband stations. The white star is the catalog epicenter. Colored stars are estimated epicenters. Colored stars and contours associated with a particular alert update have matching colors. EPIC, Earthquake Point-Source Integrated Code; FN, false negative; FP, false positive; MMI, modified Mercalli intensity; TN, true negative; TP, true positive.

9 DATA AND RESOURCES

Focal mechanism information used in this study are downloaded from the Global Centroid Moment Tensor (Global CMT) Project using https://ds.iris.edu/spud/momenttensor (last accessed August 2019), the Pacific Northwest Seismic Network (PNSN) earthquake catalog (last accessed August 2019) using https://www.pnsn.org/events?custom_search=true, and the U.S. Geological Survey (USGS) National Earthquake Information Center (NEIC) earthquake catalog (last accessed August 2019) using https://earthquake.usgs.gov/earthquakes/search/. Pacific Northwest (PNW) data is available in miniSEED format from the Incorporated Research Institutions for Seismology Data Management Center (IRIS-DMC, www.iris.edu; last accessed August 2020). The Chilean accelerometer data used in this study are publicly available at http://www.sismologia.cl/ (last accessed July 2019) in text format. Broadband recordings of Chilean events are downloaded as miniSEED files from the Federation of Digital Seismograph Networks (FDSN) with the Python ObsPy FDSN Mass Downloader package (last accessed July 2019).

10 ACKNOWLEDGEMENTS

The authors thank Annemarie Baltay, the associate editor of Seismological Research Letters, and two anonymous reviewers for comments that helped improve this article.

11 REFERENCES

Bostock, M. G., N. I. Christensen, and S. M. Peacock (2019). Seismicity in Cascadia, *Lithos* **332/333**, 55–66, doi: 10.1016/j.lithos.2019.02.019.

Böse, M., D. E. Smith, C. Felizardo, M.-A. Meier, T. H. Heaton, and J. F. Clinton (2018). FinDer v.2: Improved real-time ground-motion predictions for M2–M9 with seismic finite-source characterization, *Geophys. J. Int.* **212**, no. 1, 725–742, doi: 10.1093/gji/ggx430.

Brown, H. M., R. M. Allen, M. Hellweg, O. Khainovski, D. Neuhauser, and A. Souf (2011). Development of the ElarmS methodology for earthquake early warning: Realtime application in California and offline testing in Japan, *Soil Dynam. Earthq. Eng.* **31**, no. 2, 188–200, doi: 10.1016/j.soildyn.2010.03.008.

Chulick, G. S., S. Detweiler, and W. D. Mooney (2013). Seismic structure of the crust and uppermost mantle of South America and surrounding oceanic basins, *J. S. Am. Earth. Sci.* **42**, 260–272, doi: 10.1016/j.jsames.2012.06.002.

Chung, A. I., I. Henson, and R. M. Allen (2019). Optimizing earthquake early warning performance: ElarmS-3, *Seismol. Res. Lett.* **90**, no. 2A, 727–743, doi: 10.1785/0220180192.

Cochran, E. S., M. D. Kohler, D. D. Given, S. Guiwits, J. Andrews, M. Meier, M. Ahmad, I. Henson, R. Hartog, and D. Smith (2018). Earthquake early warning ShakeAlert system: Testing and certification platform, *Seismol. Res. Lett.* **89**, no. 1, 108–117, doi: 10.1785/0220170138.

Frankel, A., R. Chen, M. Petersen, M. Moschetti, and B. Sherrod (2015). 2014 Update of the Pacific Northwest portion of the U.S. national seismic hazard maps, *Earthq. Spectra* **31**, no. S1, S131–S148, doi: 10.1193/111314EQS193M.

Frohlich, C. (1992). Triangle diagrams: ternary graphs to display similarity and diversity of earthquake focal mechanisms, *Phys. Earth Planet. In.* **75**, nos. 1/3, 193–198, doi: 10.1016/0031-9201(92)90130-N.

Gomberg, J. S., K. M. Shedlock, and S. W. Roecker (1990). The effect of S-wave arrival times on the accuracy of hypocenter estimation, *Bull. Seismol. Soc. Am.* **80**, no. 6, 1605–1628.

Hartog, J. R., V. C. Kress, S. D. Malone, P. Bodin, J. E. Vidale, and B. W. Crowell (2016). Earthquake early warning: ShakeAlert in the Pacific Northwest, *Bull. Seismol. Soc. Am.* **106**, no. 4, 1875–1886, doi: 10.1785/0120150261.

Hayes, G. P., G. L. Moore, D. E. Portner, M. Hearne, H. Flamme, M. Furtney, and G. M. Smoczyk (2018). Slab2, a comprehensive subduction zone geometry model, *Science* **362**, no. 6410, 58–61, doi: 10.1126/science.aat4723.

Kennett B. L. N., E. R. Engdahl, and R. Buland (1995). Constraints on seismic velocities in the earth from travel times, *Geophys. J. Int.* **122**, no. 1, 108-124.

Kodera, Y., Y. Yamada, K. Hirano, K. Tamaribuchi, S. Adachi, N. Hayashimoto, M. Morimoto, M. Nakamura, and M. Hoshiba (2018). The propagation of local undamped motion (PLUM) method: A simple and robust seismic wavefield estimation approach for earthquake early warning, *Bull. Seismol. Soc. Am.* **108**, no. 2, 983–1003, doi: 10.1785/0120170085.

Kohler, M. D., D. E. Smith, J. Andrews, A. I. Chung, R. Hartog, I. Henson, D. D. Given, R. de Groot, and S. Guiwits (2020). Earthquake early warning ShakeAlert 2.0: Public rollout, *Seismol. Res. Lett.* **91**, no. 3, 1763–1775, doi: 10.1785/0220190245.

Kuyuk, H. S., and R. M. Allen (2013). A global approach to provide magnitude estimates for earthquake early warning alerts, *Geophys. Res. Lett.* **40**, no. 24, 6329–6333, doi: 10.1002/2013GL058580.

Lancieri, M., A. Fuenzalida, S. Ruiz, and R. Madariaga (2011). Magnitude scaling of early-warning parameters for the Mw 7.8 Tocopilla, Chile, earthquake and its aftershocks. *Bull. Seismol. Soc. Am.* **101**, no. 2, 447–463, doi: 10.1785/0120100045.

Lomax, A., A. Michelini, and A. Curtis (2009). Earthquake location, direct, global-search methods. In *Encyclopedia of Complexity and Systems Science, Part 5*, R. A. Meyers (Editor), Springer, New York, New York, 2449–2473, doi: 10.1007/978-0-387-30440-3.

McGuire, J. J., D. E. Smith, A. D. Frankel, E. A. Wirth, S. K. McBride, and R. M. de Groot (2021). Expected warning times from the ShakeAlert earthquake early warning system for earthquakes in the Pacific Northwest, *U.S. Geol. Surv. Open-File Rept. 2021-1026*, 37 pp.

Meier, M., Y. Kodera, M. Böse, A. Chung, M. Hoshiba, E. Cochran, S. Minson, E. Hauksson, and T. Heaton (2020). How often can earthquake early warning systems alert sites with high-intensity ground motion?, *J. Geophys. Res.* **125**, no. 2, doi: 10.1029/2019JB017718.

Meier, M. A. (2017). How "good" are real-time ground motion predictions from earthquake early warning systems?, *J. Geophys. Res.* **122**, no. 7, 5561–5577, doi: 10.1002/2017JB014025.

Miller, K. C., G. R. Keller, J. M. Gridley, J. H. Luetgert, W. D. Mooney, and H. Thybo (1997). Crustal structure along the west flank of the Cascades, western Washington, *J. Geophys. Res.* **102**, no. B8, 17857–17873, doi: 10.1029/97JB00882.

Newmark, N.M., and W.J. Hall (1982). Earthquake spectra and design, *Geotechnique* **25**, no. 2, 139-160.

Petersen, M. D., M. P. Moschetti, P. M. Powers, C. S. Mueller, K. M. Haller, A. D. Frankel, Y. Zeng, S. Rezaeian, S. C. Harmsen, O. S. Boyd, *et al.* (2014). Documentation for the 2014 update of the United States national seismic hazard maps, *U.S. Geol. Surv. Open-File Rept.* 2014–1091, 243 pp.

Thakoor, K., J. Andrews, E. Hauksson, and T. Heaton (2019). From earthquake source parameters to ground-motion warnings near you: The ShakeAlert earthquake information to ground-motion (eqInfo2GM) method, *Seismol. Res. Lett.* **90**, no. 3, 1243–1257, doi: 10.1785/0220180245.

Worden, C. B., M. C. Gerstenberger, D. A. Rhoades, and D. J. Wald (2012). Probabilistic relationships between ground-motion parameters and modified Mercalli intensity in California, *Bull. Seismol. Soc. Am.* **102**, no. 1, 204–221, doi: 10.1785/0120110156.

Worden, C. B., D. J. Wald, J. Sanborn, and E. M. Thompson (2015). Development of an open-source hybrid global Vs30 model, SSA Annual Meeting, Pasadena, CA. *Seismol. Res. Lett.* **86**, no. 2B, 713.

Zhao, J. X., J. Zhang, A. Asano, Y. Ohno, T. Oouchi, T. Takahashi, H. Ogawa, K. Irikura, H. K. Thio, P. G. Somerville, *et al.* (2006). Attenuation relations of strong ground motion in Japan using site classification based on predominant period, *Bull. Seismol. Soc. Am.* **96**, no. 3, 898–913, doi: 10.1785/0120050122.

IV A Population-based ShakeAlert performance evaluation for *M* 9 megathrust earthquakes in the Pacific Northwest, United States

1 INTRODUCTION

ShakeAlert—the earthquake early warning (EEW) system for the West Coast of the United States—is currently a network-based system that uses *P*-wave information detected at seismic stations to estimate the magnitude and location of an on-going earthquake and predict the spatial extent where ground shaking is likely to be felt. This information is used as criteria by various delivery mechanisms (e.g., Integrated Public Alert and Warning System Wireless Emergency Alerts, Android "be aware" and "take-action" alerts, MyShake alerts) for issuing alerts to end-users in the path of imminent shaking. Originally designed for alerting in California where most seismicity is produced by onshore shallow crustal faults, the alerting region has expanded over time to include the Pacific Northwest (PNW) states of Oregon and Washington.

Just off the west coast, extending from Cape Mendocino, California to Vancouver Island, British Columbia, the Juan de Fuca plate converges with the North American plate forming the Cascadia subduction zone (CSZ). Paleoseismic evidence (Atwater, 1987; Goldfinger *et al.*, 2012) has revealed a minimum of about a 10,000 year history of *M* 8+ earthquakes on the CSZ. Full margin ruptures, generating *M* ~9 earthquakes, are expected to occur approximately every 500 years (Goldfinger *et al.*, 2012). The most recent earthquake, a magnitude 8.7-9.2 as estimated from documentation of tsunami-related flooding and damage in Japan, occurred on January 26, 1700 (Satake *et al.*, 2003).

Though ShakeAlert has been tested in the PNW for various types of small-to-moderate magnitude seismicity (i.e., offshore earthquakes, crustal and intraslab events; Hartog *et al.*,

2016), it is still largely configured for onshore, shallow (~8 km depth) crustal earthquakes, which may negatively impact the timeliness and accuracy of alerts for offshore subduction zone events. Understanding ShakeAlert's limitations for large offshore megathrust earthquakes is important for guiding future improvements to the system and developing appropriate alerting strategies for the population living in the PNW.

Evaluating the performance of ShakeAlert for subduction zone earthquakes is challenging given the scarcity of moderate-to-large magnitude seismicity of any type in the PNW. In recent studies, researchers have looked toward global seismicity and ground-motion simulations of potential earthquake scenarios to assess the timeliness and accuracy of EEW alerts and estimate warning times. Thompson *et al.* (2021) supplemented a dataset of five PNW intraslab earthquakes with 32 Chilean events to quantify the errors introduced when ShakeAlert uses a fixed shallow depth to estimate source parameters for intraslab events. The authors found that, as long as events locate within a seismic network, ShakeAlert source estimates, accuracy of modified Mercalli Intensity (MMI) alert contours, and warning times are fairly insensitive to the accuracy of earthquake depth for alert thresholds of MMI III-IV. A study by Meier *et al.* (2020) used a dataset of 219 Japanese earthquakes that included several large magnitude (*M* 7+) offshore interface events to compare the timeliness and accuracy of EPIC and FinDer, two source algorithms currently utilized by ShakeAlert, and the ground-motion based algorithm, PLUM, which will be added to a future version of the system. Their analysis demonstrated that all three algorithms had the potential to provide more timely accurate alerts for subduction zone earthquakes than shallow crustal earthquakes because of the greater hypocentral distance between source and sites for noncrustal events. McGuire *et al.* (2021) also used recordings of the 2003 Tokachi-Oki earthquake in Japan and five 3D ground-motion simulations of hypothetical

earthquakes on the CSZ to estimate potential warning times for *M* 8-9 megathrust earthquakes in the PNW. Their results show that, for an offshore *M* 8, warning times will typically be less than 40 s and can be significantly shorter along the coast. For an *M* 9 event, they observed that the amount of time users receive is dependent upon hypocenter location and MMI alert threshold. End-users willing to be alerted for low levels of shaking (i.e., MMI III) could receive between 2-3 minutes of warning time at sites 500 km from the earthquake epicenter. For higher alert thresholds (i.e., MMI V), warning times would typically be less than 30 seconds for *M* 8-9 earthquakes.

We attempt to develop realistic expectations of EEW performance during a future large megathrust earthquake by playing a suite of synthetic seismograms from 3D ground-motion simulations of 30 *M* 9 earthquakes on the CSZ through an offline version of the ShakeAlert system partially optimized for the detection and characterization of large offshore events. Using various performance metrics, we analyze the timeliness and accuracy of earthquake source estimates and measure alert quality at individual seismic stations.

The quality of ShakeAlert products is typically evaluated by comparing ShakeAlert MMI alert threshold contours or ground-motion maps to earthquake ground motions recorded at stations or displayed on ShakeMaps (e.g., Chung *et al.*, 2020; McGuire *et al*., 2021; Thompson *et al.*, 2021). Comparing predicted ground motions to observed ground motions at sites can provide precise measurements of alert accuracy and warning times based on the actual times when specific levels of shaking intensity are exceeded but have limited spatial coverage. Comparisons of ground motion maps of predicted shaking intensity to actual ShakeMaps provide better spatial coverage than a station-based analysis but require making some assumptions about the arrival times of strong shaking to estimate warning times. Neither method provides information about

whether correct and timely alerts coincide with populated areas. With the exception of Minson *et al.* (2020), an analysis of PLUM algorithm performance during the 2019 *M* 6.4 and *M* 7.1 Ridgecrest earthquakes in California, and Saunders *et al.* (2021), a population-based performance comparison of PLUM with ShakeAlert, performance studies have not taken into consideration the distribution of the population within the alerting region when assessing alert quality.

In this study, we also develop a population-based alert classification scheme that builds off of the station-based alert classification scheme described in Thompson *et al.* (2021). We use this method to measure the timeliness and accuracy of EEW alerts and estimate the range of expected warning times for *M* 9 earthquakes on the CSZ with respect to the spatial distribution of the population in the PNW.

2 DATA

Our dataset is composed of synthetic seismograms from simulated *M* 9 earthquakes on the CSZ produced by Frankel *et al.* (2018) and Wirth *et al.* (2018). The dataset includes 30 scenarios with varying hypocenter locations, down-dip rupture extents, and slip distributions to address the various unknowns of a future Cascadia megathrust earthquake. 3D finite-difference simulations (< 1 Hz) and stochastic synthetics (1–10 Hz) are combined to produce broadband waveforms at 631 existing and planned ShakeAlert stations in northern California, Oregon, and Washington (**Fig. 4.1**). The actual ShakeAlert seismic network extends throughout all three states. However, in our analysis, stations are restricted to within the boundaries (defined below) of the velocity model used in the ground-motion simulations. Seismograms below 1 Hz are generated using the 3D finite-difference program of Liu and Archuleta (2002). The code uses a velocity stress formalism and is fourth-order accurate in space and second-order accurate in time.

The compound source model consists of five *M* 8 high stress-drop subevents with short rise times on the deeper portion of the fault superimposed on a background slip distribution with longer rise times. Three possibilities are considered for the farthest down-dip extent of the rupture that match the choices made for the 2014 National Seismic Hazard Maps (**Fig. 4.2**): the top of the nonvolcanic tremor zone (blue contour), the 1 cm/yr locking contour derived from inversion of Global Positioning System and uplift data (red contour), and the midpoint between the edge of the fully locked zone and the 1 cm/yr locking contour (green contour). Hypocenter locations range between about 40.7° N-49° N latitude (**Fig. 4.2**). Seismic wave energy is propagated through a 3D velocity model of the CSZ (hereafter, Cascadia Velocity Model or CVM, Stephenson *et al.*, 2017) that extends from 40.2° N to 50° N latitude, ~121° W to 129° W longitude, and ~60 km depth (boxed region in **Fig. 4.1**). The simulations are run out to 400 s after the event origin time. The long duration produces instabilities and edge effects in some seismograms after about 300 s. The time series are truncated to exclude these artifacts. Point-source stochastic synthetics are calculated for frequencies up to 10 Hz using the SMSIM program (Boore, 1983, 1996), and assuming that high frequencies are generated by high stress-drop subevents. Low and high frequency synthetics are combined using a matched filter at 1 Hz.

The original synthetic waveform files contain real numbers in units of cm/s^2. To play the data through the ShakeAlert program, the data is first multiplied by a scale factor of 1.0×10^5 to prevent rounding of significant digits and then converted to integer miniSEED files. Random noise is added to the waveforms to prevent the EPIC short term average/ long term average filter from dividing by zero at the beginning of the earthquake recordings. The miniSEED files are then converted to Earthworm tankplayer files (see Data and Resources).

3 METHODS

We play our *M* 9 scenario tankplayer files through an offline version of the ShakeAlert system modified for the detection and characterization of large offshore earthquakes, using the procedures described in Cochran *et al.* (2018) except we perform one run per scenario instead of four. Cochran *et al.* (2018) use the results from the average of multiple runs per event to account for nondeterministic behavior caused by multithreading (i.e., the concurrent execution of multiple threads by a single program). When earthquake seismograms are played through the system, multithreading can change the order in which data packets are processed, resulting in slight variations in magnitude, location, origin time, and alert times between runs. Since these values generally vary by less than 5%, we determine one instance per scenario to be sufficient. In the following subsections, we describe the configuration of the operational ShakeAlert system at the time of this writing, our modifications to the system, and the alert classification scheme we use to measure the quality of the results.

3.1 The current operational ShakeAlert system

The current operational ShakeAlert system (version 2.1.5) uses several algorithms to estimate magnitude, location, fault length, and predict ground-shaking intensities. Once shaking is detected at seismic stations, ShakeAlert uses the Earthquake Point-Source Integrated Code (EPIC) algorithm (Chung *et al.*, 2019) and the Finite-Fault Rupture Detector (FinDer) algorithm (Böse *et al.*, 2018) to estimate the earthquake's magnitude, location, and origin time. Using *P*-wave information from a minimum of four stations, EPIC estimates the event location and origin time using trilateration and a two-dimensional grid search that assumes a focal depth of 8 km. Magnitude is predicted using an empirical scaling relationship between magnitude and *P*-wave displacement amplitude (Kuyuk and Allen, 2013). The FinDer algorithm uses peak ground

acceleration (PGA) measurements at sites to estimate the length, orientation, and location of the earthquake source. A binary image of the spatial distribution of PGA amplitudes is created by assigning a value of one to PGAs that exceed a particular PGA threshold and a value of zero to PGAs below that threshold. This image of the observed ground motion is then cross-correlated with a set of precomputed templates for earthquakes with different rupture lengths to determine the length, strike angle, and centroid of an assumed line source. The production ShakeAlert system uses symmetric templates for magnitudes 2.5-8.0, corresponding to rupture lengths of 0.06-300 km, that were created with the Cua and Heaton (2009) ground-motion model (GMM) for crustal California earthquakes. Magnitude is estimated from a crustal magnitude-length scaling relationship (Wells and Coppersmith, 1994). FinDer begins computing solutions once at least two stations have recorded PGAs that exceed 2 cm/s^2. EPIC and FinDer solutions are combined by the Solution Aggregator (SA) algorithm unless FinDer estimates a magnitude greater than or equal to *M* 6. Above *M* 6, unless the EPIC magnitude exceeds the FinDer magnitude, only the FinDer magnitude estimate is reported. The eqInfo2GM ground-motion module (Thakoor *et al.*, 2019) then predicts the spatial extent of ground shaking by using the SA magnitude estimate to select distance values associated with specific MMI levels from precomputed tables. The tables are generated by precomputing distances for magnitudes 3 to 8.5 over 0.02 magnitude unit intervals and MMI thresholds II-XII. For each magnitude and a fixed V_{S30} of 350 m/s, PGA and PGV with distance are computed with a GMM (Chiou and Youngs, 2008 for the PNW). The distances at which specific MMI levels are exceeded are then calculated from the average of the PGA and PGV values using equation (6) and (9) from Worden *et al.* (2012). The distance information is used to calculate the vertices (latitude, longitude coordinates) of a contour polygons centered on the estimated earthquake source that define the maximum

spatial extent where different MMI levels of shaking will be felt. EqInfo2GM alert messages contain contour polygon information for MMI II up to the maximum predicted MMI expected for the current magnitude estimate. ShakeAlert algorithms continuously update source estimates and predicted shaking intensities as an earthquake rupture continues to grow and more data is received at stations. Several updated alert messages are usually generated by the system for a single earthquake.

3.2 ShakeAlert configuration optimization for offshore megathrust earthquakes

The current ShakeAlert system is not optimally configured to alert for earthquakes up to *M* 9 on the Cascadia megathrust fault. In this section, we describe modifications to ShakeAlert algorithms that we have implemented to improve detection and characterization of large earthquakes initiating off the west coast of the United States.

Several configuration changes have been made so that the EPIC algorithm will function properly for large offshore earthquakes and to accommodate the synthetic dataset. We reduce the number of active stations required to trigger from 40% to 5% so that EPIC will trigger for offshore events. The maximum allowed event-to-station distance for event creation and magnitude estimation has also been increased from 200 km to 500 km. These two configuration changes are not recommended for the live ShakeAlert system, however, they were necessary for EPIC to reliably create new events and associate new triggers to trial epicenters when replaying the synthetics. The filter-bank teleseismic filter (Chung *et al.*, 2019), which differentiates between local and teleseismic events, has been turned off. The filter requires 30 s of data prior to an earthquake trigger and the *M* 9 synthetics do not contain enough pre-event data for this feature to work properly. EPIC creates some split events with the *M* 9 scenarios and therefore we also

apply the split event check described in Hartog *et al.* (2016). Although this reduces the number of split events, it does not prevent them all.

We use a new version of FinDer (Andrews *et al.*, 2021; Böse *et al.*, in prep) that is capable of utilizing generic and fault specific templates. The code has been upgraded with a dynamically increasing data window to accommodate large earthquakes and has been configured to select higher PGA thresholds earlier than previous versions to estimate larger magnitudes faster. Trigger checks to remove noisy stations and a latency check that ignores stations that have stopped reporting during an event have also been introduced.

We also use an extended version of the generic symmetric crustal earthquake templates (created with the Cua and Heaton (2009) GMM) that allow rupture lengths to reach 1362 km. McGuire *et al.* (2021) also uses this template set. With the Wells and Coppersmith (1994) crustal magnitude-length scaling relation, this is equivalent to a maximum magnitude of *M* 9. However, we configure FinDer to use the subduction zone magnitude-length scaling relation of Blaser *et al.* (2010) to estimate the magnitude where this rupture length is equivalent to an *M* 9.7. A length of 629 km corresponds to an *M* 9 according to the Blaser *et al.* (2010) relation.

The configuration of the SA algorithm has also been modified to accommodate large offshore earthquakes. To allow FinDer solutions to be associated with offshore EPIC solutions, the designated FinDer alert region has been expanded offshore. The maximum time and location differences between EPIC and FinDer solutions to be associated with an event have been increased from 30 s to 60 s and 100 km to 250 km, respectively. Finally, the SA allows FinDer to alert on its own (the operational ShakeAlert system currently requires an EPIC solution as well).

For this study, we also apply a new contour distance table created with the four Next Generation Attenuation – West 2 (NGA-West2) GMMs (Abrahamson *et al.*, 2014; Boore *et al.*,

2014; Campbell and Bozorgnia, 2014; Chiou and Youngs, 2014). Because of the magnitude limitations of the GMMs, the table only extends to *M* 8.5. EqInfo2GM applies contour distances for an *M* 8.5 to all magnitude estimates above this value.

During the writing of this article, the ShakeAlert project decided not to deploy the NGA-West2 contour distance tables yet because they deteriorated overall performance for low magnitude events. In the PNW, eqInfo2GM will continue to use contour distance tables generated with the Chiou and Youngs (2008) GMM. Because the NGA-West2 GMMs and the Chiou and Youngs (2008) GMM were both developed with crustal earthquakes, neither is ideal for predicting ground motions for offshore interface earthquakes. Therefore, we choose not to rerun the *M* 9 scenarios using the Chiou and Youngs (2008) contour distance tables because we expect little impact on the results.

3.3 MMI threshold station-based and population-based alert classification

We quantitatively assess the quality of EEW alerts using an alert classification scheme similar to Thompson *et al.* (2021). All EEW stations within California, Oregon, Washington, and within the boundaries of the CVM are included in the station-based quality assessment (red dots in **Fig. 4.1**). For each station we create a PGA and PGV time series by taking the vector sum of the horizontal acceleration, or velocity, components at each time step. The velocity time series are created by integrating the acceleration records after they are demeaned, tapered, and high-pass filtered at 0.075 Hz. An MMI time series is then computed from the PGA and PGV time series using equations (6) and (9) from Worden *et al.* (2012). The MMI time series is used to measure the time (relative to earthquake origin time) when particular MMI alert thresholds are first exceeded at each site.

Alerts are classified by comparing the ShakeAlert contour messages generated for each *M* 9 scenario to the MMI alert threshold exceedance times measured at each site. For a particular MMI alert threshold, sites that fall within the boundaries of the MMI contour prior to the observed ground motions exceeding the threshold are classified as true positive (TP). True positive sites with warning times (defined in the following paragraph) less than one second or sites that exceed the threshold before receiving an alert are classified as late alerts (LA). Sites outside of the MMI contour that exceed the threshold are false negatives (FN). Sites within the MMI contour that do not exceed the threshold are false positives (FP). True negative (TN) sites do not receive alerts and do not exceed the threshold. This study focuses on MMI alert thresholds MMI III (MMI 2.5-3.4), MMI IV (MMI 3.5-4.4), and MMI V (MMI 4.5-5.4), which are the thresholds used to define the alerting criteria for the delivery mechanisms that currently issue alerts for the operational ShakeAlert system (McGuire *et al.*, 2021). ShakeAlert outputs alert messages in three formats: source parameters, ground-motion contours and ground-motion maps. We concentrate our assessment on the source parameters and MMI contours since they are used by the operational ShakeAlert system to send alerts to the general public.

For a particular MMI alert threshold, warning time is defined as the difference between the time when threshold level shaking reaches a site and the alert time (time when an alert message is sent out relative to origin time) when that site is alerted for threshold level shaking. As an earthquake rupture grows and ShakeAlert receives more information from stations, magnitude estimates and contour sizes generally increase with successive alert updates. Large earthquake ruptures lasting several minutes may generate several alert updates before more distant sites receive alerts. Warning times in this study do not take into consideration system latencies from data telemetry or alert delivery. **Figure 4.3** shows all the information described

above for a single scenario. It shows the successive ShakeAlert source estimates (stars or lines) of the main event and the associated MMI V alert contours in black and the source estimates and alert contours for two split events in blue and magenta. Split events are further described in the next section. The symbols denote station locations, where the shape of the symbol represents a FN (lighter colored filled circles), FP (squares), LA (darker colored filled circles), TN (diamonds), or TP (triangles) classification using the main event estimates. The color of the triangles denote the amount of warning time. The white star is the actual epicenter and the blue to yellow color gradient shows the slip distribution of the scenario rupture.

For our population-based assessment of alert quality, we compute a Voronoi diagram of the sites used in the station-based assessment for each *M* 9 scenario and MMI alert threshold. Each Voronoi cell is categorized based on the classification of the site within the cell (see **Fig. 4.4**). We overlay each map of categorized Voronoi cells with a 30 arc-second (~1 km) resolution Center for International Earth Science Information Network (CIESIN) and National Aeronautics and Space Administration (NASA) Socioeconomic Data and Applications Center (SEDAC)'s Gridded Population of the World (see Data and Resources). Using raster statistics, we sum the population within the TP, FN, and LA classified Voronoi cells. The population located within California, Oregon, Washington, and within the boundaries of the CVM (**Fig. 4.1**) are included in the population-based assessment. We assume that every person in the population grid has the means of receiving an alert and, if the cell is classified as TP, will receive the same amount of warning time as the site within the cell.

4 RESULTS

4.1 Assessment of ShakeAlert earthquake source parameters

For each of the 30 *M* 9 scenarios, we measure the estimated magnitude errors for each alert update, the first alert epicentral location error, and the timing of first and final alerts. The scenario magnitude grows as the rupture evolves and magnitude error is therefore defined as the difference between the observed *M* 9 scenario magnitude at a specific alert time and the ShakeAlert magnitude estimate at the same alert time. The difference between the *M* 9 scenario magnitude and ShakeAlert magnitude with the first alert range between -0.4 and 4.8 magnitude units (squares in **Fig. 4.5**), with a mean and standard deviation (std) of about 2.1 and 1.1 magnitude units, respectively. On average, it takes about 60 s from origin time (std = 31 s), for the difference to decrease to 0.5 magnitude units or less (triangles in **Fig. 4.5**). By the time the magnitude error reduces to at least 0.5 units, the observed scenario magnitude is greater than *M* 8 for all scenarios. *M* 9 scenario ruptures grow to *M* 8 in about 17 s, on average. For the final alerts, magnitude errors range between 0.0 and 0.6 magnitude units (stars in **Fig. 4.5**). Note that a zero magnitude error only indicates that the *M* 9 scenario magnitude and the ShakeAlert magnitude at the time of the final alert were the same, not that ShakeAlert predicted a final magnitude of *M* 9. All scenario ruptures continue for tens of seconds to minutes after ShakeAlert issues the final alert. The maximum magnitude estimated by ShakeAlert averaged over all scenarios is 8.7. The highest magnitude estimate is *M* 8.9. On average, *M* 9 scenario ruptures grow to *M* 8.9 in 190 s. The range of final alert times is 80 to 430 s (mean = 230 s, std = 92 s).

The FinDer3 algorithm is configured to only retain PGA measurements observed at stations for 180 s because of performance issues observed in the live real-time system when trying to cache a longer time series for each of the thousands of ShakeAlert station channels. It is

possible that we observe final magnitude estimates below *M* 9 using FinDer3 because the algorithm is discarding high threshold PGA measurements while the rupture is still growing.

The location error is the distance between the true epicenter and the epicenter predicted by ShakeAlert at a specific alert time. For most scenarios, initial epicenter estimates have location errors less than 50 km. Only two scenarios with epicenters around 100 km from the coast have location errors between 100-110 km (**Fig. 4.6**). First alert times range from 5 to 41 s (mean = 15 s, std = 6 s). The earliest first alert times coincide with inland hypocenters, but for offshore epicenters, nearness to the coast does not necessarily decrease first alert time.

4.2 Split events

For 17 out of the 30 *M* 9 scenarios, EPIC splits triggers (shaking detections) for a single scenario into multiple events (**Fig. 4.7a**). During an earthquake rupture, triggers at stations must fall within a specified range of *P*-wave arrival times and epicentral distances (black lines in **Fig. 4.7b**) defined in the EPIC algorithm configuration for the triggers to be associated with an existing event. If a trigger cannot be associated with an existing event, EPIC will attempt to create a new event by associating it with other unassociated triggers. When multiple EPIC events are generated during a ShakeAlert run, the SA associates FinDer source estimates with the EPIC event with the smallest origin time and location misfit between the FinDer and EPIC solutions. We define this EPIC event as the main event and label all others as split events. The number of split events generated per scenario ranges between zero and four. In most cases, split events occur after the creation of the main event and generate alerts while the main event is still sending out updates (e.g., **Fig. 4.7c**)**.** There are two *M* 9 scenarios, csz004 and csz020, where EPIC splits the earthquake into two events before FinDer is triggered. In each of these cases the SA associates the FinDer solutions with the later EPIC event. As a result, these scenarios exhibit the

latest first alert times (25 s and 41 s after origin time, respectively). Most split events are created when EPIC triggers on *S*-waves at several stations and associates them as a new event (e.g., **Fig. 4.7e,f**). Five scenarios generate split events when EPIC triggers on artifacts at the end of waveforms. We exclude these from the total count because they would not occur during an actual earthquake. For four out of the 20 remaining split events, it is unclear why the triggers are not associated with the main event: EPIC triggers on *P*-wave arrivals, the triggers meet the event association criteria, and epicenter location estimate is within 50 km of the main event epicenter.

During a real earthquake, split events could potentially generate false alerts that would negatively impact ShakeAlert performance. However, we have decided to exclude the split events from our analysis for three reasons: (1) We are unsure whether EPIC triggers on many *S*-phases due to the nature of the synthetics or whether we can expect EPIC to have trouble with picking *P*-wave first arrivals from real offshore events in general, (2) contours generated by split events generally overlap in space and time with main event contours (e.g., **Fig. 4.3 and 4.7a,c**), and (3) in all cases except two (csz004 and csz020 mentioned above), EPIC predicts magnitudes around *M* 7 and above for split events and point-source magnitude estimates above about *M* 7.5 are unreliable (e.g., Trugman *et al.*, 2019). A new version of the SA algorithm will be deployed to the production ShakeAlert system in the near future that is configured to only accept EPIC events with magnitudes up to *M* 7.5. This could eliminate many of the split events that we observe in our runs since most of the split events based on *S*-wave triggers estimate magnitudes between about *M* 7 and *M* 9.

4.3 Station-based and population-based alert quality

For each scenario and MMI alert threshold, we compute the normalized station-based TP rate (STPR = TP/(TP + FN + LA)), FN rate (SFNR = FN/(TP + FN + LA)), and LA rate (SLAR

= LA/(TP + FN + LA)) using methods modified from Meier (2017) and Cochran *et al.* (2018), where TP, FN, and LA are the number of true positive, false negative, and late alert classified stations, respectively (transparent shapes in **Fig. 4.8**). We do not calculate an FP rate since only three or fewer sites for two *M* 9 scenarios are classified as FP, and only for MMI V. We also calculate the normalized population-based TP rate (PTPR), FN rate (PFNR), and LA rate (PLAR) using the same equations, but substituting the TP, FN, and LA station counts with the population count within the TP, FN, and LA classified Voronoi cells (solid shapes in **Fig. 4.8**). A TP rate value of 1.0 indicates perfect performance.

For an alert threshold of MMI III, the mean STPR is 0.95 and mean PTPR is 0.97. If we define good performance as a TP rate greater than or equal to 0.75 then all scenarios except csz004 perform well at this threshold. Because of csz004's later than average first alert time (41 s), a large region around the epicenter that encompasses Portland, OR and includes 36% of the population in our analysis region receive late alerts for this scenario. There is about a 10% decrease in average alert quality for MMI IV (mean STPR = 0.81, mean PTPR = 0.84), with 73% of scenarios showing good performance in the station-based assessment and 80% performing well in the population-based assessment. For MMI V, the average alert quality drops below our definition of good performance (mean STPR = 0.56, mean PTPR = 0.59) with only 20% of scenarios showing good station-based performance and 37% with good population-based performance. TP rates are higher when taking into account population because most people in the PNW live in urban centers far enough inland from the coast to avoid near-source LA zones (e.g., compare locations of black dots surrounding Seattle and Tacoma to the location of LA zone on the coast of Washington in **Fig. 4.4**).

4.4 Warning times distributed by population

For each MMI alert threshold, we estimate a range of possible warning times for each scenario. By performing a population-based alert quality assessment and assigning the warning times calculated for the sites within the TP classified Voronoi cells to the population within the cells (e.g., **Fig. 4.4**), we are able to explore how warning times are distributed throughout the population in the alerting region (**Fig. 4.9**). Warning times do not simply increase with distance from the earthquake epicenter (e.g., **Fig. 4.3**) due to the complicated evolution of ShakeAlert's source estimates and alerting polygons. For MMI III, most of the population could receive positive warning times with more than half of the alerts received at least 30 s ahead of threshold level shaking. The percentage of the population to receive correct and timely alerts and the range of warning times decreases as the alert threshold is increased. For MMI V, a small majority (~59%) may receive a timely alert, but only ~17% of alerts will be at least 30s ahead of threshold shaking. For all thresholds, there are limited regions where possible warning times may exceed 90s.

5 DISCUSSION

The ShakeAlert system is still under development and optimally configured to alert for shallow crustal earthquakes within the seismic network. We attempt to develop realistic expectations of ShakeAlert performance for offshore megathrust earthquakes by playing a suite of synthetic seismograms from 30 hypothetical *M* 9 scenarios on the CSZ through a test system that is very similar to the production system but incorporates a few recent improvements to FinDer that are soon to be included in production.

Our results show that the majority of the population could receive alerts with positive warning times for an alert threshold of MMI III (**Fig. 4.9**). We also observe an overall reduction

in alert quality and decrease in the range of possible warning times with increased MMI alert threshold (**Fig. 4.8** and **Fig. 4.9**). By surveying the individual scenario outcomes, we determine that decreasing alert quality with increased alert threshold can generally be attributed to three factors: LA zones near earthquake epicenters, LA zones caused by long time intervals between later alert updates, and FN zones at the northern and/ or southern ends of the ruptures.

We observe LA zones near event epicenters for almost all scenarios that tend to increase in size when the MMI alert threshold is increased. On average, first alert magnitude predictions underestimate the observed magnitude of the growing *M* 9 rupture by around two magnitude units and it takes about 60 seconds for the magnitude error to reduce to less than 0.5 units. Underpredicted first alert magnitudes are unsurprising as EPIC typically detects earthquakes before FinDer and first alert estimates are based on a 0.2 s window of *P*-wave amplitude information from a minimum of four stations (Chung *et al.*, 2019). Magnitude is the only parameter used to select the contour radius from the precomputed contour distance tables, therefore, underpredicted magnitudes will result in undersized MMI contours. For higher MMI thresholds, especially MMI V, several alert updates are often generated before the contours begin alerting onshore sites (e.g., **Fig. 4.3**) so it is more likely that people near the epicenter will experience MMI V level shaking before an alert is received.

LA zones are also created by large time gaps between later alert updates. For many scenarios, we begin to see time lags of up to several tens of seconds between alert updates for magnitude estimates around *M* 8 and above. For example, there is an LA zone along the Oregon-California border in **Fig. 4.3** that is caused by a 90 second gap between the second-to-last and final alert updates. Delays in later alerts may be traced to the FinDer algorithm. At this time, the only templates available are designed for characterizing crustal earthquakes. They are generated

using a crustal GMM (Cua and Heaton, 2009) and a simple on-land line source that generates bi-laterally symmetrical templates of predicted ground-motion patterns (Böse *et al.*, 2018). The CSZ is an offshore thrust fault with a curved geometry and since there are very few offshore stations in the ShakeAlert seismic network (**Fig. 4.1**), the observed ground-motion pattern of an *M* 9 megathrust event appears asymmetrical. As the rupture area grows, it becomes more difficult to find a good match between the ground-motion pattern and the crustal templates. FinDer discards matches with low likelihood values and continues to reprocess the data until a satisfactory match can be made, leading to delays in alert updates. In most cases, the MMI III contours rapidly expand during earlier alert updates to include the entire alerting region and are not affected by delays in later alert updates. Since the contours decrease in size with increased alert threshold, we see a greater negative impact on the higher level contours.

For several scenarios, our ShakeAlert runs produce large FN zones at the northern and/ or southern ends of the rupture for alert thresholds MMI IV and V. Poor FinDer fault location estimates are one contributor to large regions of missed alerts. Contours are centered about the FinDer line source. We observe many cases where, for consecutive alert updates, the FinDer line source will increase in length but the centroid remains very near the location of the first finite fault estimate (e.g., **Fig. 4.3**). FinDer also underpredicts the final magnitude for all *M* 9 scenarios. However, since the precomputed contour distance tables used to define the radius of the MMI contours are calculated with crustal GMMs and are only valid up to *M* 8.5 it is more likely that undersized contours for the largest magnitude estimates are contributing to the size of FN zones. A new set of Cascadia fault-specific FinDer templates, currently in development, may improve the timing and accuracy of source characterization for large offshore earthquakes in the PNW.

From the station-based alert classification scheme, we observe that all sites within the alerting region (**Fig. 4.1**) are classified as either TP, LA, or FN for all scenarios and alert thresholds of interest with the exception of three scenarios with three or fewer sites classified as FP or TN for a threshold of MMI V. Our results indicate that it is very possible that the entire alerting region would experience at least MMI V level shaking during an *M* 9 earthquake on the CSZ. We observe poor performance for most scenarios for this alert threshold (mean STPR = 0.56, mean PTPR = 0.59) with LA zones contributing more significantly to reduced alert quality (mean SLAR = 0.28, mean PLAR = 0.25) than FN zones (mean SFNR = mean PFNR = 0.16).

We use a fairly strict definition of warning time in this study that essentially assumes that mitigating actions can no longer be performed once MMI V level shaking begins. Since LA zones have such a significant impact on alert quality, we find it useful to explore a broader definition of warning time that assumes that end-users are still capable of performing actions to reduce seismic risk prior to experiencing MMI VI (strong) or VII (very strong) level shaking. With what we refer to as our strong shaking alert classification scheme, we define three warning time categories: warning time 1 (WT1) uses our original definition, warning time 2 (WT2) is the difference between the time when MMI VI is first felt at a site and the time when an alert for MMI V is received, and warning time 3 (WT3) is the time difference between when MMI VII is felt and an alert is received for MMI V. After classifying sites using our original station-based alert classification method, we reevaluate the warning times at each LA classified site. LA sites with positive WT2 are classified as TP2. LA sites with a zero or negative WT2 and a positive WT3 are classified as TP3. We generally observe a reduction in the size of LA zones near epicenters and from alert time gaps (e.g., compare LA zones in **Fig. 4.3** to **Fig. 4.10**), indicating that even though an alert may not arrive before MMI V shaking is experienced, for some people

it may still arrive before stronger shaking arrives possibly improving the chance that they may take protective action, such as drop, cover, and hold on. We recalculate the station-based and population-based TP rates (TPR = (TP1 + TP2 + TP3) / (TP1 + TP2 + TP3 + FN + LA)) and LA rates ((LAR = LA / (TP1 + TP2 + TP3 + FN + LA)) and compare them to our original quality factors (**Fig. 4.11**). Mean TP rates increase by about 10% (mean STPR = 0.67, mean PTPR = 0.69).

We also evaluate ShakeAlert performance for an alerting strategy where the entire PNW region receives an alert for MMI V level shaking if ShakeAlert detects an earthquake near the coast with a magnitude of at least *M* 8 (hereafter referred to as the *M* 8 alerting strategy). We use our original station-based alert classification scheme to classify sites for consecutive alert updates until at least an *M* 8 is predicted. Then the remaining unclassified sites are classified as TP, LA, or FP based on whether MMI V level shaking is exceeded and the amount of warning time received relative to the alert time of the *M* 8 prediction.

For the *M* 9 scenarios, it takes ShakeAlert an average of about one minute to estimate an *M* 8. We observe that there are no cases where a PNW regional alert is sent out early enough to reduce the size of LA zones near epicenters, however it does eliminate all FN zones and almost all LA zones caused by time gaps between later alert updates (e.g., **Fig. 4.12**), significantly increasing alert quality (mean STPR increased from 0.56 to 0.93 and mean PTPR from 0.59 to 0.97). There is one case where a delay of 67 s between alert updates occurs before ShakeAlert predicts a magnitude of at least *M* 8, producing an LA zone that extends from northern California to southern Washington. Once the general alert is sent out to the entire PNW region, we observe warning times consistently increasing with distance from the epicenter. The maximum warning time increases from about 90 s for MMI V to around five minutes (**Fig. 4.13**).

Note that the average TP rates for the *M* 8 alerting strategy (mean STPR = 0.93, mean PTPR = 0.97) are very similar to the MMI III TP rates (mean STPR = 0.95, mean PTPR = 0.97). Unlike MMI V contours, first alert MMI III contours are often large enough to alert onshore sites, resulting in smaller LA zones and longer warning times near the event epicenter. However, choosing to use a low MMI threshold rather than applying the *M* 8 alerting strategy increases the likelihood of over-alerting in California. For hypocenters between central Oregon and northern California, we observe that MMI III contours can extend into central California where strong shaking is not likely to be felt (Wirth *et al.*, 2020). Also, for the *M* 8 alerting strategy, almost 50% of the population could receive between ~1-5 minutes of warning (**Fig. 4.13**), whereas only 22% of population would receive between ~1-2.5 minutes of warning for MMI III (**Fig. 4.9**).

6 CONCLUSIONS

Our performance evaluation shows that, with a low MMI alert threshold (i.e., MMI III), ShakeAlert could potentially provide timely and correct alerts for an *M* 9 earthquake to the population in the PNW regardless of the where the event begins. Incorporating Cascadia fault-specific templates may improve alert quality for higher alert thresholds by reducing the size of FN and LA zones caused by poor fault location estimates and time gaps in later alert updates. Contour distance tables computed from subduction zone GMMs for magnitudes up to *M* 9 could also increase the coverage of higher alert threshold contours, particularly for the largest magnitude estimates, thereby decreasing the number of late and missed alerts. By reevaluating alert quality using our strong shaking alert classification scheme, we show that our definition of warning time may be overly conservative and that some end-users that do not receive alerts prior to MMI V (moderate) shaking may still receive useful alerts prior to the arrival of MMI VI (strong) or MMI VII (very strong) level shaking.

Our results suggest that until the system can be more optimally configured for large offshore earthquakes, it may be advisable to alert the entire PNW region if an earthquake that exceeds a particular magnitude threshold is detected near the coast. We apply this strategy with a magnitude threshold of *M* 8 to the *M* 9 scenarios and find the mean TP rates to be similar to using an alert threshold of MMI III. However, the percentage of the population to receive long warning times is significantly greater and there is less risk of over-alerting. Because it can take several alert updates for MMI V contours to reach sites on land, the *M* 8 alerting strategy does not eliminate LA zones near earthquake epicenters. Also, we note that this strategy works well with the *M* 9 simulations because almost all sites experience at least MMI V level shaking. It is possible that some past earthquakes on the CSZ, interpreted as *M* 9 events, were actually a series of *M* ~8 earthquakes that ruptured the entire subduction zone over the course of several years or decades (Melgar *et al.*, in review; Petersen *et al.*, 2014). If a rupture on the CSZ were to stop before reaching *M* 9, the *M* 8 alerting strategy could over-alert some people, however, given the paucity of large offshore Cascadia events and the difficulty of correctly characterizing an *M* 9 rupture in near real-time, we believe this possible down-side is preferrable to risking a large number of late and missed alerts in the event of a very large megathrust event.

7 FIGURES

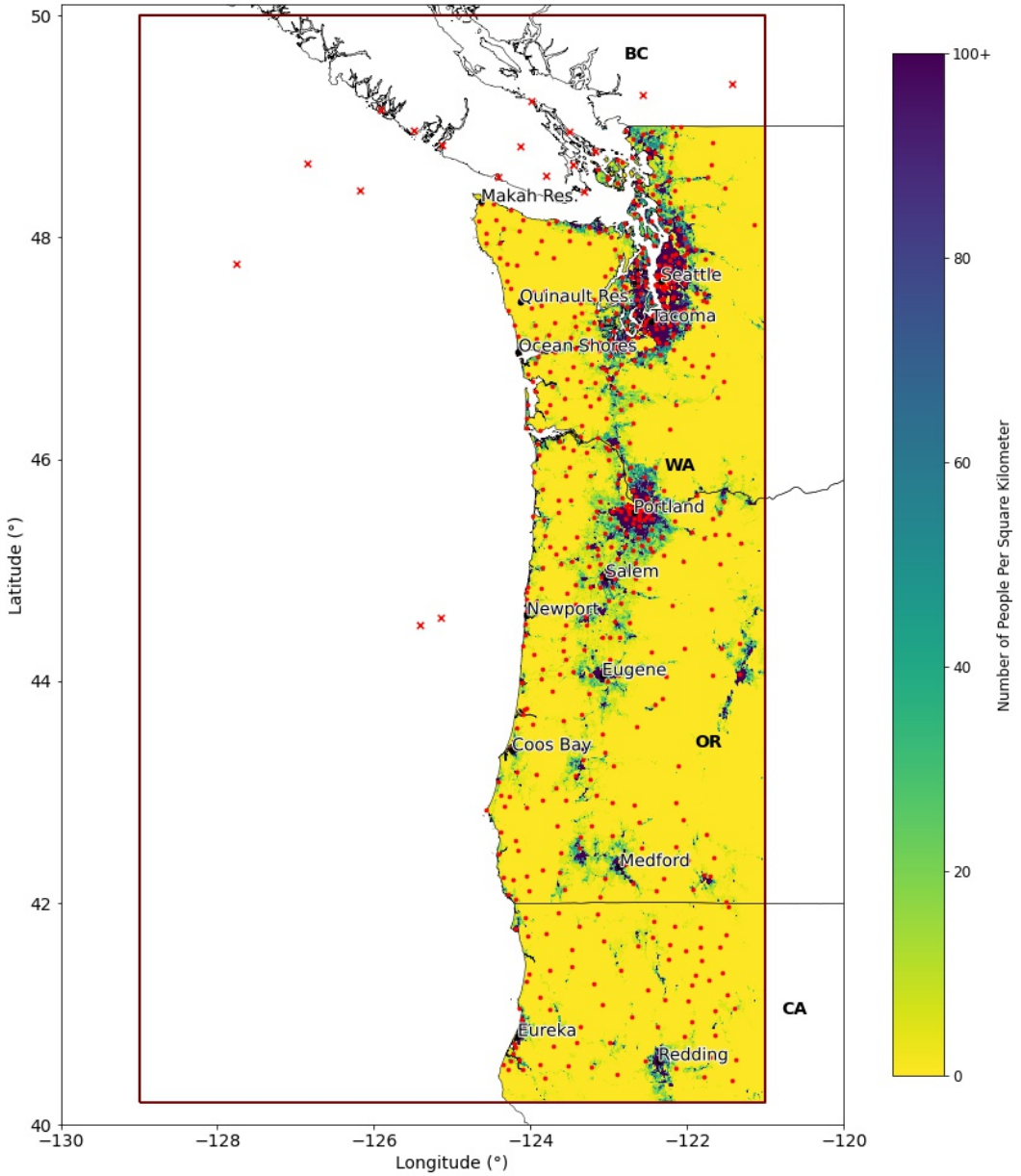

Figure 4.1: Map of ShakeAlert stations (dots and crosses) overlying the portion of a 30 arc-second (~1 km) resolution Center for International Earth Science Information Network and National Aeronautics and Space Administration Socioeconomic Data and Applications Center Gridded Population of the World used in our analysis (colored region of map). Dots are stations within the operational ShakeAlert alerting region and included in our station-based quality assessment. Crosses are stations outside of the United States used only for detecting and characterizing events. Population within the colored region of the map are included in the population-based quality assessment. The boxed region shows the extent of the Cascadia Velocity Model (CVM) used to compute the *M* 9 scenario 3D finite-difference simulations. For our analysis, stations are restricted to the boxed region. The actual ShakeAlert seismic network extends throughout Washington, Oregon, and California. See text for further details. BC, British Columbia, Canada; CA, California; OR, Oregon; Res., reservation; WA, Washington.

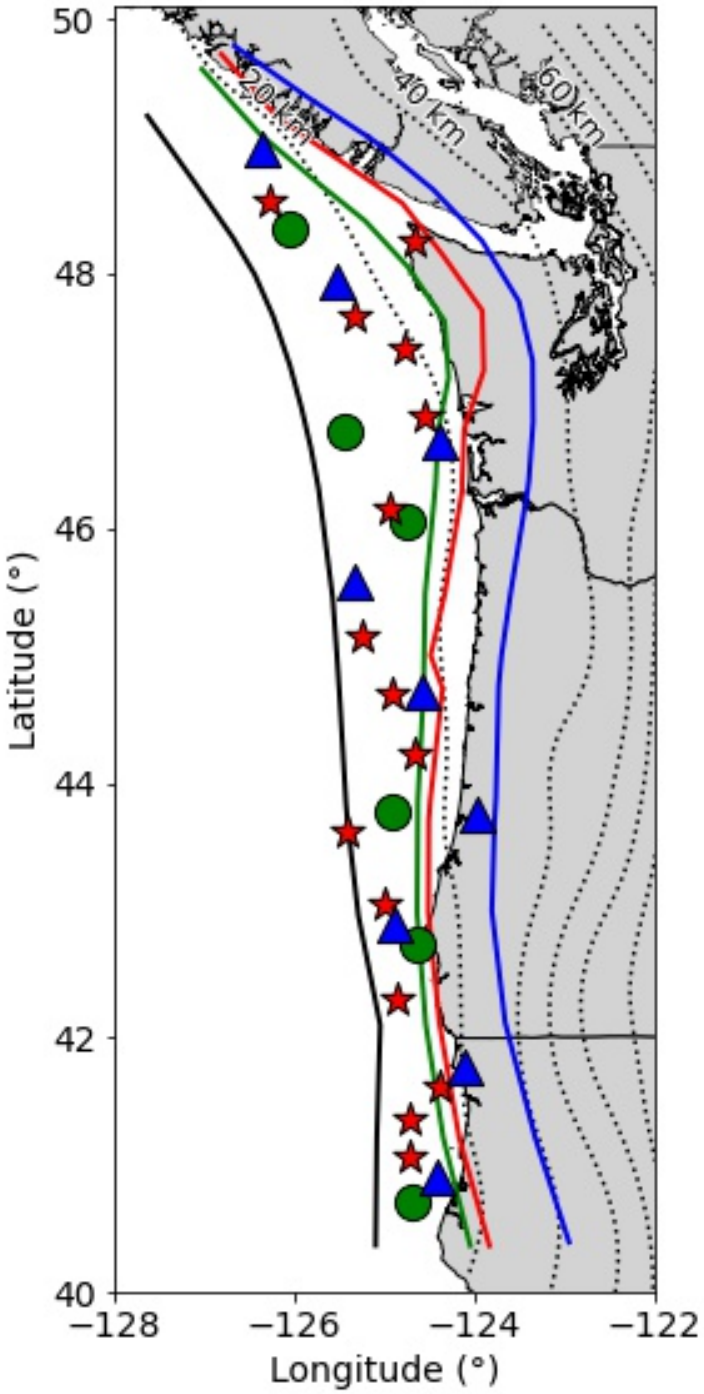

Figure 4.2: Circles, stars, and triangles are hypocenters used in the 30 *M* 9 scenario simulations. The western most solid contour is the up-dip limit of rupture. Additional solid contours are the three options for maximum down-dip rupture extent. Circles are hypocenters for simulations using the westernmost down-dip edge. Stars are hypocenters for the middle down-dip edge. Triangles are hypocenters for the easternmost down-dip edge. Dotted contours are the depth of the Juan de Fuca plate interface from Slab2 (Hayes *et al.*, 2018). Figure is modified from Figure 3 in Frankel *et al.* (2018).

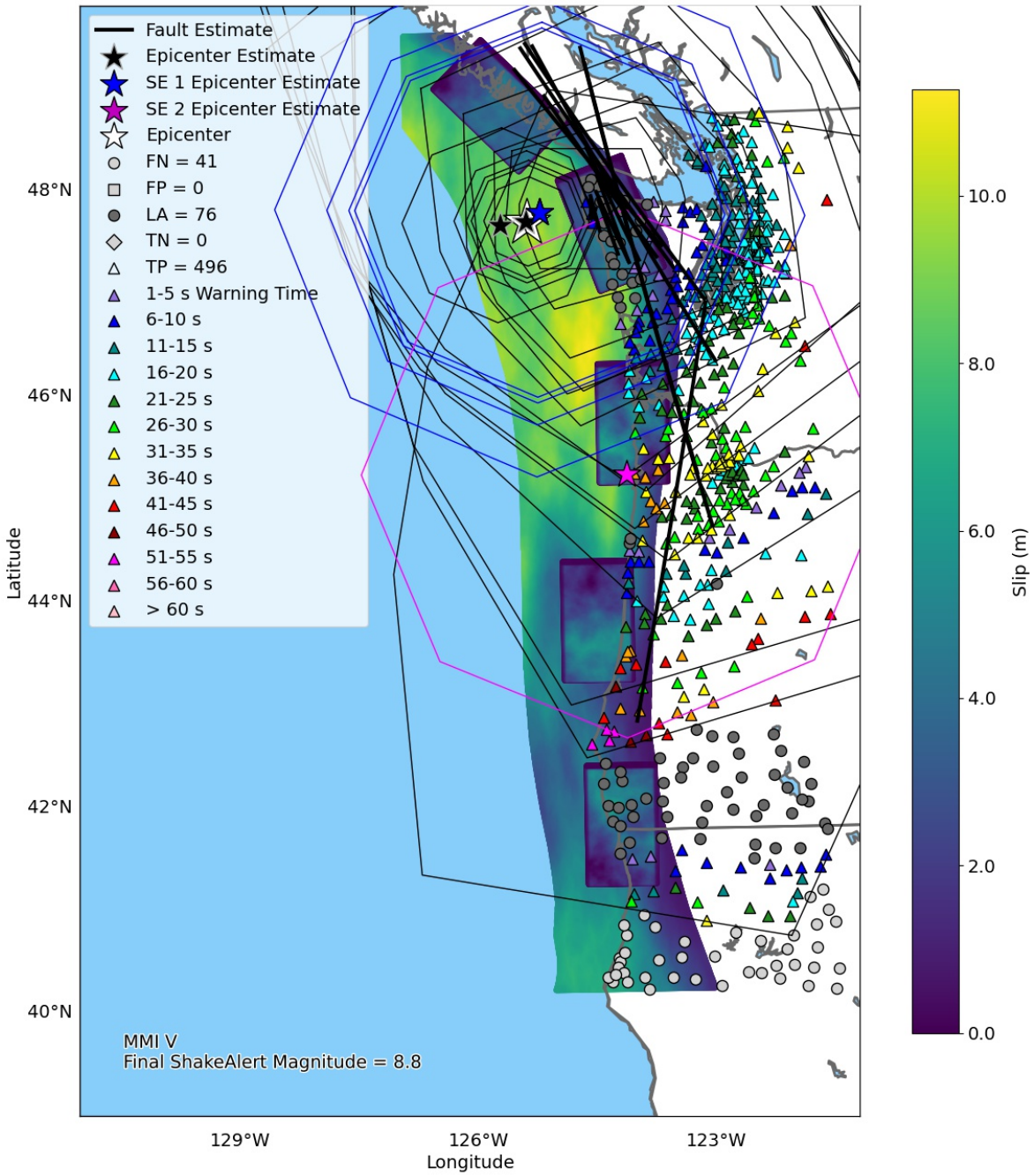

Figure 4.3: Map of the West Coast of the United States showing the ShakeAlert MMI V alert contours for csz003, an *M* 9 scenario that initiates off the coast of Washington. Also displayed are the Solution Aggregator (SA) epicenter and fault estimates associated with each contour update. Note that EPIC splits this scenario into three events: the main event, split event 1, and split event 2. Slip on the Cascadia fault and on five high stress-drop subevents (rectangles) is also shown. The number of stations in each alert classification category for this scenario are listed with the classification symbols in the legend. Stations outside of the alerting region have been excluded from the figure. See text for further details. FP, false positive, FN, false negative; LA, late alert; MMI, modified Mercalli intensity; SE, split event; TN, true negative.

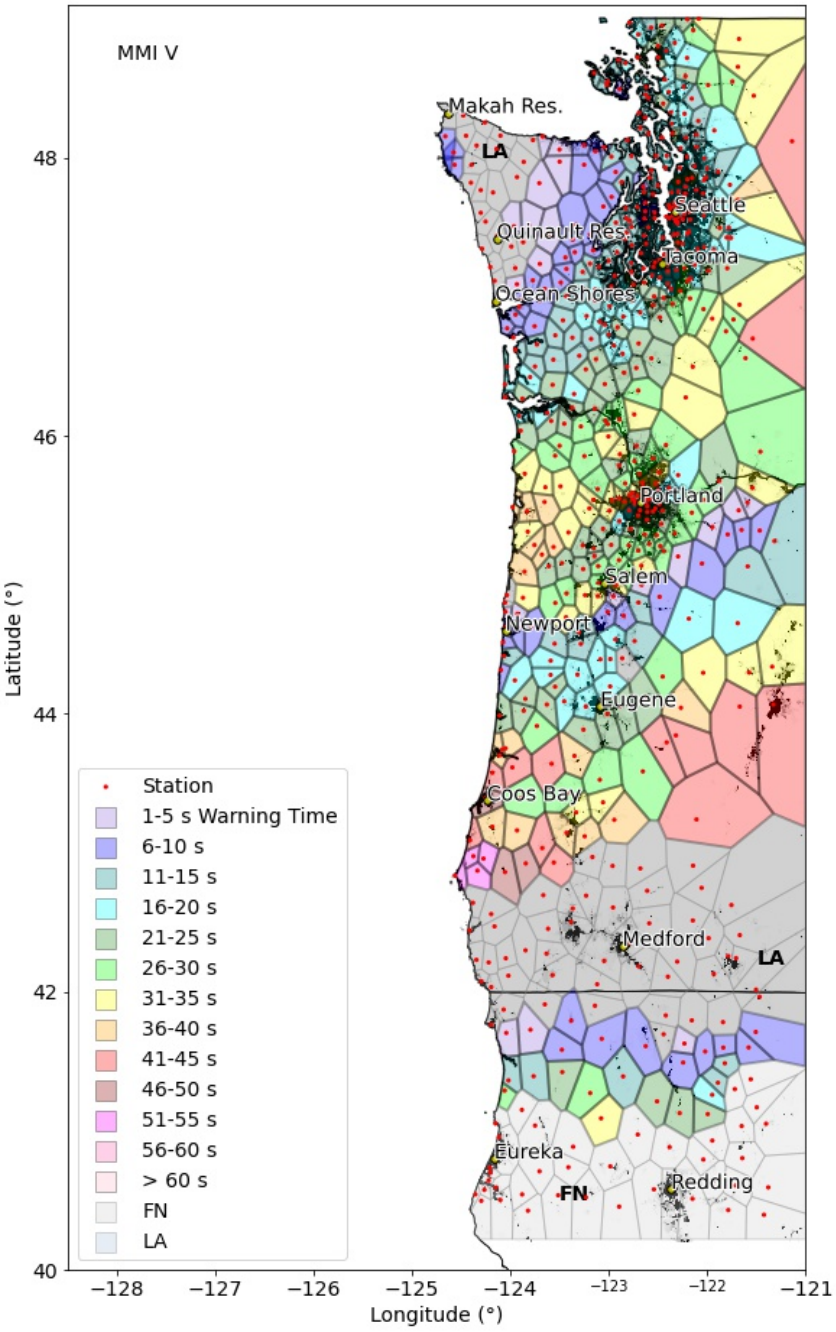

Figure 4.4: Voronoi diagram of the sites used in the station-based quality assessment. The cells are classified according to the MMI V contour results for scenario csz003 in Figure 3. Small black dots mark places where there are at least 100 people per square kilometer. Zones of FN and LA classified Voronoi polygons are labeled. There are no false positive or true negative Voronoi polygons in this example. FN, false negative; FP, false positive; LA, late alert; MMI, modified Mercalli intensity; Res., reservation; TN, true negative.

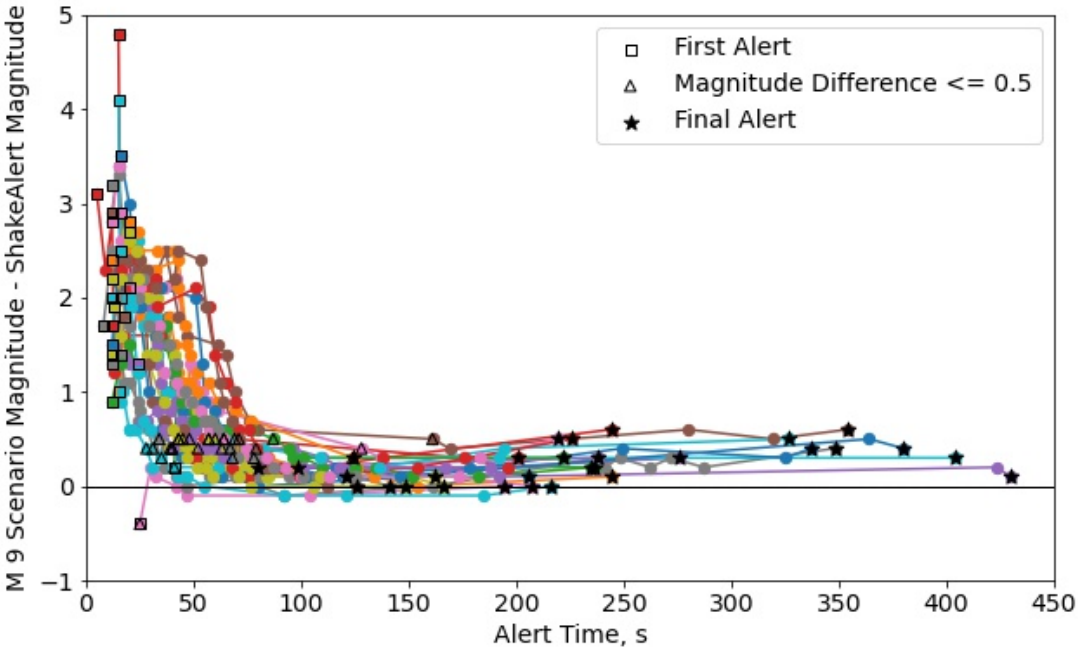

Figure 4.5: Magnitude error versus alert time plot for all *M* 9 scenarios. Each color represents a single scenario. Filled circles represent individual alert messages.

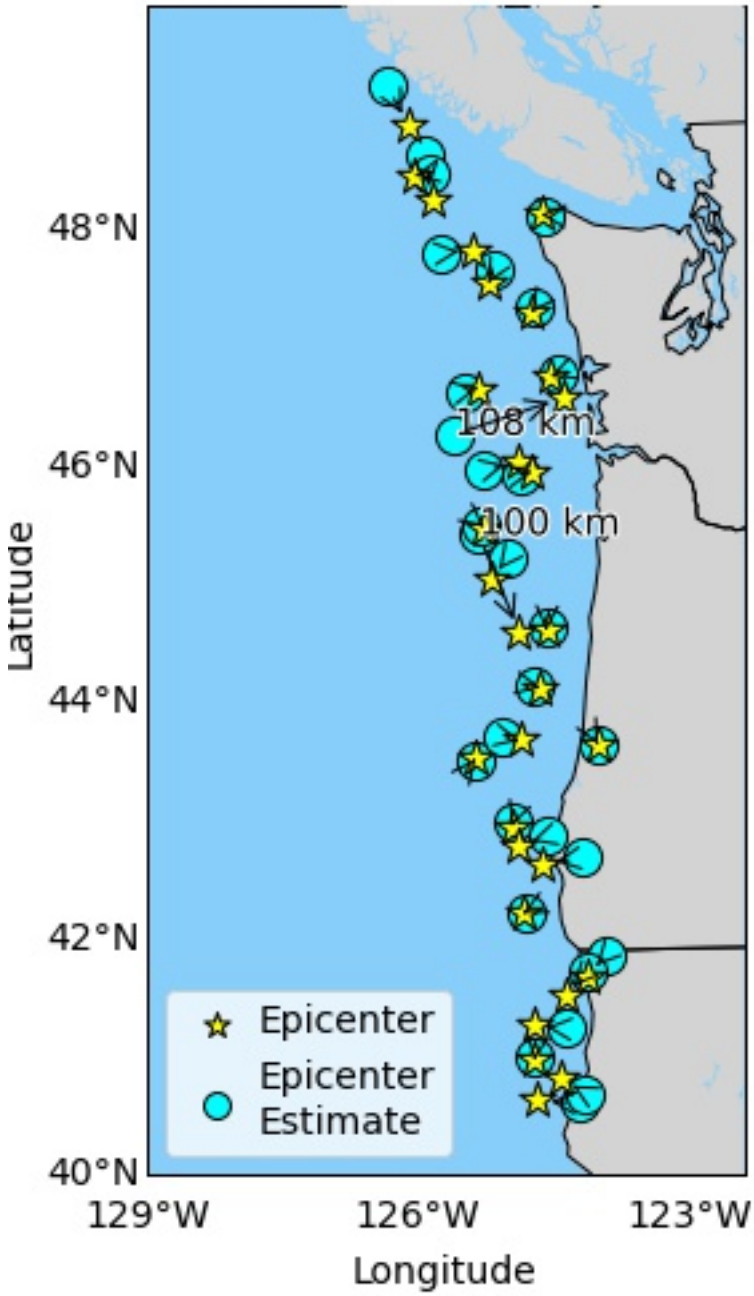

Figure 4.6: Epicenter locations for the 30 *M* 9 scenarios and ShakeAlert first alert epicenter estimates. Location errors that are greater than 50 km are labeled in the figure.

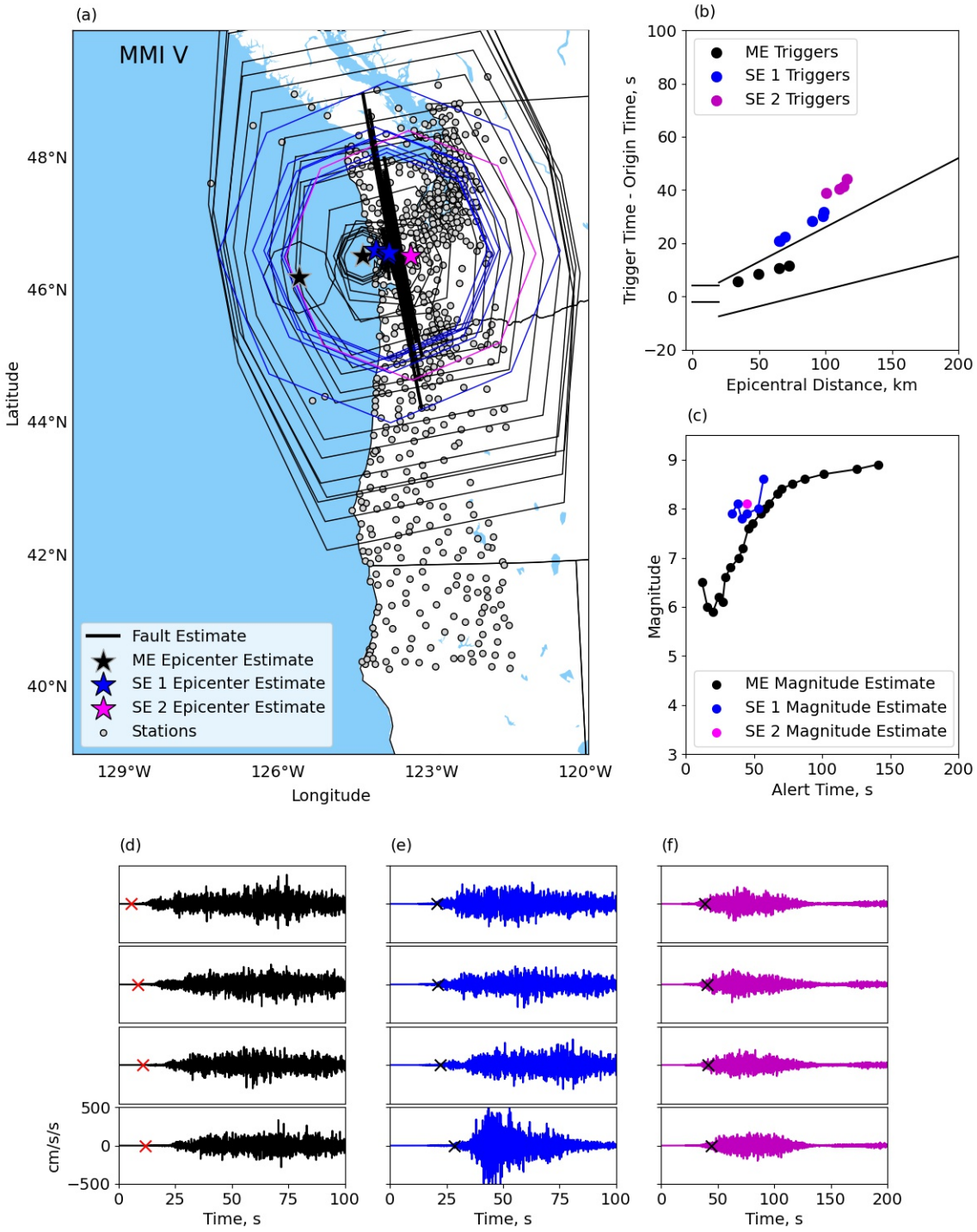

Figure 4.7: (a) Main event and two split event source estimates and MMI V contours generated by ShakeAlert for scenario csz031. **(b)** Triggers associated with the main event and the two split events plotted with the EPIC event association criteria (black lines). **(c)** Estimated magnitude versus alert time plot. **(d**) Waveforms and triggers (red crosses) used to create main event. Waveforms and triggers (black crosses) used to create the **(e)** first split event and **(f)** second split event. ME, main event; MMI, modified Mercalli intensity; SE, split event.

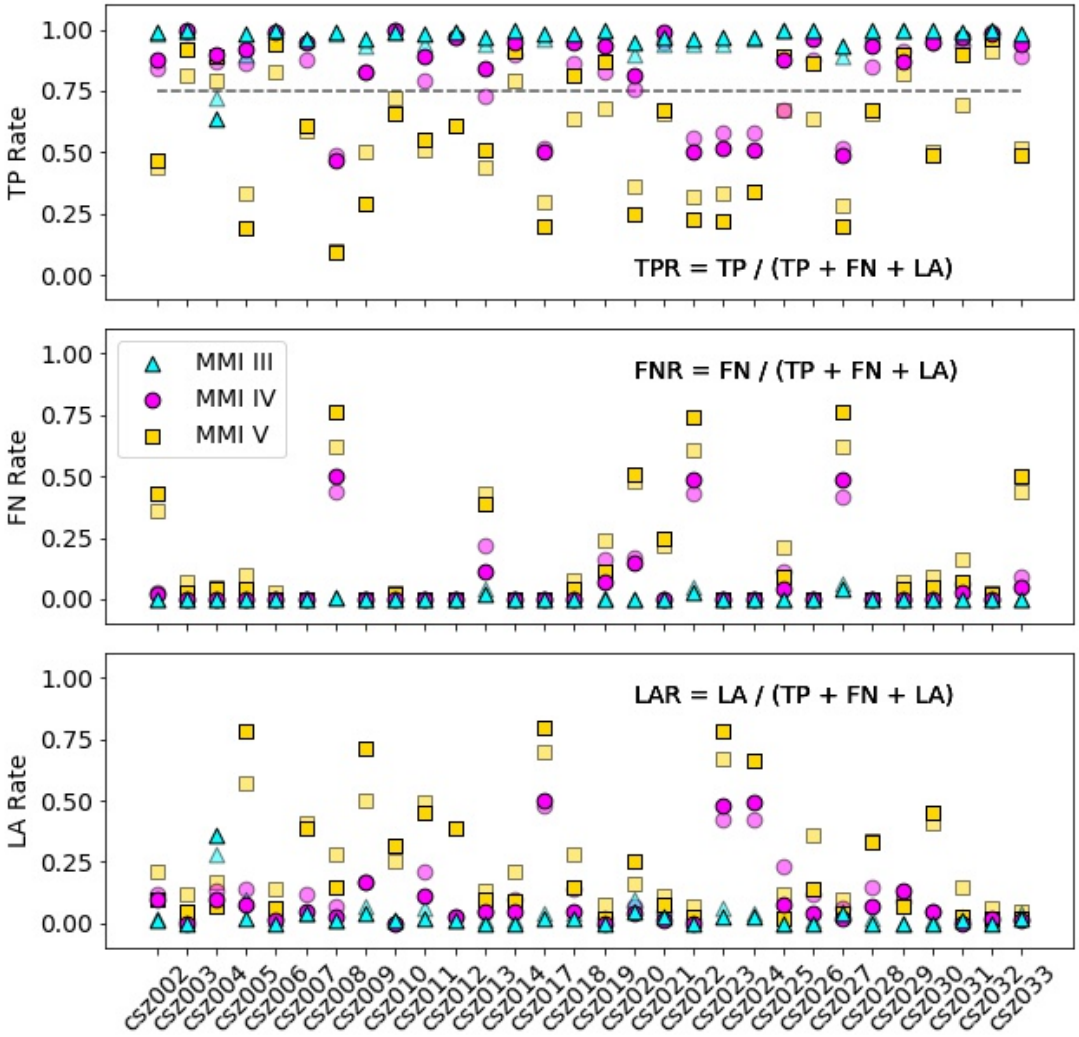

Figure 4.8: Quality factors with respect to MMI alert threshold for each *M* 9 scenario. Solid shapes represent population-based quality factors and transparent shapes represent station-based quality factors. The dashed line marks a TP Rate = 0.75. A TP rate greater than or equal to this value denotes good performance in this study. FN, false negative; FNR, false negative rate; LA, late alert; LAR, late alert rate; MMI, modified Mercalli intensity; TP, true positive; TPR, true positive rate.

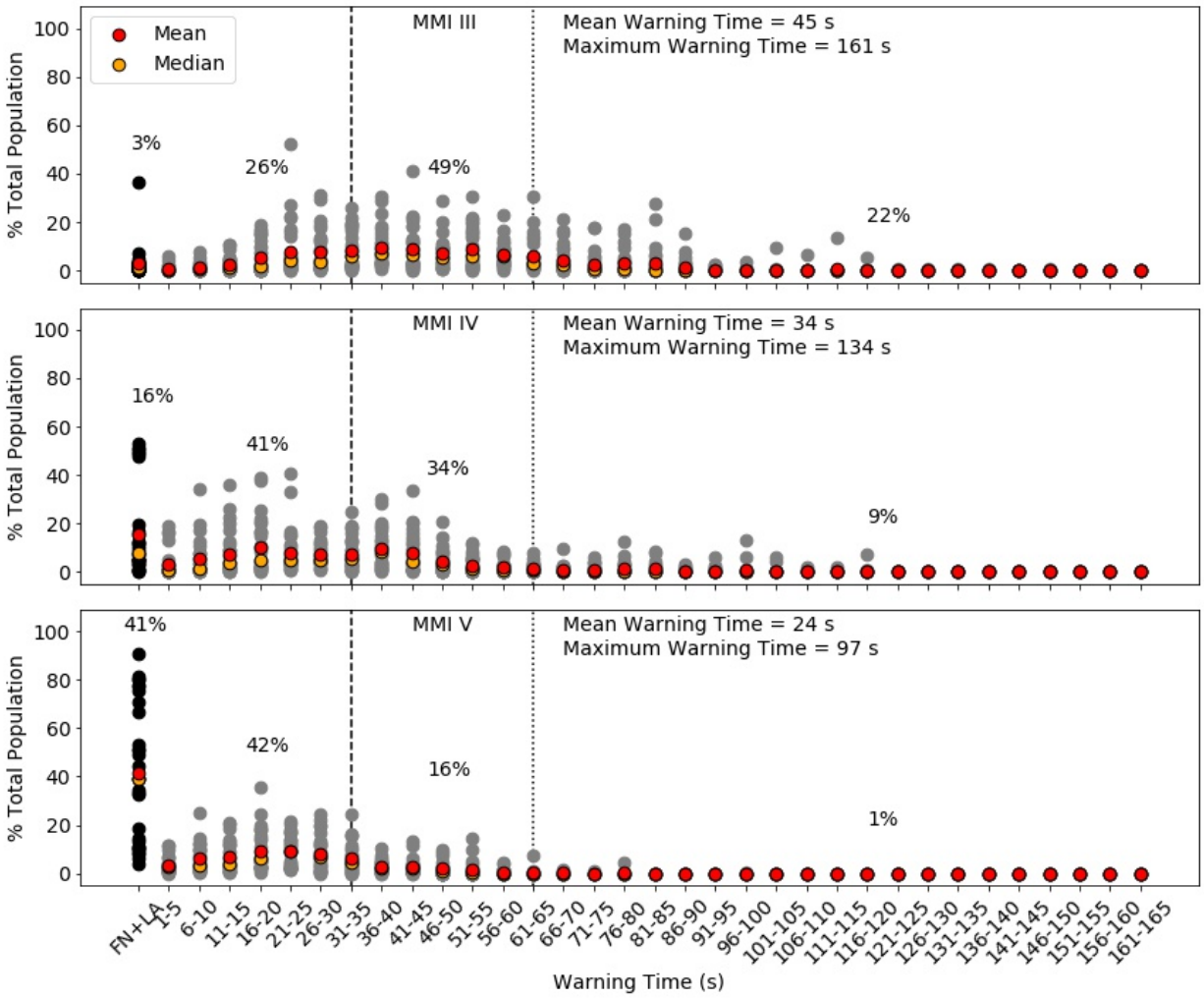

Figure 4.9: For each *M* 9 scenario, percentages of the total population binned by warning time (gray circles) for **(top)** MMI III, **(middle)** MMI IV, and **(bottom)** MMI V. Warning times are binned in five second intervals. Black circles are the percentage of the population in the LA and FN zones. Values above black dots are the mean percentage of the population in the LA and FN zones. Mean percentage of the population that will receive 1-30 s of warning is shown left of dashed line, 31-60 s of warning is between the dashed and dotted line, and greater than 60 s of warning is right of dotted line.

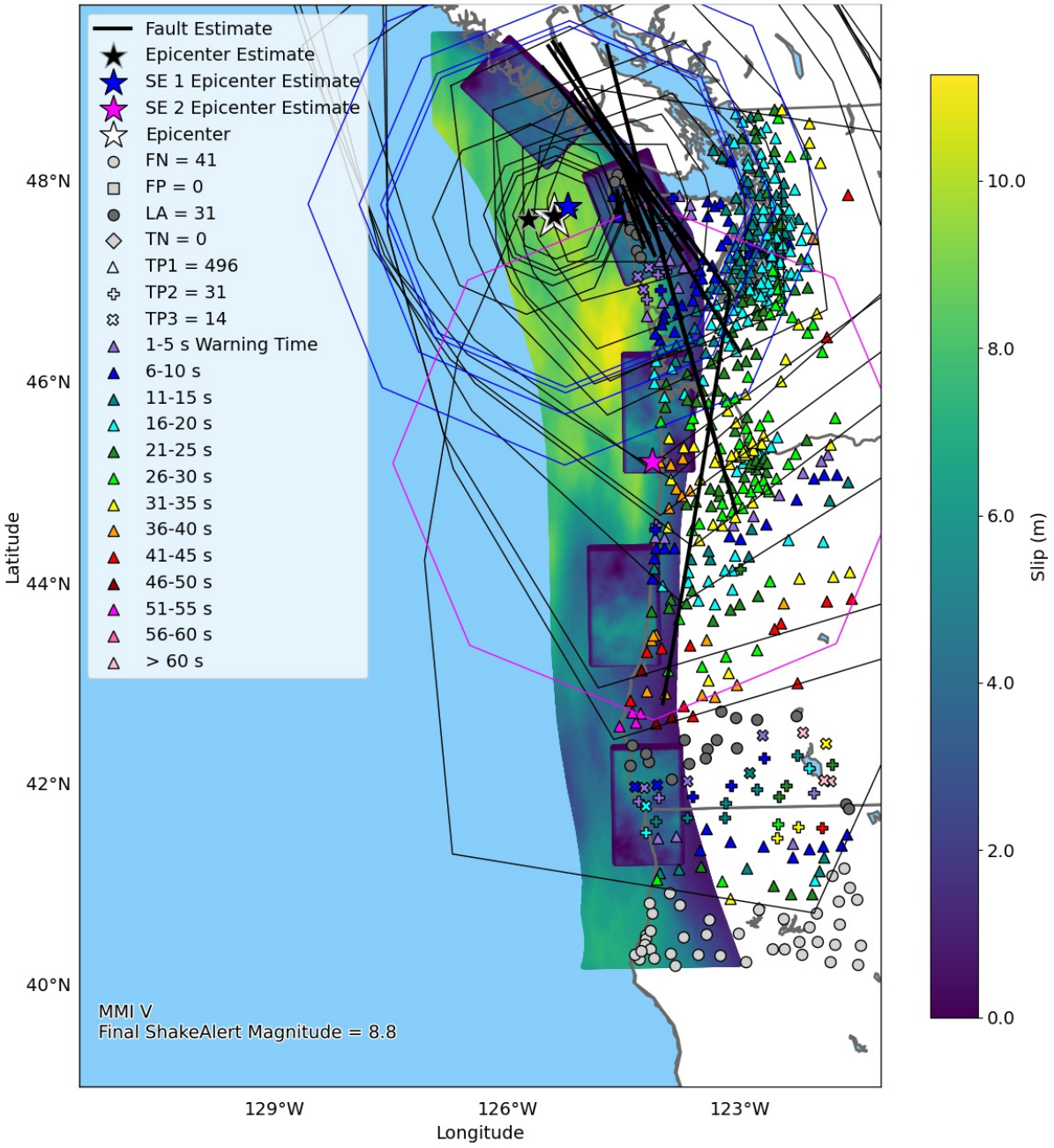

Figure 4.10: The same map as shown in Figure 3 with LA sites reclassified using a strong shaking alert classification scheme. Note that 45 sites originally classified as LA near the earthquake epicenter and along the Oregon-California border in Figure 3 are reclassified as TP2 and TP3. Stations outside of the alerting region have been excluded from the figure. FN, false negative; FP, false positive; LA, late alert; MMI, modified Mercalli intensity; SE, split event; TN, true negative.

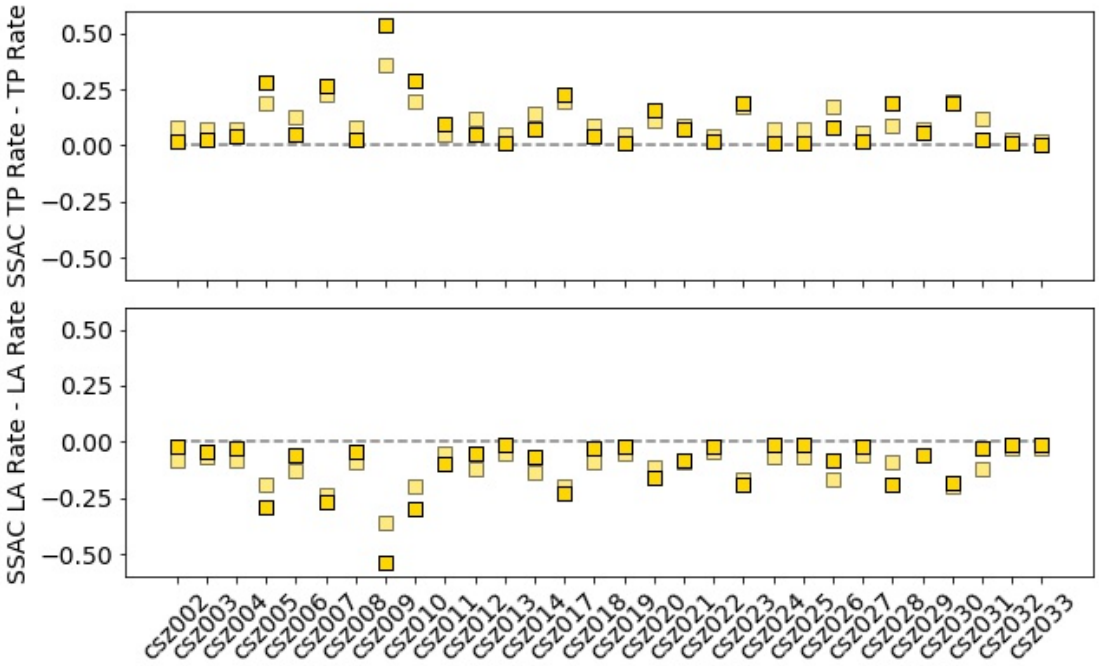

Figure 4.11: For each scenario, the difference between **(top)** the strong shaking alert classification (SSAC) TP rate and the original MMI V TP rate and **(bottom)** the SSAC LA rate and the original MMI V LA rate. Solid shapes are population-based results and transparent shapes are station-based results. LA, late alert; SSAC, strong shaking alert classification; TP, true positive.

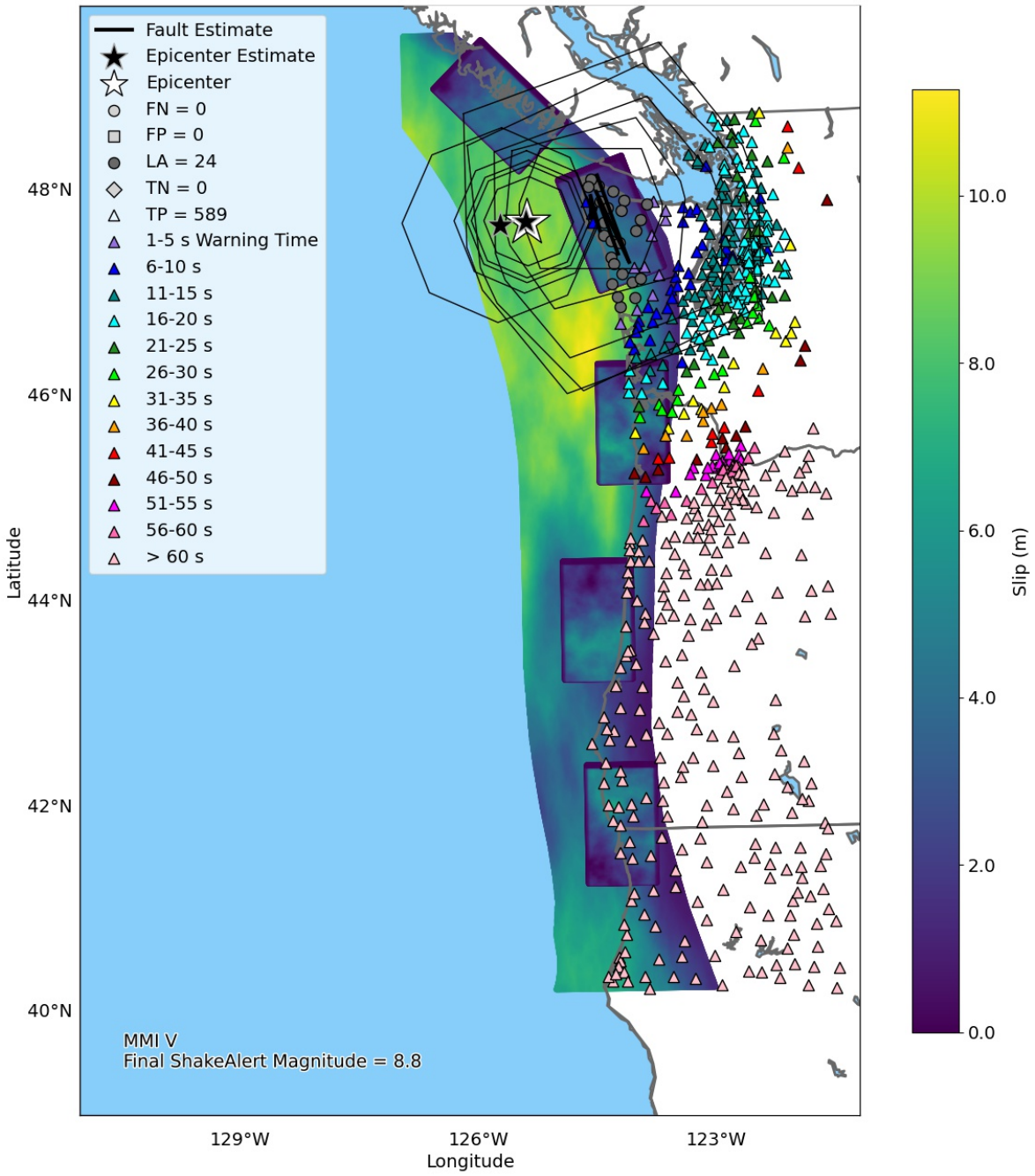

Figure 12: The same map as shown in Figure 3 with sites classified using the original station-based alert classification scheme for an alerting strategy where the entire PNW region receives an alert for MMI V when ShakeAlert estimates an *M* 8 near the coast. Only source estimates and contours for magnitude estimates below *M* 8 are shown. Stations outside of the alerting region have been excluded from the figure. FN, false negative; FP, false positive; LA, late alert; MMI, modified Mercalli intensity; TN, true negative.

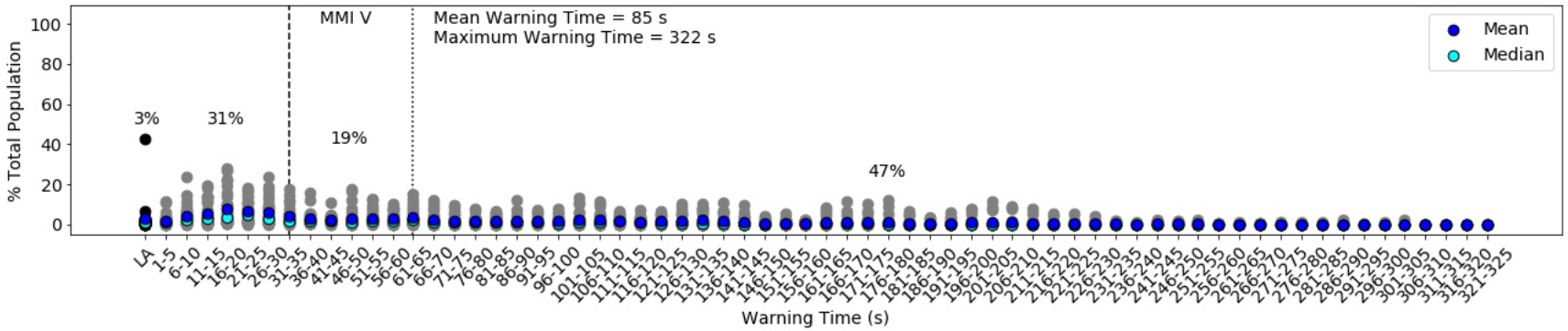

Figure 4.13: For each *M* 9 scenario, percentages of the total population are binned by warning time (gray circles) for an alerting strategy where the entire PNW region receives an alert for MMI V when ShakeAlert estimates an *M* 8 near the coast. Warning times are binned in five second intervals. Black circles are the percentage of the population in the LA zones. Values above black dots are the mean percentage of the population in the LA zones. Mean percentage of the population that will receive 1-30 s of warning is shown left of the dashed line, 31-60 s of warning is between the dashed and dotted line, and greater than 60 s of warning is right of the dotted line. MMI, modified Mercalli intensity.

8 DATA AND RESOURCES

Synthetic broadband seismograms for the 30 hypothetical *M* 9 megathrust earthquake scenarios on the CSZ are available from Design Safe at https://www.designsafe-ci.org/data/browser/public/designsafe.storage.published//PRJ-1355. We developed additional synthetics for existing and planned ShakeAlert station locations and have provided the Earthworm (http://www.earthwormcentral.org/) tankplayer files to the ShakeAlert System Performance and Testing Working group. 30 arc-second resolution population count is the year 2020 estimate from the Center for International Earth Science Information Network (CIESIN) and National Aeronautics and Space Administration (NASA) Socioeconomic Data and Applications Center (SEDAC)'s Gridded Population of the World, Version 4 (GPWv4), available from https://sedac.ciesin.columbia.edu/data/set/gpw-v4-population-count-rev11 (last accessed July 6, 2021).

9 REFERENCES

Abrahamson, N. A., W. J. Silva, and R. Kamai (2014). Summary of the ASK14 ground motion relation for active crustal regions, *Earthq. Spectra* **30**, no. 3, 1025–1055, doi: 10.1193/070913EQS198M.

Andrews, J. R., M. Böse, and J. R. Hartog (2021, December). The Finite-Fault Rupture Detector (FinDer): Enhancing rupture determination for the largest earthquakes. In *AGU Fall Meeting 2021*. AGU.

Atwater, B. F. (1987). Evidence for great Holocene earthquakes along the outer coast of Washington State, *Science* **236**, 942–944.

Blaser, L., F. Kruger, M. Ohrnberger, and F. Scherbaum (2010). Scaling relations of earthquake source parameter estimates with special focus on subduction environment, *Bull. Seismol. Soc. Am.* **100**, no. 6, 2914–2926, doi: 10.1785/0120100111.

Boore, D. M. (1983). Stochastic simulation of high-frequency ground motions based on seismological models of the radiated spectra, *Bull. Seismol. Soc. Am.* **73**, 1865–1894.

Boore, D. M. (1996). SMSIM-Fortran programs for simulating ground motions from earthquakes: Version 1.0, *U.S. Geol. Surv. Open-File Rept. 96-80-A*, 73 pp.

Boore, D. M., J. P. Stewart, E. Seyhan, and G. M. Atkinson (2014). NGA-West2 equations for predicting PGA, PGV, and 5% damped PSA for shallow crustal earthquakes, *Earthq. Spectra* **30**, no. 3, 1057–1085, doi: 10.1193/070113EQS184M.

Böse, M., D. E. Smith, C. Felizardo, M.-A. Meier, T. H. Heaton, and J. F. Clinton (2018). FinDer v.2: Improved real-time ground-motion predictions for M2–M9 with seismic finite-source characterization, *Geophys. J. Int*. **212**, no. 1, 725–742, doi: 10.1093/gji/ggx430.

Böse, M., J. Andrews, J. R. Hartog, and C. Felizardo (in prep). U.S. west coast ShakeAlert warning system: Development and performance of Finite-Fault Rupture Detector (FinDer) v.3.

Campbell, K. W., and Y. Bozorgnia (2014). NGA-West2 ground motion model for the average horizontal components of PGA, PGV, and 5% damped linear acceleration response spectra, *Earthq. Spectra* **30**, no. 3, 1087–1115, doi: 10.1193/062913EQS175M.

Chiou, B.-J., and R. R. Youngs (2008). An NGA model for the average horizontal component of peak ground motion and response spectra, *Earthq. Spectra* **24**, no. 1, 173–215, doi: 10.1193/1.2894832.

Chiou, B. S.-J., and R. R. Youngs (2014). Update of the Chiou and Youngs NGA model for the average horizontal component of peak ground motion and response spectra, *Earthq. Spectra* **30**, no. 3, 1117–1153, doi: 10.1193/072813EQS219M.

Chung, A. I., I. Henson, and R. M. Allen (2019). Optimizing earthquake early warning performance: ElarmS-3, *Seismol. Res. Lett.* **90**, no. 2A, 727–743, doi: 10.1785/0220180192.

Chung, A. I., M.-A. Meier, J. Andrews, M. Böse, B. W. Crowell, J. J. McGuire, and D. E. Smith (2020). ShakeAlert earthquake early warning system performance during the 2019 Ridgecrest earthquake sequence, *Bull. Seismol. Soc. Am.* **110**, no. 4, 1904–1923, doi: 10.1785/0120200032.

Cochran, E. S., M. D. Kohler, D. D. Given, S. Guiwits, J. Andrews, M. Meier, M. Ahmad, I. Henson, R. Hartog, and D. Smith (2018). Earthquake early warning ShakeAlert system: Testing and certification platform, *Seismol. Res. Lett.* **89**, no. 1, 108–117, doi: 10.1785/0220170138.

Cua, G.B., and T. H. Heaton (2009). Characterizing average properties of southern California ground motion amplitudes and envelopes, Earthquake Engineering Research Laboratory, Pasadena, CA, available at http://resolver.caltech.edu/CaltechEERL:EERL-2009-05 (last accessed November 2018).

Frankel, A., E. Wirth, N. Marafi, J. Vidale, and W. Stephenson (2018). Broadband synthetic seismograms for magnitude 9 earthquakes on the Cascadia megathrust based on 3D simulations and stochastic synthetics, part 1: Methodology and overall results, *Bull. Seismol. Soc. Am.* **108**, no. 5A, 2347–2369, doi: 10.1785/0120180034.

Goldfinger, C., C. H. Nelson, A. E. Morey, J. R. Johnson, E. Karabanov, J. Gutierrez-Pastor, A. T. Eriksson, E. Gracia, G. Dunhill, *et al.* (2012). Turbidite event history—Methods and implications for Holocene paleoseismology of the Cascadia subduction zone, *U.S. Geol. Surv. Profess. Pap. 1661-F*, 170 pp.

Hartog, J. R., V. C. Kress, S. D. Malone, P. Bodin, J. E. Vidale, and B. W. Crowell (2016). Earthquake early warning: ShakeAlert in the Pacific Northwest, *Bull. Seismol. Soc. Am.* **106**, no. 4, 1875–1886, doi: 10.1785/0120150261.

Kuyuk, H. S., and R. M. Allen (2013). A global approach to provide magnitude estimates for earthquake early warning alerts, *Geophys. Res. Lett.* **40**, no. 24, 6329–6333, doi: 10.1002/2013GL058580.

Liu, P.-C., and R. J. Archuleta (2002). The Effect of a low-velocity surface layer on simulated ground motion, *Seismol. Res. Lett.* **73**, no. 2, doi: 10.1785/gssrl.73.2.195.

McGuire, J. J., D. E. Smith, A. D. Frankel, E. A. Wirth, S. K. McBride, and R. M. de Groot (2021). Expected warning times from the ShakeAlert earthquake early warning system for earthquakes in the Pacific Northwest, *U.S. Geol. Surv. Open-File Rept. 2021-1026*, 37 pp.

Meier, M. A. (2017). How "good" are real-time ground motion predictions from earthquake early warning systems? *J. Geophys. Res.* **122**, no. 7, 5561–5577, doi: 10.1002/2017JB014025.

Meier, M., Y. Kodera, M. Böse, A. Chung, M. Hoshiba, E. Cochran, S. Minson, E. Hauksson, and T. Heaton (2020). How often can earthquake early warning systems alert sites with high-intensity ground motion? *J. Geophys. Res.* **125**, no. 2, doi: 10.1029/2019JB017718.

Melgar, D. (in review). Was the January 26th, 1700 Cascadia earthquake part of an event sequence? Available at https://doi.org/10.31223/X5XG78 (last accessed March 2022).

Minson, S. E., J. K. Saunders, J. J. Bunn, E. S. Cochran, A. S. Baltay, D. L. Kilb, M. Hoshiba, and Y. Kodera (2020). Real-Time performance of the PLUM earthquake early warning method during the 2019 M 6.4 and 7.1 Ridgecrest, California, earthquakes, *Bull. Seismol. Soc. of Am.* **110**, no. 4, 1887–1903, doi: 10.1785/0120200021.

Petersen, M. D., M. P. Moschetti, P. M. Powers, C. S. Mueller, K. M. Haller, A. D. Frankel, Y. Zeng, S. Rezaeian, S. C. Harmsen, O. S. Boyd, *et al.* (2014). Documentation for the 2014 update of the United States national seismic hazard maps, *U.S. Geol. Surv. Open-File Rept. 2014-1091*, 243 pp., doi: 10.3133/ofr20141091.

Satake, K., K. Wang, and B. F. Atwater (2003). Fault slip and seismic moment of the 1700 Cascadia earthquake inferred from Japanese tsunami descriptions, *J. Geophys. Res.* **108**, no. B11, 2535, doi: 10.1029/2003JB002521.

Stephenson, W. J., N. G. Reitman, and S. J. Angster (2017). P- and S- wave velocity models incorporating the Cascadia subduction zone for 3D earthquake ground motion simulations, update for OFR 2007-1348, *U.S. Geol. Surv. Open-File Rept. 2017-1152*, 17 pp., doi: 10.3133/ofr20171152.

Saunders, J. K., E. S. Cochran, S. E. Minson, J. Bunn, A. Baltay, D. L. Kilb, and C. O'Rourke (2021, December). Population-based earthquake early warning alert performance comparison of PLUM with ShakeAlert. In *AGU Fall Meeting 2021.* AGU.

Thakoor, K., J. Andrews, E. Hauksson, and T. Heaton (2019). From earthquake source parameters to ground-motion warnings near you: The ShakeAlert earthquake information to ground-motion (eqInfo2GM) method*, Seismol. Res. Lett.* **90**, no. 3, 1243–1257, doi: 10.1785/0220180245.

Thompson, M., J. R. Hartog, and E. A. Wirth (2021). Effect of fixing earthquake depth in ShakeAlert algorithms on performance for intraslab earthquakes, *Seismol. Res. Lett*. **93**, 277–287, doi: 10.1785/0220210056.

Trugman, D. T., M. T. Page, S. E. Minson, and E. S. Cochran (2019). Peak ground displacement saturates exactly when expected: Implications for earthquake early warning, *J. Geophys. Res.* **124**, no. 5, 4642–4653, doi: 10.1029/2018JB017093.

Wells, D. L., and K. J. Coppersmith (1994). New empirical relationships among magnitude, rupture length, rupture width, rupture area, and surface displacement, *Bull. Seismol. Soc. Am.* **84**, 974–1002.

Wirth, E. A., A. D. Frankel, N. Marafi, J. E. Vidale, and W. J. Stephenson (2018). Broadband synthetic seismograms for magnitude 9 earthquakes on the Cascadia megathrust based on 3D simulations and stochastic synthetics, part 2: Rupture parameters and variability, *Bull. Seismol. Soc. Am.* **108**, 2370–2388, doi: 10.1785/ 0120180029.

Wirth, E. A., A. Grant, N. A. Marafi, and A. D. Frankel (2020). Ensemble ShakeMaps for magnitude 9 earthquakes on the Cascadia subduction zone, *Seismol. Res. Lett.* **92**, 199–211, doi: 10.1785/0220200240.

Worden, C. B., M. C. Gerstenberger, D. A. Rhoades, and D. J. Wald (2012). Probabilistic relationships between ground-motion parameters and modified Mercalli intensity in California, *Bull. Seismol. Soc. Am*. **102**, no. 1, 204–221, doi: 10.1785/0120110156.

V Summary and future work

In this dissertation, we sought to inform earthquake risk mitigation efforts in the Pacific Northwest (PNW) by characterizing sedimentary basin effects in the Seattle and Tacoma basins and evaluating the performance of an earthquake early warning (EEW) system for the West Coast of the United States for intraslab and megathrust earthquakes.

In Chapter 2, we characterized and measured seismic wave amplification in the Seattle and Tacoma basins using a dataset of local small-to-moderate magnitude crustal and intraslab earthquakes. We also validated a 3D seismic velocity model of the Cascadia subduction zone (CSZ) by computing ground-motion simulations of the earthquakes in our dataset and comparing the synthetic waveforms to the actual strong-motion records. We observed amplification in the Seattle basin for all earthquakes and for a subset of earthquakes in the Tacoma basin. A shallow crustal earthquake southwest of the Seattle basin produced the largest amplification factors suggesting that future shallow crustal events rupturing west of the Puget Lowland and megathrust events on the CSZ will produce greater amplification in the Seattle basin than intraslab earthquakes. We also observed basin-edge generated surface waves at sites in the Seattle basin for most ray paths that cross the Seattle fault zone and possible basin-edge effects recorded at one station in the Tacoma basin for a single event with ray paths crossing the Olympia structure. Ground-motion simulations reproduce shear-wave amplitudes and basin-edge effects well in the Seattle basin. Amplification and basin-edge effects were less well resolved in the Tacoma basin since it is not well characterized in the 3D seismic velocity model.

This study shows that further investigation of the amplification effects of the Tacoma basin would expand our knowledge of seismic hazards in the Puget Lowland region. Since about 2018, station coverage has significantly improved within and surrounding the Tacoma basin.

Surveying recent strong-motion records of local earthquakes could provide further insight into whether the Olympia structure or the Tacoma fault zone can generate basin-edge surface waves. There have been very few earthquakes greater than *M* 3.8 in the Puget Lowland region since this study was conducted, but recordings of teleseismic events (e.g., the 2021 *M* 8.2 Alaska earthquake) could also be used to measure amplification in the basin.

In Chapter 3, we investigate whether applying a simplifying assumption to ShakeAlert algorithms (i.e., fixing all earthquakes at a depth of 8 km) negatively impacts alert quality for intraslab earthquakes in the PNW. We play a dataset of PNW and Chilean intraslab earthquakes twice through ShakeAlert: once using a fixed depth of 8 km for all events and a second time using the catalog depth of each event. By comparing the outcomes, we measure the magnitude, location, and ground-motion prediction errors produced by a shallow depth assumption. We observe that replays of events using a fixed shallow depth are more likely to produce errors in location estimates greater than 50 km when the earthquake is located outside of a seismic network, but that location estimates are similar between shallow and catalog depth replays for events located within a network. For low modified Mercalli intensity (MMI) alert thresholds (i.e., MMI III and IV), our results show that applying catalog depth does not improve the accuracy of magnitude estimates or MMI alert threshold contours. We also do not see an improvement in warning times.

The next useful step in the study would be to explore whether higher MMI alert threshold contours are more sensitive to earthquake depth. Our study was limited to low alert thresholds because some of the smaller magnitude events in our dataset did not produce shaking intensities above MMI IV. Insights may be gleaned from an investigation of moderate-to-large magnitude Japanese intraslab earthquakes. Japan has uniform dense seismic station coverage that may

capture differences in ground motion patterns produced by intraslab events and predicted ground shaking extent assuming shallow depth that we did not observe in the PNW and Chile.

In Chapter 4, we evaluate ShakeAlert's ability to produce timely and accurate alerts for *M* 9 earthquakes on the CSZ by playing a suite of hypothetical *M* 9 scenario ground-motion simulations through the system. Using various performance metrics to measure alert quality, we found that most of the population in the PNW could receive alerts with positive warning times for an alert threshold of MMI III, but that alert quality decreases as the MMI alert threshold increases because of missed and false alerts caused by inaccurate source estimates, time lags during processing, and underpredicted MMI alert threshold contour sizes. Using a less strict definition of warning time, we determine that about 10% of end-users that receive late alerts for MMI V would still receive alerts prior to the arrival of MMI VI or MMI VII level shaking. We also investigate the outcome of an alerting strategy where the entire PNW region receives an alert for MMI V level shaking when an *M* 8 is detected near the coast. We find that it eliminates all missed and late alerts except at sites close to the epicenter. The mean true positive rate is similar to using an alert threshold of MMI III, but the range of warning times is much greater for the *M* 8 alerting strategy and there is less risk of over-alerting in California.

The ShakeAlert system is continually evolving. Cascadia fault-specific templates for the FinDer algorithm and subduction zone specific contour distance tables for the eqInfo2GM algorithm are currently in development. Implementation of these features may improve the timeliness and accuracy of ShakeAlert performance for megathrust earthquakes on the CSZ. Further testing of system upgrades with simulated offshore earthquakes, over a range of magnitudes, would guide future improvements and inform alerting strategies.